AN IMPACT FORCE TRANSDUCER FOR ANTHROPOMORPHIC TEST DUMMY
HEADFORMS: APPLICATION TO STUDY EFFECTS OF EXTERNAL HELMET
ACCESSORIES ON BIOMECHANICAL MEASURES OF HEAD INJURY RISK

by

Robert Calyn Butz

A thesis submitted in partial fulfillment of the requirements for the degree of

Master of Science

DEPARTMENT OF MECHANICAL ENGINEERING
University of Alberta

Abstract

The first half of this thesis describes the mechanical design, calibration and validation of an in-fibre Bragg grating based impact transducer. The transducer comprises an in-fibre Bragg grating fixed to an aluminum superstructure (12 mm in diameter, 3 mm thickness) designed to withstand typical impact forces in helmeted impact and to have resonances that exceeds industry standards on mechanical resonance. Calibration experiments were used to determine the transducers sensitivity to force measurements, and calibration results are, on average, within 10% of finite-element modelling predictions of force sensitivity. Validation of force transducers indicated excellent repeatability in both the force and time domain for an impact. The maximum standard deviation of force measurements of 0.4% of the net head force applied to the impacted headform and average error in the time duration of the force transients of only 4%.

The latter components of the thesis describe application of the transducers and HybridIII in a biomechanical study of the effects that external helmet accessories (camera mounts) have on measures of skull fracture and brain injury risk in helmeted head impact. The presence of a helmet accessory reduced peak linear acceleration of the head, and forces on the headform skull did not increase. For low velocity impacts, peak angular acceleration and velocity reduced with the presence of a helmet accessory. For high velocity impacts, the peak angular acceleration and velocity of the head increased with the presence of a helmet accessory. Overall, the impacted helmets protected the head from significant skull fracture risk (regardless of the presence of the camera). Average concussion risk increased in high velocity impacts with cameras fixed to helmets.

Acknowledgements

Table of Contents

List of Tables

List of Figures

1   INTRODUCTION

1.1   Introduction

This thesis describes the development of an experimental model to study head-helmet force interactions during simulated impact to anthropomorphic headforms used in helmet certification and head injury research, including the HybridIII anthropomorphic headform, and subsequent application of the experimental model to study a timely hypothesis on head injury in sport. The first half of this thesis describes the mechanical design, calibration and validation of an in-fibre Bragg grating (FBG) based impact force transducer that integrates with the HybridIII headform and allows measurement of transient impact forces in parallel with the common acceleration measures obtained from the HybridIII. The latter components of the thesis describe application of the transducers and HybridIII in a biomechanical study of the effects that external helmet accessories (camera mounts) have on measures of skull fracture and brain injury risk in helmeted head impact.

1.2   Overview of head anatomy, mechanics and head injury

The human head houses three major structures: scalp, skull and brain. The scalp is the outer layer of the head and is approximately 5 mm to 7 mm thick and consists of skin, connective tissue and muscle [1]. Below the scalp is a loose connective tissue that covers the bony skull. The skull or cranium is a structure consisting of several bones fused together (Figure 1.1). The skull can be divided into frontal, occipital, parietal and temporal (Figure 1.1) regions [2]. The human skull supports the structures of the face and forms a cavity for

the brain. The four major bones in the skull act as the protective bones that protect the brain from its surroundings. Three membranes called the dura mater, the arachnoid mater, and the pia mater protect and separate the brain from the skull (Figure 1.2). Cerebrospinal fluid (CSF) fills the subarachnoid space and protects the brain from mechanical shock [3].

The brain is made of three main parts: the cerebrum, the cerebellum, and the brain stem (Figure 1.3). The cerebrum or cortex is the largest part of the brain and is divided into four sections (lobes): the frontal lobe, parietal lobe, occipital lobe and temporal lobe (Figure 1.3) [4]. Each section (lobe) of the brain is responsible for a different brain function. The frontal lobe is associated with reasoning, planning, and emotions. The parietal lobe is responsible for movement, perception of stimuli and spatial recognition. The occipital lobe is only responsible for visual processing. Lastly, the temporal lobe is associated with recognition of auditory stimuli, memory and speech [4].
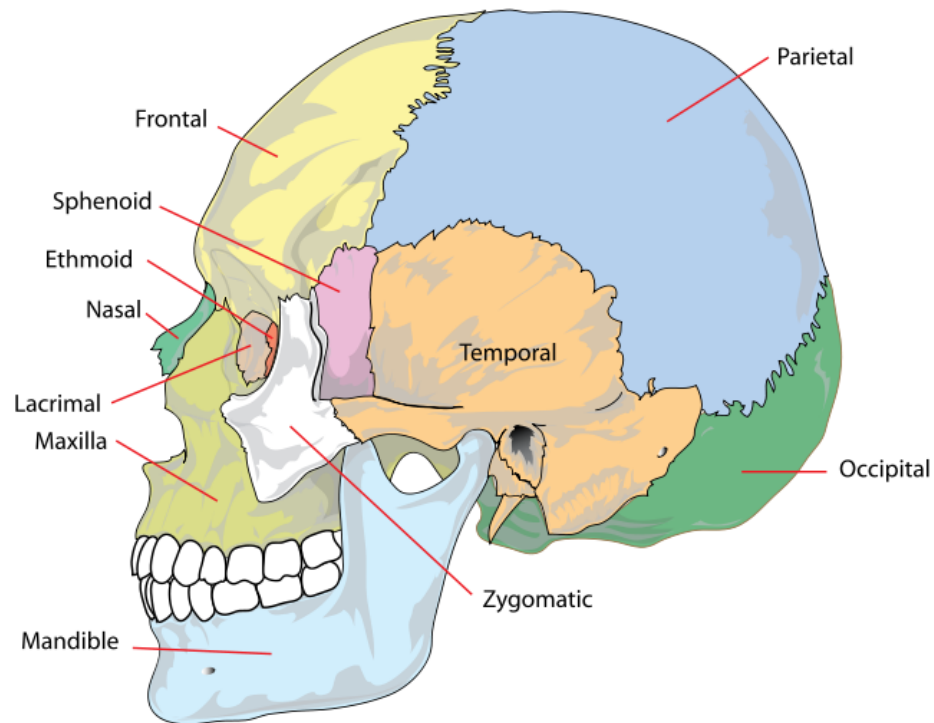
Figure 1.1: The skull can be divided into frontal, occipital, parietal and temporal regions [5].

An impact to the head results in mechanical energy transfer into all the anatomies described previously. These impacts can result in fracture of the skull, which can lead to damage to the soft tissues of the brain [1]. A major focus of injury biomechanics research is to establish human tolerances to these types of injuries, based on quantifying impact severity using mechanical measures related to head impact.
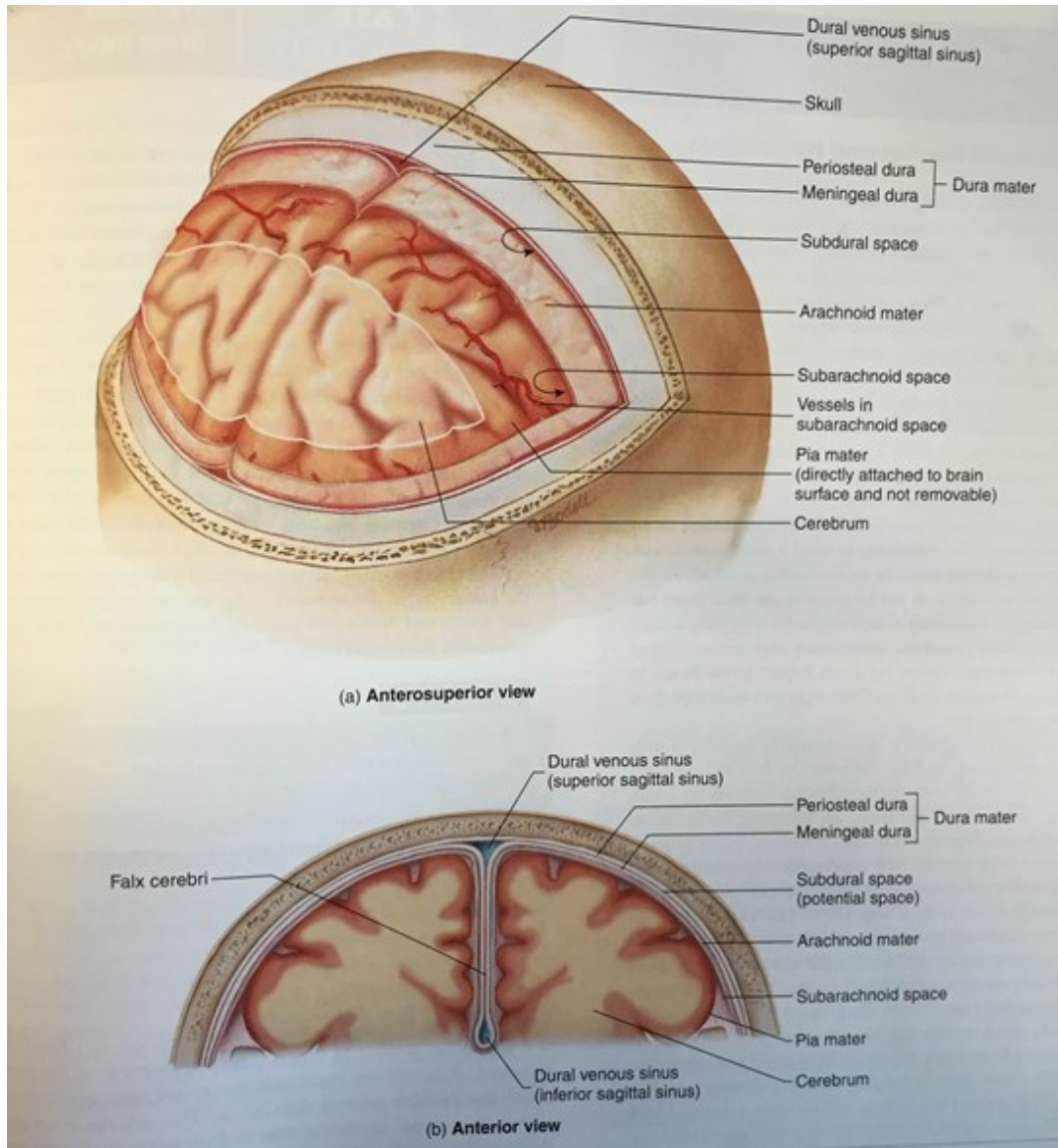
Figure 1.2: a) Meningeal membranes surrounding the brain. b) Frontal section of the head to show the meninges. Image taken with permission from Vanputte *et al.* [3]. Copyright 2014 McGraw-Hill (Permission to use this figure for non-commercial purposes given by Cynthia Aguilera; McGraw-Hill Education).
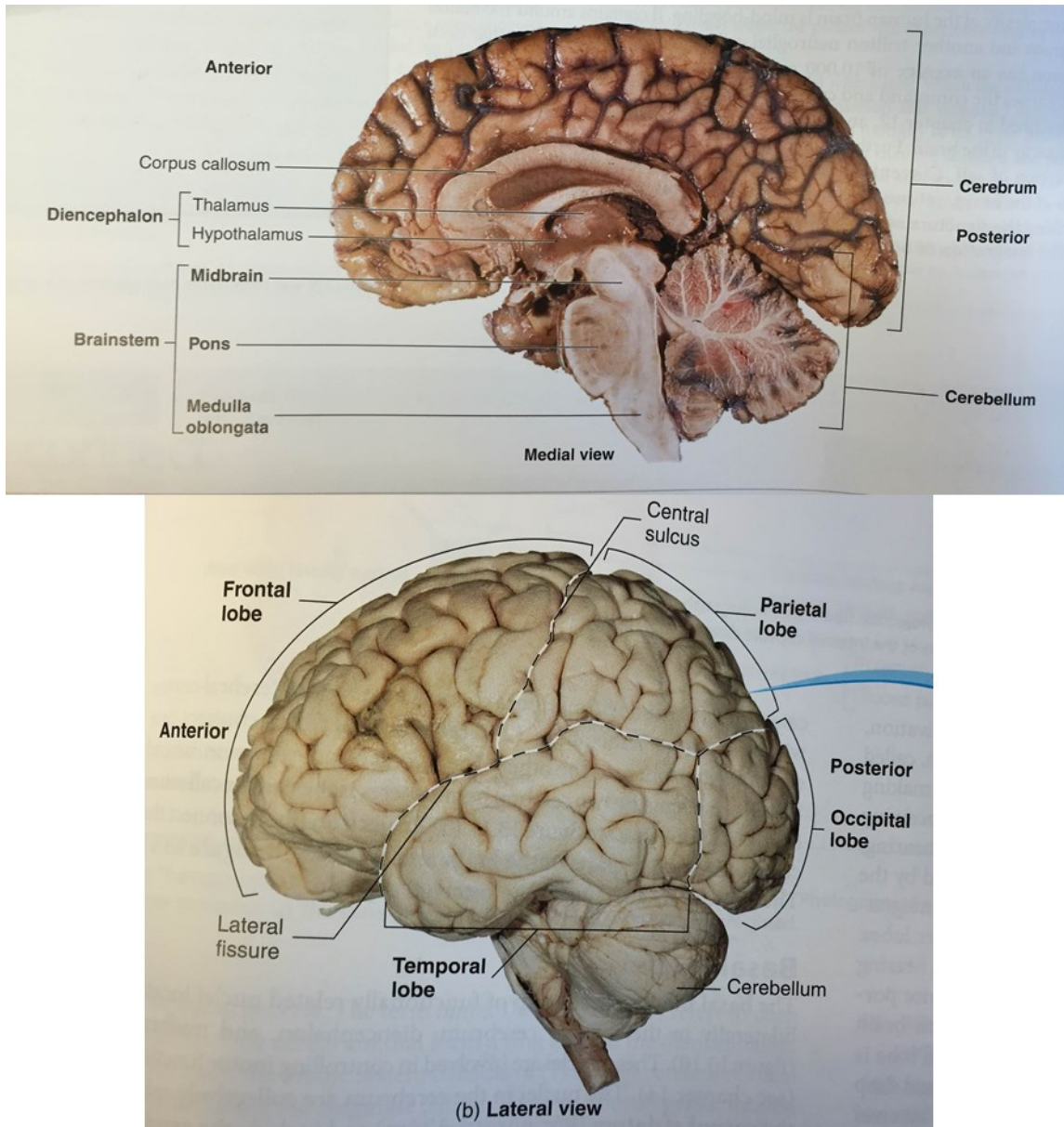
Figure 1.3: Top. Regions of the brain. Bottom. Cerebrum is broken down into 4 lobes: frontal, temporal, parietal, and occipital. Image taken with permission from Vanputte *et al.* [4]. Copyright 2014 McGraw-Hill (Permission to use this figure for non-commercial purposes given by Cynthia Aguilera; McGraw-Hill Education).

Head injuries sustained in accidents are a leading cause of fatalities and disabilities [6]. The injuries to the head that are most commonly associated with extended hospitalization and chronic symptoms are skull and brain injury. In the United States, the total combined rates

for skull and brain injury related emergency department visits, hospitalization and deaths have increased over the past decade. In 2010, the rates of hospitalization and deaths have climbed to 823.7 per 100,000 US population (521.0 per 100,000 in 2001) [6]. Head injury can occur as a result of force application (static or impact) to the head or through head kinematics (accelerations and velocities) that arise due to a fall or other scenario where head loading is absent. Skull fractures can occur when the head experiences a large mechanical load to the head from blunt force trauma. Under static loading the head deforms until it reaches a maximum deformation, then the skull fractures, exposing the brain to further injury [1]. In accidents (falls, sport related impacts), however, impact loading is more prevalent. Forces on the head are typically associated with fractures of the skull, but can also cause brain injury [2],[7]. Head injury can also be caused by kinematics, such as acceleration (linear and angular) [8] and velocity [9] of the head. In non-contact scenarios, the head experiences accelerations (both linear and angular), and the brain may experience injury despite the skull fracturing. These brain injuries are caused by tissue damage that is caused by the kinematics experienced by the head. Brain injury can occur anytime the brain is exposed to high-levels of strain or stress, or there is considerable damage to the anatomies that lie under the skull[10].

Injuries to the brain are generally classified as two types of injuries: diffuse and focal injuries [1]. Focal brain injuries are described as damage to the brain where the damage is confined to one area of the brain. In most cases, the brain tissue is damaged at the site where the injury occurred. The most common types of focal brain injuries are hematoma and contusions [1]. Brain contusions are most often caused by an impact to the head that results in a bruise of the brain tissue. Because contusions involve structural brain damage, they are

considered a serious brain injury. Hematoma is defined as the bleeding of the brain and is usually caused by trauma to the skull that damages the blood vessels underneath the skull, resulting in blood being leaked into the surrounding brain tissues [1]. Hematoma is generally classified as a fatal brain injury.

Diffuse brain injuries are far less severe than focal brain injuries, but can still cause considerable damage to the tissues of the brain. The most common type of diffuse brain injury is mild concussion (no loss of consciousness) or mild traumatic brain injury (mTBI). Mild traumatic brain injury is caused by trauma to the head that can result in damage to the brain tissue and result in loss of consciousness [6]. Symptoms of mild traumatic brain injury include: nausea, headache, fatigue and other cognitive issues [6]. Repeatedly sustained concussions may result in an increase of damage to the brain tissue and can lead to the development of more serious injuries, such as, mild cognitive impairments (MCIs), and chronic traumatic encephalopathy (CTE, which can be fatal). Sustaining repeated concussions has been shown to cause a change in the person's personality or mood as well as cause depression [6]. Although concussions reported in sports are often classified as minor or mild, they are, particularly in youth sports, a major concern.

The Centers for Disease Control and Prevention concludes that the number of mTBIs that occur annually in the United States is an estimated 1.6-3.8 million cases [6]. A 2007 epidemiological study conducted by the National Collegiate Athletic Association (NCAA) on American football revealed that concussion accounted for 6.8% of all game injuries and 5.5% of all practice injuries [11]. Athletes involved in contact sports such as hockey and football

are exposed to a relatively high risk of concussion (0.37 to 0.91/1000 injury rate per athlete exposed)[12].

Because rates of brain injury remain elevated in both sport and accidents despite widespread use of protective devices such as helmets, interest in understanding the mechanics of mild traumatic brain injury and the pathophysiology of the injury, as well as the short term and long term effects, has grown over the years. Biomechanical researchers have conducted countless experiments to understand the mechanics of brain injury as well as to come up with metrics to assess the severity and probability of head injury risk.

1.3   Assessment of head injury through kinematics

Much of the recent research in head injury stems from the automotive sector and sport. Automotive research is typically devoted to developing kinematic correlations to head injury severity and risk, and focuses on bare head impact (impact to the head where the head is not protected by a helmet or other protective device). Sport research into head injury typically focuses on helmeted head impact, and like automotive research, seeks to correlate measures of impact severity to risk of head/brain injury. Biomechanical (both sport and automotive) research suggests that parameters including linear and angular acceleration [8], velocity [9], and directional kinematics [7], [13] are needed to accurately assess injury risk and protective efficiency.

One of the earliest, and until recently perhaps the most common, methods to assess both head impact severity and (later on) helmet efficacy was based on measuring the peak linear headform acceleration (most commonly in multiples of the acceleration due to gravity,

9.81m/s/s = 1g) [1]. In the 1950s and 1960s, injury biomechanics of the head were investigated through cadaver head impact and the injuries of emphasis were skull fractures (which were also considered as an indicator of severe life threatening brain injury). In these cadaveric studies, mainly drop tests against a rigid flat anvil were performed.

Results from these cadaveric tests [14] (for example, as shown in Figure 1.4) suggested that for skull fracture, there was a relationship between the linear acceleration experienced by the head and the time duration of the acceleration that the head experienced. For example, as shown by the solid line fit to the experimental data in Figure 1.4 that is the 'demarcation' between safe (no fracture – below the line) an unsafe (skull fracture – above the line), a head acceleration of 100 g may be safely sustained in bare head impact for 5 msec. Barring the first British helmet standards [15], it is interesting to note that a majority of the helmet certification standards from the following decades and still in use today (e.g. hockey and cycling [16], [17]) in large part rely upon measures of peak head acceleration to decide whether a helmet provided adequate protection. The majority of helmet standards committees set minimum criteria on head protection to limit peak linear head acceleration to be less than 300 g (275 g in some cases). The genesis of the 300 g threshold is arguable; however helmets meeting these limits have been credited with eliminating fatal head injuries in many sports.
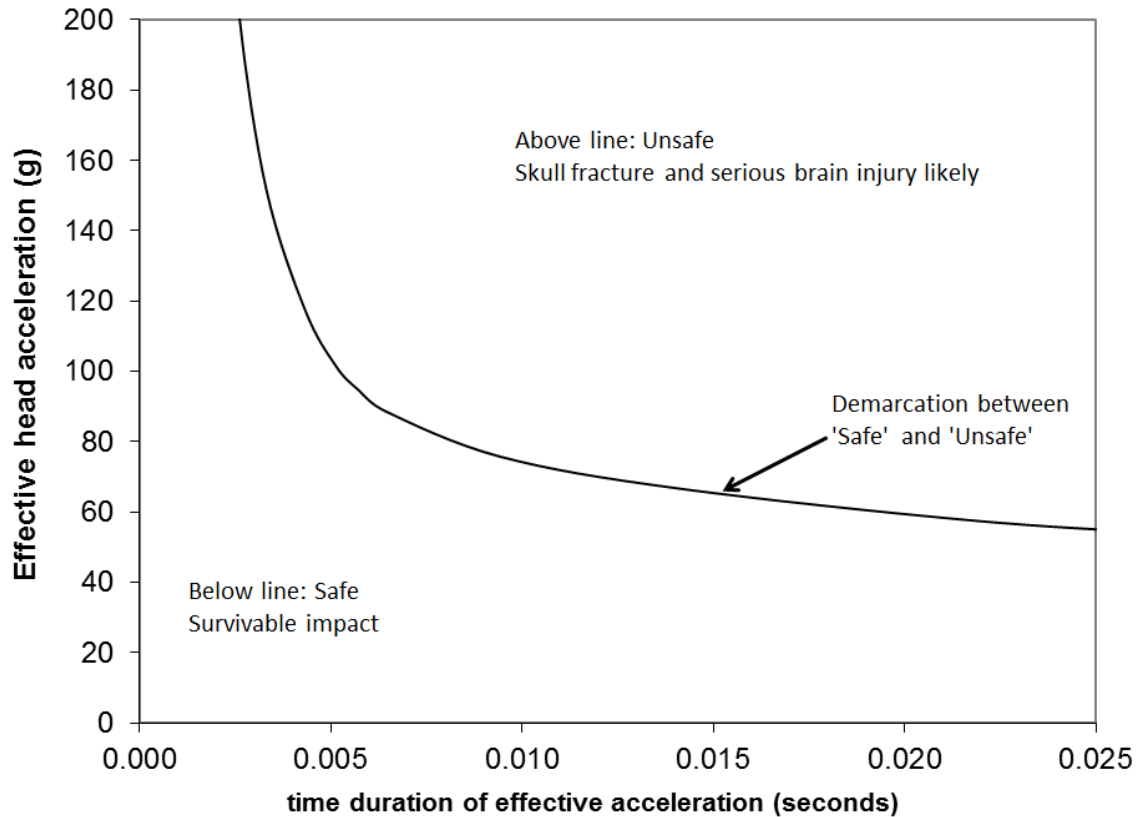
Figure 1.4: The Wayne State Tolerance Curve (WSTC) was first proposed by Gurdjian [14]. The WSTC provides a relationship between the average linear acceleration of the head and the time duration of that acceleration pulse. Figure constructed based on data presented by Hodgson and Thomas (1971) [18].

While not invoked in a large number of helmet standards, the apparent relationship between acceleration magnitude and duration (for a given injury type) has long been known and did lead to development of metrics to quantify impact severity (later adapted to quantify helmet performance). The Wayne State Tolerance Curve (Figure 1.4, above, termed the WSTC) was first proposed by Gurdjian [14] and was invoked in developing these metrics. The WSTC provides a relationship between the average linear acceleration of the head and the time duration of that acceleration pulse. As mentioned briefly above, combinations of acceleration and time durations that lie above the curve is thought to cause severe head

injury. Combinations below the curve do not exceed human tolerance, but may result in mild reversible head injuries. Skull fracture was used to demark the line on the WSTC (the boundary between severe life threatening injury and reversible), which causes complications in using the WSTC because injuries to the brain such as strain deformation can be present without the skull fracturing.

Researchers needed ways to assess injury risk by taking into account both acceleration and time duration of the acceleration pulse simultaneously. Gadd developed the Severity Index (SI) as a way to fit the information from the WSTC curve into an equation [19]. The SI was the first criterion used to assess injury risk and provide a numerical value based on the acceleration of the head and the time duration of the experienced acceleration. An SI of greater than 1000 was considered to be dangerous to life. In 1971, to address some complications with SI, Versace proposed a functional similar to SI. Versace suggested that the acceleration of the head can be expressed as a mathematical average. Versace also pointed out that the average acceleration could be computed at any time interval within the acceleration pulse. The functional proposed by Versace, considers both acceleration magnitude and acceleration duration [20], maximizes the integral of head acceleration against time, and is computed based on the following expression:

$$HIC = max \left[\frac{1}{t_2 - t_1} \int_{t_1}^{t_2} a(t)dt \right]^{2.5} (t_2 - t_1) \qquad (1.1)$$

Where t_2 and t_1 are two arbitrary time points during the acceleration pulse. Acceleration (a) is measured in multiples of the acceleration of gravity (g) and time is measured in seconds. The criterion for head injury became that the numerical value of the new expression

not exceed 1000. The Head Injury Criterion (HIC) was then proposed by the National Highway Traffic Safety Administration (NHTSA) as a replacement for the SI and is computed using the Equation 1.1. A variant of HIC, HIC over 15 milliseconds of the impact duration (HIC-15), has since been invoked in NHTSA Federal Motor Vehicle Safety Standard as a standard measure for head injury risk [21].

HIC is the current assessment function for the evaluation of closed head injury probability in automotive crash testing. Since HIC is computed solely with linear accelerations of the head, many complications arise when using HIC as a metric to predict injury risk. HIC is not specific to direction of impact and HIC neglects the role of angular accelerations of the head, factors that are now known relevant to injury risk [22]. Standards organizations suggest it is not recommended for helmet evaluation [23], and further, it is not now considered to be a useful measure of mild or diffuse brain injury probability [24], which therefore limits its utility in contemporary head injury research.

Other head impact assessment functions have incorporated additional metrics, such as angular acceleration and change in angular velocity, to assess injury risk. These injury criteria include the Brain Rotational Injury Criterion (BRiC [9]) and the Generalized Acceleration Model for Brain Injury Tolerance (GAMBIT [25]). BRiC is based on a combination of peak angular acceleration and angular velocity change. GAMBIT accounts for both linear and rotational acceleration. Both assessment functions have grown in popularity, but are not yet widely used in impact testing. In 2000, the Head Impact Power (HIP [13]) was introduced as:

$$HIP = ma_x \int a_x dt + ma_y \int a_y dt + ma_z \int a_z dt + I_x a_x \int a_x dt + I_y a_y \int a_y dt + I_z a_z \int a_z dt \qquad (1.2)$$

Each of the terms within the integrands equals velocity change. HIP considers acceleration, mass, and velocity change, as well as directional issues. HIP also accounts for contributions due to angular motion and inertial properties (mass) of the head. HIP has been shown to correlate better to mTBI probability than any other current criterion function [26].

A small but growing amount of biomechanical research on transient head impact forces has suggested that force distribution and transient aspects of force could be relevant to injury [7], [27],[28]. Impacts to the head can cause transient forces on the head to exceed the human tolerance and cause severe head injury such as skull fractures. Finite element analysis with skull-brain models has shown that transient focal impact forces on the skull lead to skull deformation and, in turn, an intracranial pressure distribution which initially forms at the impact site (coup site) and subsequently migrates through the brain as time progresses [7]. The inter-cranial pressure distribution causes shear deformation of the brain resulting in injury, and these deformations are force magnitude and force location dependent. Because strain in brain tissue is thought to correlate with injury [27], these transient focal forces and force locations could give useful measures in studying the mechanics of head injury.

The finite element analysis described above suggests that impact force location is a strong predictor of head injury risk. Therefore, measurement of impact location with corresponding temporal force distributions between the head and helmet could be a useful measure that augments the kinematic measures of impact severity, described above.

1.4   Engineered protective devices – helmets

Since the adoption of helmets, fatal brain injuries have virtually been eliminated in many sports (the most famous example being football [29]). Despite the widespread use of helmets in contact sports, epidemiology studies suggest mTBIs still remain high and are a major concern to athletes and the public as a whole [30].

The helmet is composed of three major components (see Figure 1.5): the outer shell, impact liner and retention system. The helmet shell is typically made of a hard plastic. The helmet shell is designed to resist penetration of any foreign object that would result in direct skull fracture. The helmet shell is also designed to distribute the impact load to the helmet liner. The helmet liner is typically crushable foam that is engineered to limit forces on the skull below magnitudes that cause skull fracture. As a consequence of limiting forces, head accelerations of the head are also attenuated [31]. Figure 1.6 shows the interaction of a bicycle helmet with a magnesium test headform during a frontal impact. The purpose of the retention system is to keep the helmet from moving while on the head, and can be used to tighten or loosen the fit of the helmet. The primary function of the helmet is to limit forces on the head below fracture tolerances, increase time-durations of these forces and limit peak head acceleration [32].

The evaluation of helmet protective efficiency is governed by international standards (ASTM[16], CSA[33], ISO[34], and NOCSAE[35]) that rely on minimizing the metric of peak acceleration during a free fall impact onto a hard surface. Each standard outlines the testing protocols for certifying a helmet. An anthropomorphic test headform is used as the surrogate head to test helmet protective efficiency. Protective efficacy based on these

standards is based on a linear drop test using a linear drop monorail to impact the helmet onto a flat steel anvil. The drop heights and impact velocity are specified in each standard. A helmet is considered certified if after complying with the standard test protocols, the helmet limits peak linear accelerations of the head to below 300 g. These international standards are based solely on limiting the metric of linear acceleration and do not account for rotational effects on the head. Indeed, none of the metrics described above that correlate with diffuse injuries (BrIC or HIP) have been invoked in helmets standards, arguably because they require measurement of angular kinematics and directional kinematics and, therefore, would require increases in the amount and complexity of instrumentation needed for helmet certification. Helmets certified against these standards have proven effective at eliminating skull fractures and fatal brain injuries in contact sports. However, there is no strong clinical evidence that these helmets reduce the incidence of mTBI [36]. Despite helmet use, concussion rates at both the amateur and professional levels of contact sports remain high [30] (0.37 to 0.91/1000 injury rate per athlete exposed [12].
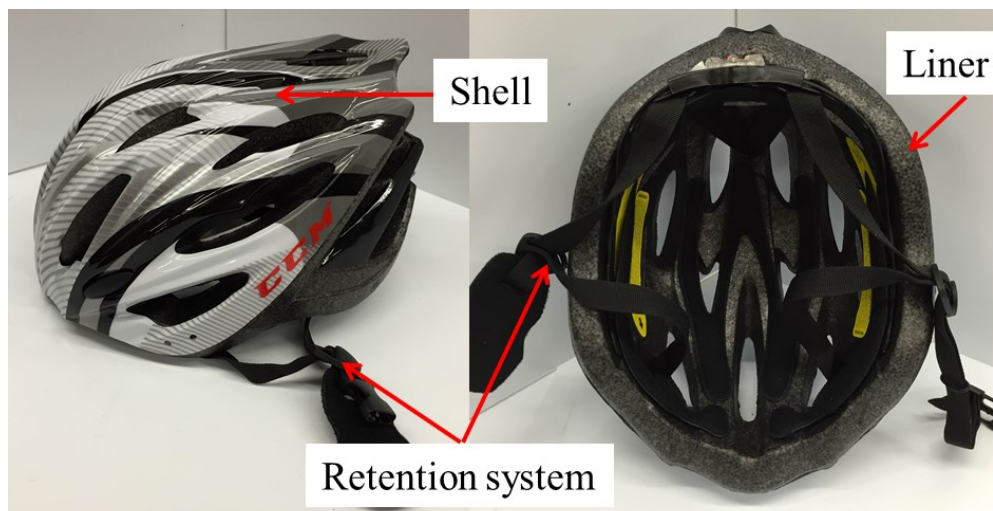
Figure 1.5: The helmet is composed of three major components: the outer shell, impact liner and retention system (chin strap).
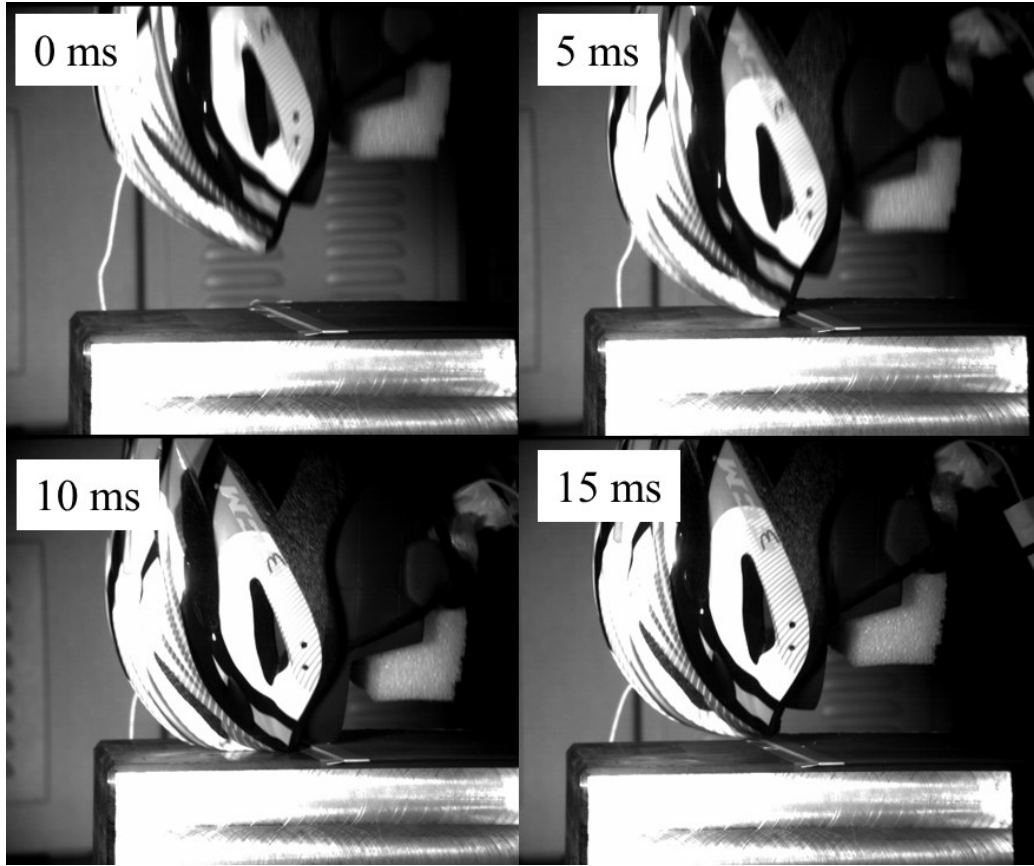
Figure 1.6: Frames of a high speed video capturing a frontal impact.

As mentioned above, FE analysis [7] has shown that impact force location is a strong predictor of concussion risk. Therefore, measurement of impact location with corresponding temporal force distributions between the head and helmet could augment our understanding of helmet performance.

There are currently no established transducers and techniques for measuring head-helmet interaction forces using helmet test headforms. In this thesis, a transducer technology has been developed that can integrate with the HybridIII headform and common magnesium headform used in helmet certification. The integration of these transducers with the HybridIII and magnesium headform allows us to measure both head-helmet interaction forces as well

as the common kinematic measures (described above) in our subsequent investigations on head injury and helmet performance.

1.5   Brief review of force/stress measurement techniques

The most common sensing system to measure forces during helmeted impacts is through the use of stress sensitive films. These films have sensing elements within the film, and these embedded elements allow for the measuring of stress distributions.

Precale Film (Fuji Photo Film Co., Japan) and I-Scan (Flexiforce® and other variants, Tekscan Inc., Boston, MA) are the most common tools to measure contact force [37], [38]. Both are force-sensitive films that can be integrated between contacting surfaces. Because force-sensitive films are inserted between contacting surfaces, they distort the natural contact mechanics. The resulting error (14-28%) depends primarily upon film thickness and modulus, surface curvature, and the compressive modulus of the contacting materials [37], [38]. I-Scan provides dynamic data, while Prescale provides only static (peak) data. Force measurements with Prescale have been performed between headforms and hockey helmets. Results show poor correlation between peak forces and injury risk [39], but, due to the limitations of Prescale, force durations and rates (temporal aspects of the impact) could not be determined. I-Scan has only been applied between helmet impact foam samples and metallic impactors for the purpose of studying impact liner performance [28], but is subject to the significant measurement errors noted above. Due to the limitations of films there is no established method to accurately quantify the contact mechanics between the skull and

helmet. In other words, there is no force transducer designed to integrate with helmet test headforms and measure transient forces relevant to helmet performance and head injury.

1.6   Thesis objectives

The first main objective of this thesis is to develop impact force transducers that can integrate with existing established anthropomorphic test device (ATD) headforms like the HybridIII, such that transient impact forces can be measured during impact. The second main objective is to apply the force transducers to answer a timely research question on head injury: do external helmet accessories (e.g. camera mounts, cameras), alter the biomechanical measures of injury risk, with emphasis on skull fracture and brain injury.

The effects helmet accessories have on head protection has been a concern to the standards organizations [17], but more recently they have been blamed for exacerbating injury in high profile athletes [40]. There is currently no biomechanical data on effects of helmet accessories, and no experimental model suitable for studying these effects. The contributions in this thesis address these considerations.

This thesis is organized into three sub-objectives that are structured to systematically progress toward fulfilling the main objectives described above.

- The first sub-objective is to design an in-fibre Bragg grating (FBG) based impact force transducer that can integrate with contoured surfaces of helmet test headforms.
- The second sub-objective is to calibrate and validate the transducers for transient impact force measurements on ATD headforms commonly used in helmet certification and head injury research.

- The third sub-objective is to apply the FBG-based impact transducers to contact force measurements of the head in helmeted impacts to distinguish if the presence of an external helmet mounted camera will increase the risk of head/brain injury.

1.7   Thesis organization

Background information needed to understand the force transducer design and main transducing element, FBGs, and previous research using FBGs is presented in Chapter 2. Chapter 2 concludes with a brief overview of the pragmatic considerations for using Bragg gratings in biomechanics. In Chapter 3, the design of the impact force transducers is presented. Detailed analysis on determining the transducers dimensions and properties is also outlined in Chapter 3. In Chapter 4, the calibration of the prototype impact transducers is given. Chapter 4 concludes with the results of the calibration trials and the transducer's sensitivity to force is presented. Chapter 5 describes the validation experiments used to assess the transducers repeatability in measuring impact force. The transducer was integrated with two test headforms and the results from these validation tests are presented at the end of Chapter 5. In Chapter 6, the impact transducers were integrated onto a test headform and an experiment to determine the effects of external helmet mounted cameras is outlined. Chapter 6 concludes with the results of this study. Chapter 7 concludes the thesis, summarizes the key contributions, and briefly outlines planned directions for future work.

A subset of the methods and results presented in Chapter 2 through Chapter 5 has been published in the Journal of Lightwave Technology:

- Butz, RC and Dennison, CR. (2015) In-Fiber Bragg Grating Impact Force Transducer for Studying Head–Helmet Mechanical Interaction in Head Impact. IEEE/OSA Journal of Lightwave Technology, 33(13), 8pp.

Methods and results of Chapter 6 are the subject of a second submission to the Journal of Biomechanics, which is currently undergoing review in consideration for publication:

- Butz, RC, Knowles, BK, Newman, JA, and Dennison CR. (2015) Effects of external helmet accessories on biomechanical measures of head injury risk: An ATD study using the HybridIII headform. Journal of Biomechanics, submission BM-D-15-00541, under review.

2   IN-FIBRE BRAGG GRATING THEORY

The purpose of this chapter is to introduce the reader to Bragg grating theory in preparation for understanding the optical impact force transducers presented in this thesis. The chapter also provides a concise overview of fibre optic transducer application in biomechanics research.

2.1   Introduction

From a telecommunications context, one of the most desirable features of optical fibre is ability to transmit light waves (communication signals) over large distances with very little loss [41]. Optical fibres are also intrinsically sensitive to their state and environment, and are therefore well suited as transducing elements for sensors. Optical fibres are comprised of two essential components: a core region, which serves to guide light along the fibre, and an outer cladding region (Figure 2.1a) [41]. The majority of transmitted light in an optical fibre is contained within the core region. The core region of the fibre has a relatively high refractive index compared to the clad, and the core-clad index mismatch creates the conditions for total internal reflection, and, as a consequence, the majority of transmitted light is confined to the core. Optical fibres are generally divided into two types: single mode and multimode. Single mode optical fibres have a very small core (5 to 10 μm in diameter, as shown in Figure 2.1a) and the light is transmitted as a plane wave perpendicular to the propagation direction [41]. This permits a wide transmission bandwidth by reducing sequential spreading of short light pulses. Multimode optical fibres have a much larger core diameter (as large as 100 μm) than single mode fibres and therefore can carry higher power. This type of optical fibre is

commonly used for industrial processing, whereas all interferometric-based sensors, including Bragg gratings, require single mode optical fibres [41].

2.2   In-fibre Bragg gratings

In-fibre Bragg gratings (FBGs) are a permanent periodic variation in the refractive index within the core of a single-mode optical fibre [41], [42] (see Figure 2.1a). The gratings consist of a series of regions of increased refractive index, n, spaced at a regular period, Λ, over the length of the fibre core (typically 1 mm to 10 mm). The periodic variation is formed by exposing the core to ultraviolet light that has a periodic pattern that is similar to the variation in the refractive index [43]. The formation of permanent gratings in an optical fibre was first demonstrated by Hill *et al.* [42]. They excited a Germania-doped optical fibre with argon-ion laser radiation at a wavelength of 488 nm and observed an increase in the intensity of reflected light until all light was reflected from the fibre [42].

The magnitude and period of variation of the refractive index determine the optical spectrum that is reflected by the FBG (see Figure 2.1b), this can be predicted from coupled-mode theory applied to optical waveguides. This reflection results from constructive interference between the forward light wave and the contra propagating light wave, and the reflected light is returned down the optical fibre [41]. This constructive interference only occurs at the Bragg grating within the core of the fibre.

When light propagates in the core of a conventional single-mode fibre [44] and encounters the Bragg grating, a spectrum of wavelengths is reflected. This spectrum is

centered at the Bragg wavelength, λ_B (Figure 2.1b), and can be calculated using the grating period, $\wedge$, and the reflective index, n_o, using the relation [41]:

$$\lambda_B = 2 \wedge n_0 \quad (2.1)$$

According to Equation (2.1), changes in the Bragg wavelength result from changes in the spatial-periods of the variation in the refractive index of the fibre and from changes in the fibre refractive index. For example, as detailed subsequently, strain on the fibre modifies the grating period, $\wedge$, and the refractive index, n, and causes a shift in the Bragg wavelength. The maximum reflectivity, R_{MAX} (Figure 2.1b), of the Bragg grating is used to predict the amount of light reflected for the entire Bragg grating, and can be calculated using the length of the grating, Lg, and the change in refractive index, Δn, for a given Bragg wavelength as [41]:

$$R_{MAX}(\lambda_B, Lg) = \tanh^2 \left[\pi \left(\frac{\Delta n}{2n_o} \right) \left(\frac{Lg}{\wedge} \right) \right] \quad (2.2)$$

Whereas the linewidth, $\Delta \lambda_W$ (Figure 2.1b), of the reflected spectrum is given by [41]:

$$\Delta \lambda_W = 2 \lambda_B \sqrt{ \left(\frac{\wedge}{Lg} \right)^2 + \left(\frac{\Delta n}{2n_o} \right)^2 } \quad (2.3)$$

The light that is not reflected at the given Bragg wavelength continues to propagate down the fibre and can illuminate subsequent FBGs set at different Bragg wavelengths. The reflective properties and the ability to be multiplexed enables FBGs to be used in a variety of applications that will be outlined subsequently.
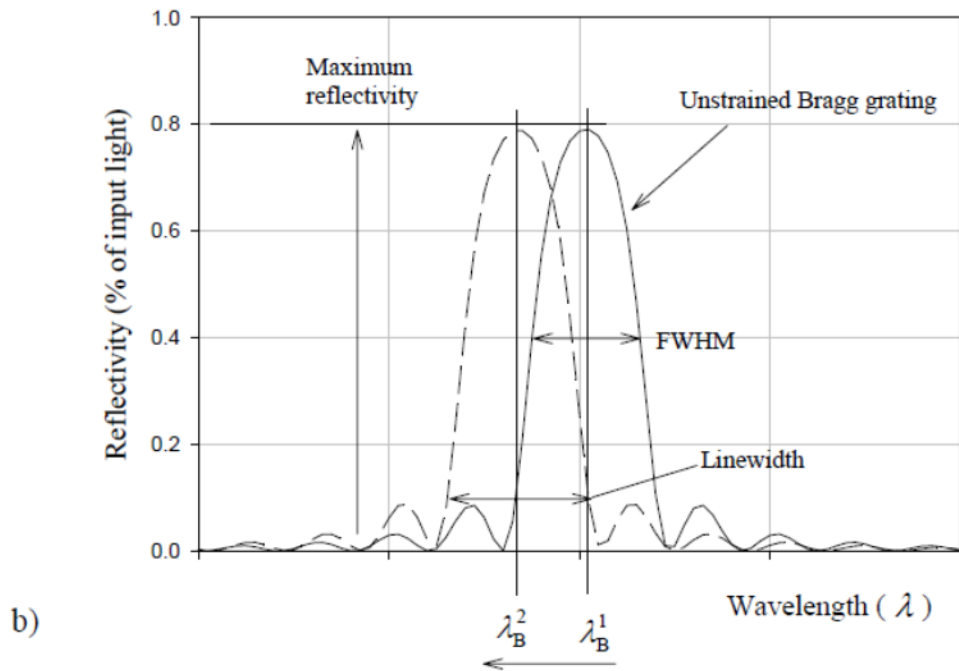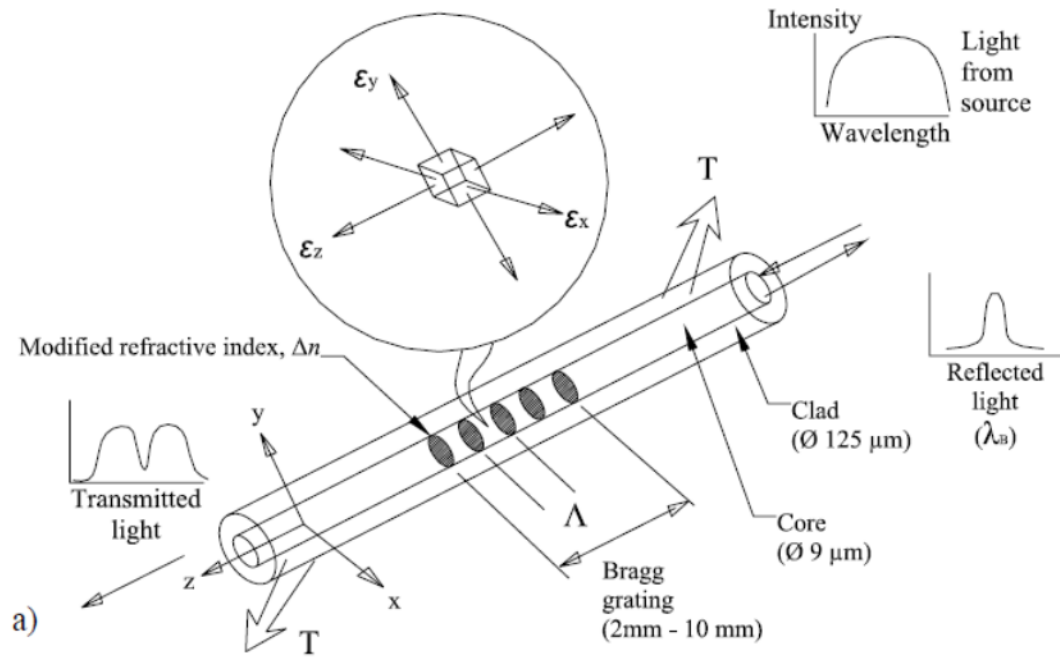
Figure 2.1: a) schematic showing features of in-fibre Bragg gratings including the core, clad and Bragg grating. The gratings consist of a series of regions of increased refractive index, n, spaced at a regular period, Λ, over the length of the fibre core; and b) optical spectrum that is reflected by the FBG. When strain is applied to the FBG, the Bragg wavelength, λ$_B$, will shift while the maximum reflectivity and full-width at half maximum (FWHM) remain constant. Reproduced with permission from Dennison (2008) Master's thesis [45].

The key attributes of FBGs that makes them an enabling transducer for biomechanical research are immunity to electro-magnetic interference, resistance to corrosive and humid environments, and, in some cases, the small size of FBGs (125 μm diameter and sensing gage lengths typically 1 mm to 10 mm). The small size of FBGs allows the fibres to be directly integrated into materials or be fixed on the surface of test objects like strain gauges.

Both mechanical strain and temperature perturbations at the grating will modulate (shift) the Bragg wavelength. The magnitude of Bragg wavelength shift is a function of the strain and temperature over the region of the grating. The shift in the Bragg wavelength from the principal strains (Figure 2.1a), ε_x, ε_y, ε_z, can be predicted as [41]:

$$\frac{\Delta\lambda_B}{\lambda_B}=\varepsilon_z-\frac{n_o^2}{2}\left[p_{zy}\varepsilon_z+p_{zz}\varepsilon_y+p_{zx}\varepsilon_x\right] + \zeta\Delta T \quad (2.4)$$

Where ε denotes mechanical strain with the subscripts referencing the fibre coordinate system shown in Figure 2.1a; and p_{zz}, p_{zx}, p_{zy}, are positive valued photo-elastic constants. Note that the subscripts on the photo-elastic constraints are referred to fibre coordinate system (Figure 2.1a). These photo-elastic constants relate strain magnitude to changes in the fibre-core index of refraction [41]. ζ is the thermo-optic coefficient of the fibre and ΔT is the change in temperature. For the studies performed in this thesis, thermal perturbations are neglected. The above equation can be used to predict the change in Bragg wavelength due to strains experienced by the fibre, including the axial strain sensitivity of an FBG. Transverse strains in Equation 2.4 can be transformed to purely axial strains by applying the Poisson's ratio of an FBG. To calculate the axial strain sensitivity of an FBG, Equation 2.4 can be rearranged as [41]:

$$\frac{\Delta\lambda_B}{\lambda_B} = G_\varepsilon \Delta\varepsilon \quad (2.5)$$

Where G_ε is the strain gauge factor of an FBG expressed as [41]:

$$G_\varepsilon = 1 - \frac{n_o^2}{2} P_\varepsilon \quad (2.6)$$

Where P_ε is given by [41]:

$$P_\varepsilon = p_{zy} - \nu \left(p_{zz} + p_{zy} \right) \quad (2.7)$$

Where ν is the Poisson's ratio of an FBG.

For a Germania-doped silica fibre, the photo-elastic coefficients have a value of 0.113 [41] for p_{zz}, and 0.252 [41] for both p_{zx} and p_{zy}, and the fibre core has an effective refractive index of 1.468 [41]. Using the photo-elastic coefficients and refractive index in the above equation the strain gauge factor, G_ε, can be calculated as 0.78. Using the strain gauge factor of 0.78 and an FBG with a Bragg wavelength set as 1550 nm, equation 2.8 can be used to calculate the strain sensitivity, S_ε, as 1.21 pm/micro-strain. The strain sensitivity can be used to predict the wavelength shift from strains in the fibre as [41]:

$$\Delta\lambda_B = S_\varepsilon \varepsilon \quad (2.8)$$

As detailed subsequently, FBGs are the transducing element used to develop the impact force transducers described in this thesis. In subsequent chapters, a detailed presentation of impact force transduction to strain and then wavelength shift are presented. Methods to use equations similar to Equation 2.8 to convert wavelength shift to impact force are also described.

2.3 Pragmatic considerations for Bragg grating application

Recently, with advances in swept-laser light sources, high-bandwidth photo-detectors, and oscillating interferometric cavities, FBGs can be interrogated from DC to kHz and are therefore suited for both static and dynamic measurements. Static and dynamic measurements of FBG sensors can be achieved using compact and robust interrogator instruments. To measure wavelength shift from FBGs, sweeping interrogators are used that operate at multi kHz frequencies. In this thesis we use a commercially available interrogator (details in subsequent chapters) that has a maximum scan frequency of 25 kHz.

The key characteristics of FBGs are: their small in size, biocompatibility, and ability to be multiplexed. Optical fibres are nominally 125 μm in diameter and various methods exist to reduce the fibre diameter to as small as 20 μm [46]–[48]. The extremely small size of FBGs allows the fibres to be easily embedded in material, unlike many other transducer technologies, and in the case of biomechanics research do not require removal of biomechanically relevant anatomy for their insertion. Optical fibres are constructed using silica glass that is chemically inert. Optical signals are retained with fibres and do not interact with tissues that surround the fibre. Unlike electronic and metallic transducers, FBGs are also compatible with medical imaging techniques such as computer-aided tomography and magnetic resonance imaging. To make distributed strain measurements, many gratings, each having their own distinct Bragg wavelength, are inscribed at locations spaced along the length of a single optical fibre. Transducers based on in-fibre Bragg gratings [49] have been developed to measure a variety of parameters including but not limited to strain [50][51], temperature [52], pressure [53], force [54], [55], and refractive index [56].

2.4   Previous biomechanics research involving in-fibre Bragg gratings

The first application of optical fibre technology dates back to the 1960s [57], when fibre bundles were successfully pioneered in endoscopy, both for illumination and for imaging. FBG-based sensors have grown in popularity in biomechanical research because of the FBG small size, biocompatibility and the ability to be multiplexed for distributed measurements. Researchers have used the desirable characteristics of FBGs to develop transducers for a wide range of applications in science and engineering including biomechanics [54], [58]–[60].

Carvalho *et al.* (2006) exploited the small size of FBGs to measure strain at the mandible surface of a dental implant [60]. The small size of FBGs enabled Carvalho *et al.* (2006) to integrate the FBG sensor into the mandible surface of two standardized dental implants. The work presented by Carvalho *et al.* introduced the use of FBG sensors as an alternative method over other sensors (strain gauges) for measuring strains. The FBG sensor proved to be a good biomechanical sensor because of the FBGs ability to measure dynamic strains. Using FBGs was beneficial to Carvalho *et al.* because FBGs proved to be more precise and less intrusive.

Mohanty *et al.* (2007) explored the use of an FBG sensor to measure distributed stresses during total knee replacement surgery [59]. The FBGs were altered to produce five sub-gratings and the multiplexed FBG was embedded in a fibre-reinforced composite. The FBG sensor was used to determine the pressure distribution across the tibiofemoral interface resulting from flexion/extension of the knee. The exploitation of the ability of an FBG to be serial-multiplexed was beneficial because it allowed the measurement the distribution of

contact stresses across the tibiofemoral interface. The multiplexed FBG array addressed the limitations of previously applied stress sensitive film technology because of the FBGs small size (easily integrated with tibiofemoral interface), it successfully measured the pressure distribution across the interface.

Dennison *et al.* (2008) [58] exploited the small size of FBGs to measure intervertebral disc pressure. The FBG sensor produced consistent measurements with previous studies using different sensors. The FBG sensor provided a less intrusive way to measure a linear response of disc pressure to applied compressive load [58]. The small size of FBGs provided an advantageous tool by allowing the authors to integrate the FBG sensors directly into the intervertebral disc and produce repeatable measurements.

Dennison *et al.* (2010) [54] also presented an FBG based sensor for contact force/stress measurements in intact cadaveric human hips. The contact force/stress sensor addressed limitations of stress-sensitive films (widely applied in joint mechanics research) that require removal of biomechanically relevant anatomy, and exhibited repeatable measurements in intact hips [54]. The small size of the FBG sensor allowed Dennison *et al.* to produce repeatable measurements in intact cadaveric human hips.

2.5   Summary

An FBG comprises regions of modified refractive index in a short length (i.e. 1-10 mm, Figure 1.1a) of the core of an optical fibre. FBGs reflect light at a prescribed wavelength (λ_B) which is a function of the refractive index of the fibre core and of grating spacing, both of which are functions of strain. As a result, the Bragg wavelength can be used as a measure of

strain. Transducers based on FBGs have been developed to measure strain [50][51], temperature [52], pressure [53], force [54], [55], and refractive index [56].

FBGs possess key characteristics that enable these fibres to be used in biomechanical research:

1. Small size: optical fibres can be easily integrated with head-helmet interface because of their small size (typically 125 μm in diameter).

2. Biocompatibility: optical fibres will not interact with the soft tissues of the body because they are made using chemically inert silica glass.

3. Multiplexing: To make distributed measurements, many gratings, each having their own distinct Bragg wavelength, are inscribed at locations spaced along the length of the fibre.

4. Can be interrogated at high rates: FBGS can be interrogated at rates from DC to many kHz to produce dynamic measurements. The FBGs used in this thesis will be interrogated at 10 kHz.

As a result of the key characteristics and the FBGs sensitivity to strain, FBGs have been exploited and used in a wide variety of biomechanics research. In the context of this thesis, we will exploit the small size and frequency response to develop an FBG-based impact force transducer that can be integrate with contoured surfaces of helmet test headforms. The design and properties of the novel impact force transducer will be outlined in Chapter 3.

3   DESIGN OF IMPACT FORCE TRANSDUCER

The design and modeling of the FBG-based impact force transducer is described in this chapter. The impact force transducers will be used to measure transient forces resulting from head impact. Forces applied to the transducer will produce axial strains along the integrated FBG and those force-dependent strains are transduced to optical wavelength shift using FBGs. These strains are directly proportional to impact force, and calibration of the transducer will provide a relationship between applied forces and induced wavelength shift. The key design criteria of our transducer were: small in size, ability to withstand impact forces up to 5 kN, and have a high acquisition rate. An overview of the basic design is presented first, followed by a complete description of the dimensions and materials of the transducer. The mechanics of impact force transduction to optical wavelength shift (as reported by the FBG) is given and a finite element model of the design is presented to predict transducer performance.

3.1   Conceptual design and basic solid mechanics

As mentioned in Chapter 2, a shift in the Bragg wavelength is caused by load induced strains along the Bragg grating. In the presented force transducer, impact forces applied to a mechanical beam result in strain transfer to the Bragg grating, and therefore Bragg wavelength shifts that are directly proportional to impact force.

The impact force transducer comprises an FBG that is integrated onto an aluminum superstructure (6061 T6 aluminum) (Figure 3.1). The basic design of the transducer is a cylindrical disc with a major diameter of 12 mm and an overall thickness of 3 mm (Figure

3.1). The geometry and dimensions of the transducer is small and compact in order to be easily integrated and not disrupt the overall geometry of anthropometric test headforms. The bottom of the sensor is hollowed to a depth of 1 mm to allow integration of the FBG and allow deflection of the transducer. The FBG integrated onto the underside of the superstructure will deflect with the transducer, and that deflection will create strains along the axis of the FBG, and those strains are directly proportional to transducer deflection, which is in turn directly proportional to impact force. Two 1 mm wide troughs are cut into the top face of the transducer (Figure 3.1) to produce a fixed-fixed beam centrally located in the transducer. As detailed below, the fixed-fixed beam dimensions were determined to ensure deflections of the transducer will not result in beam mechanical failure over the range of impact forces (0 kN to 5 kN) thought to occur in helmeted impact where skull fracture [2] is rare. The presented transducer is purpose-built for normal force (shown in Figure 3.1) sensing by deflecting in the normal direction (z axis). The superstructure is also designed to have mechanical resonance that is compatible with industry requirements for helmet test headforms (no resonances can exist below 2 kHz [61]). The mechanical resonance of the superstructure will be discussed subsequently.
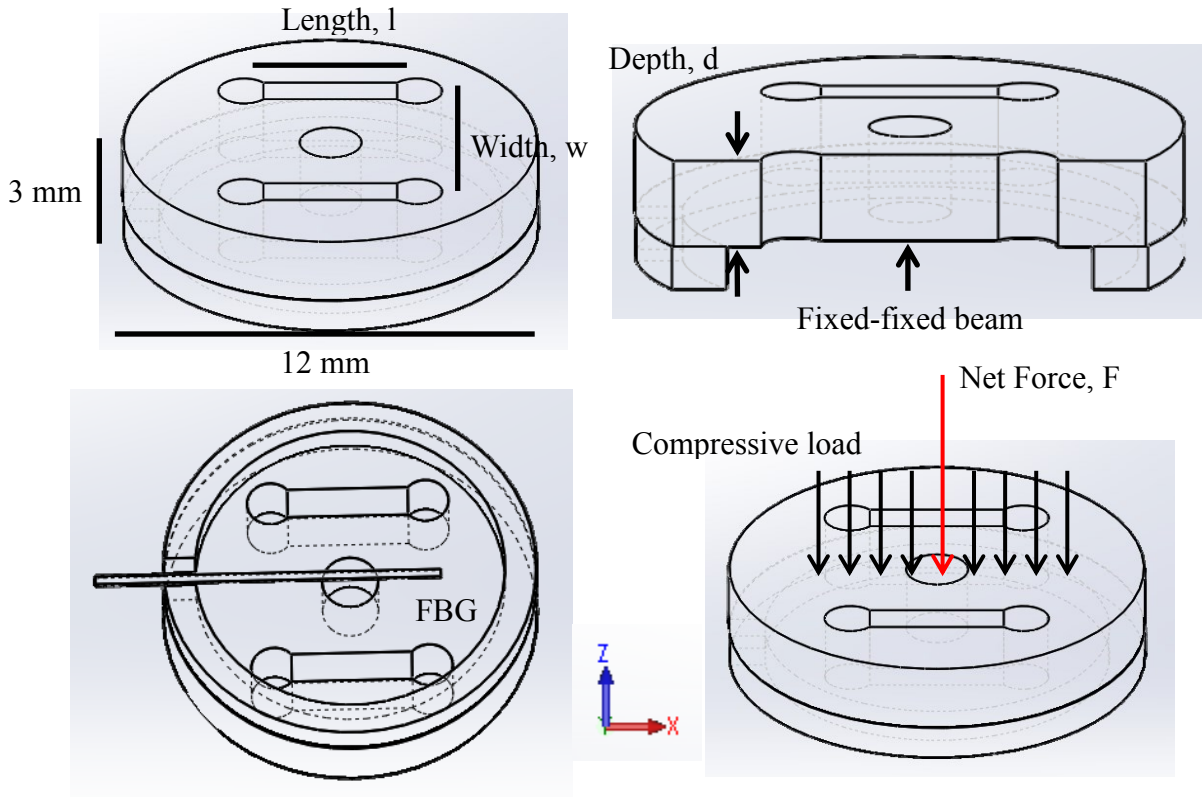
Figure 3.1: Schematic and section-view of impact force transducer. The transducer has major diameter of 12 mm and overall thickness of 3 mm. The transducer has a centrally located fixed-fixed end beam. FBG is permanently fixed to the underside of the beam and acts as the sensing mechanism.

To determine beam dimensions (primarily length in Figure 3.1) and overall sensor geometry, a deflection analysis was performed using basic solid mechanics of fixed-fixed beams. The deflection analysis was used to establish beam thickness and dimensions to ensure deflections of the fixed-fixed beam were lower than the maximum allowable deflection (1 mm). This maximum allowable deflection of 1 mm ensures the beam will deflect without the risk of bottoming onto the ATD headform to which the transducers will be fixed. Furthermore, once beam deflections were established, surface strains of the beam (at the location where the FBG is located) were calculated to ensure that the beam strains

coupled into the FBG were at or below that maximum strain that an optical fibre can reliably sustain (i.e. approximately 9,000 με [41]).

Three prototype beam dimensions were analyzed. The length of the beam (Figure 3.1) used in the analysis is 5 mm, 6 mm, and 7 mm, and the width of the beam (Figure 3.1) was set at 5 mm, 6 mm and 7 mm. The deflection of the beam was calculated using the relation of stress and deflection of a fixed-fixed beam given by the equation [62]:

$$y = \frac{Fl^3}{192EI} \quad (3.1)$$

Where F is the load located at the center of the beam, l is the length of the beam, E is the Young's modulus of aluminum (68.9 GPa [62]), and I is the area moment of inertia of the beam given by the relation:

$$I = \frac{wd^3}{12} \quad (3.2)$$

Where w is the width of the beam and d is the depth of the beam (2 mm).

The results from this analysis are given in Table 3.1. To solve for the maximum deflection, a force of 5000 N was used. Based on the results presented in the table, all combinations of beam dimensions produce a maximum deflection that is lower than the critical deflection of 1 mm. Based on this analysis the impact force transducer will not over-deflect and the fixed-fixed beam will not bottom out.

Table 3.1: Results from deflection analysis. Design feature sizes and calculated maximum deflection.

Length (mm)	Width (mm)	Moment of Inertia (mm^4)	Max. Deflection (mm)
5	5	3.33E-12	0.00142
	6	4.00E-12	0.00118
	7	4.67E-12	0.00102
6	5	3.33E-12	0.00245
	6	4.00E-12	0.00204
	7	4.67E-12	0.00175
7	5	3.33E-12	0.00389
	6	4.00E-12	0.00324
	7	4.67E-12	0.00278

To ascertain final beam dimensions and strains in the fixed-fixed beam, a stress/strain analysis was performed using basic solid mechanics. A stress/strain analysis was used to approximate the strain along the fixed-fixed end beam resulting from an expected impact force in helmeted head impact of 1200 N [63]. The results from this analysis will determine whether or not the total strains produced in the fixed-fixed beam will exceed the maximum allowable strain capacity of an FBG (9,000 micro-strain) [40]. The stress in a solid body can be calculated by dividing the force acting on the solid body by the area that force acts on. Hooke's law states that the stress acting on a solid body is proportional to the elasticity of the material (Young's modulus) and the strain of the deformation [62]. The strain in a solid body is the ratio of the elongation of a solid body's dimension relative to the original position. Hooke's law is given by the expression [62]:

$$\sigma = \varepsilon E \quad (3.3)$$

Where σ is the stress, E is the materials Young's modulus, and ε is the strain in the solid body.

For a given impact, the normal force acting on the force transducer will cause strains throughout the fixed-fixed beam. The strain along the bottom of the beam where an FBG will be located can be approximated by calculating the stress along the bottom of the beam and using Hooke's law to approximate the strain. The stress at the bottom of the beam can be calculated using the equations derived from a fixed-fixed beam's shear and moment diagrams. For a fixed-fixed beam the shear at the fixed ends can be calculated as one half the acting force on the beam.

$$V = \frac{F}{2} \quad (3.4)$$

Where V is the shear force and F is the impact force. From the moment diagram of a fixed-fixed beam, the moment at the fixed ends can be calculated as:

$$M = \frac{Fl}{8} \quad (3.5)$$

Where F is the impact force and l is the length of the beam. The stress in a fixed-fixed beam can be determined by the equation:

$$\sigma = \frac{Mz}{I} \quad (3.6)$$

Where z is the distance from the neutral axis to the bottom of the beam. Combining all equations together and introducing the stress and strain relationship (Hooke's law), the strain at the bottom of the fixed-fixed beam can be calculated using the relation:

$$\varepsilon = \frac{Flz}{8EI} \quad (3.7)$$

Where F is the impact force onto the force transducer, l is the beam length, z is the distance from the neutral axis to the bottom of the beam, E is the Young's modulus of the transducer (68.9 GPa), and I is the moment of inertia of the beam.

The results from the stress and strain analysis are shown in Table 3.2. The results of the stress and strain analysis show each combination of beam dimensions produces strain that is lower than the maximum allowable strain of an FBG (9,000 micro-strain) [41].

Table 3.2: Results from stress/strain analysis. Design feature sizes and calculated strain for the fixed-fixed end beam.

Length (mm)	Width (mm)	Moment of Inertia (mm^4)	Strain (micro-strain)
5	5	3.33E-12	3,269
	6	4.00E-12	2,721
	7	4.67E-12	2,331
6	5	3.33E-12	3,922
	6	4.00E-12	3,266
	7	4.67E-12	2,797
7	5	3.33E-12	4,576
	6	4.00E-12	3,810
	7	4.67E-12	3,263

Based on the deflection and stress/strain analysis of the possible combinations of beam dimensions, the results indicate low deflections (less than 1mm) and strains on the FBG that are appropriate relative to the maximum strain for an FBG (9,000 $\mu\varepsilon$). With this information, the chosen dimensions of the beam are a length and width of 5 mm. These were chosen to

both limit strain and deflection, but also to result in a transducer with small active sensing region.

3.2   Force transduction with Bragg gratings and sensor superstructure

Impact forces applied to the transducer create strains in the superstructure and these force-dependent strains are transduced to optical wavelength readings using FBGs. Force-dependent strains in the aluminum superstructure are coupled into the FBG such that FBG strains are along the axis of the fibre. Strains along the fibre will modulate the Bragg wavelength and the shifts in Bragg wavelength can be detected using standard equipment used in Bragg grating sensing. Changes in the Bragg wavelength, denoted by $\Delta\lambda_B$, proportional to the force-dependent axial strain, ε, can be calculated as [41]:

$$\Delta\lambda_B = S_\varepsilon \varepsilon \quad (3.8)$$

Where S_ε is the FBG sensitivity to axial strain (i.e. 1.2 pm/$\mu\varepsilon$).

The centrally-located fixed-fixed mechanical beam (Figure 3.1) deforms when impact forces are transmitted onto the transducer. In the present transducer configuration, a single FBG is permanently fixed to the underside of the beam using an epoxy (Epoxy 907, Miller Stephenson Chemical Company Inc., Danbury CT). This surface-mounted FBG experiences strain when the fixed-fixed beam deforms. These strains are directly proportional to beam deflection, which is in turn directly proportional to impact force.

A finite-element model of the transducer was used to predict the force sensitivity of the transducer and predict mechanical resonance. Static loading up to 1200 N was used to

determine the response to impact under the typical range of expected impact forces [2] and calculate a predicted sensitivity to force of the impact transducer. Also, the finite-element model was used to predict the mechanical resonance of the transducer to make sure the lowest resonance exceeded the requirements on mechanical resonance of helmet and crash-test headforms (>2 kHz [61]). The procedure in developing the finite-element model is outlined in detail in the subsequent sections.

3.3   Finite element modeling – structural

The finite-element method, implemented using ABAQUS Explicit (version 6.12, Dassault Systems Simulia Corp., Providence, RI), was used to analyze the transducer for both force sensitivity and mechanical resonances (modal analysis). The finite-element model was used to predict strain in the transducer superstructure and FBG when using typical helmet impact loads. The strains calculated in the FBG were used to develop a predicted sensitivity to force without fabricating the transducer. The predicted sensitivity to force obtained from the finite-element model and was used as the baseline sensitivity for comparison with fabricated prototype transducers.

A structural model comprising three parts was created to match the physical dimensions of the transducer (Figure 3.1). The three parts (as shown in Figure 3.2) are: transducer superstructure, FBG, and rubber liner. The rubber liner (Figure 3.2a) is used in the calibration procedure (detailed subsequently) to increase the time duration of impact and reduce the magnitude of applied force to typical impact contact forces (1200 N) [63]. The rubber was modeled as a solid circular disc with a diameter of 12 mm and a thickness of 1 mm. The

transducer superstructure (Figure 3.2b) was modeled as a solid circular disc with a major diameter of 12 mm and an overall thickness of 3 mm. A 10 mm in diameter cut was extruded out of the bottom of the transducer to a thickness of 1 mm to model the bottom of the transducer (Figure 3.2b) and allow the FBG to be fixed to the bottom of the fixed-fixed end beam. Two 1 mm wide troughs were cut into the top face of the transducers to create the fixed-fixed beam located in the center of the transducer (Figure 3.2b). A threaded #4-40 screw hole was cut into the center of the beam. The purpose of the hole was to provide an alignment and fixation point for sensor manufacture. Lastly, the FBG (Figure 3.2c) was modelled as a 1 mm rectangular prism. The width and thickness of the FBG was set to 125 microns to model the diameter of an FBG in a standard optical fibre [41]. A rectangular geometry was able to integrate with the bottom of the beam of the transducer more easily than a cylindrical shape.
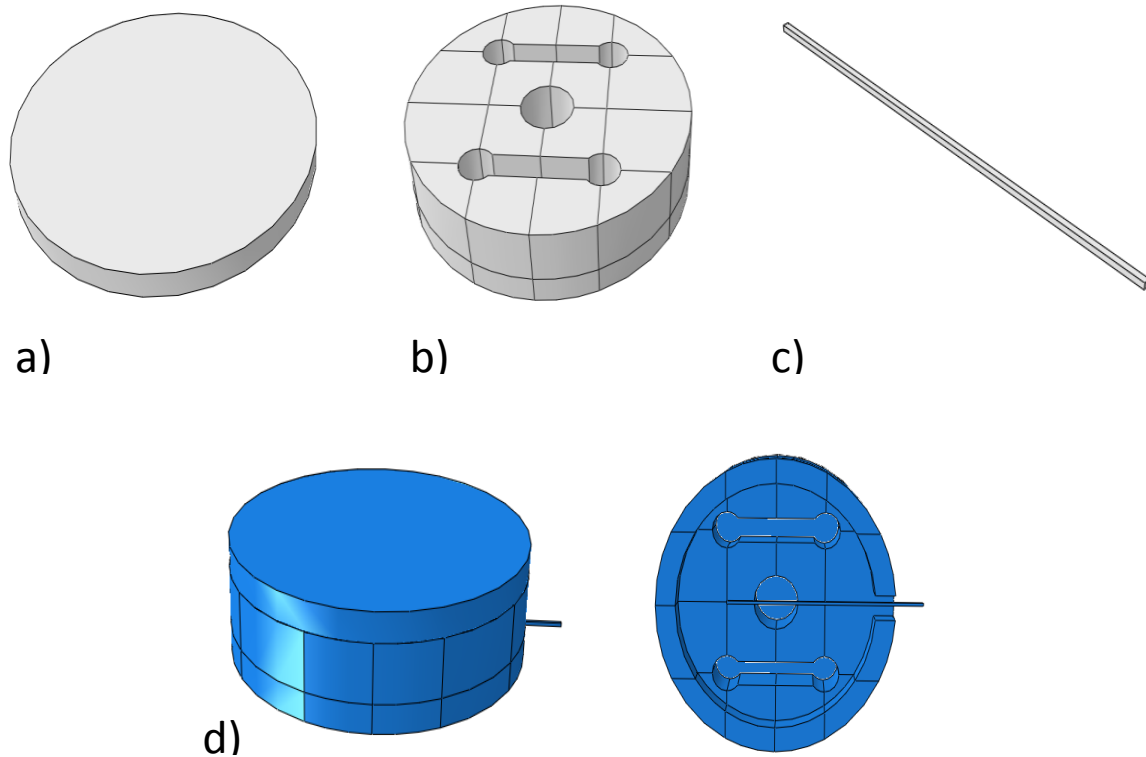
Figure 3.2: ABAQUS Explicit model of impact transducer. a) Rubber liner; b) aluminum superstructure; c) FBG fibre; d) Assembly and underside view of the impact transducer.

The material properties were assigned to each part to match the properties of the prototype force transducer (Figure 3.2d). The Young's modulus of the rubber liner was set as 2.64 GPa [62] with Poisson's ratio of 0.4 [62]. The Young's modulus of the 6061 T6 aluminum superstructure was 68.9 GPa [62] with Poisson's ratio of 0.34 [62]. Lastly, the Young's modulus of the FBG fibre was 69 GPa [41] with Poisson's ratio of 0.17 [41].

To predict transducer sensitivity to force, a static analysis was performed on the model. Thirteen load steps were implemented. The first load step was a compressive 100 N load, and the following 11 steps were incrementally (100N) greater, up to a maximum of 1200N. The final (13th) load step was a total applied load of 5000 N. This load was used to determine

whether the superstructure could withstand stresses associated with forces approximately double what was expected in application. The compressive forces were applied as pressure loads (acting in the normal direction) over the face of the button (see Figure 3.3). For each step, the pressure magnitude was determined to produce a resultant compressive load with a magnitude to match the load increments.
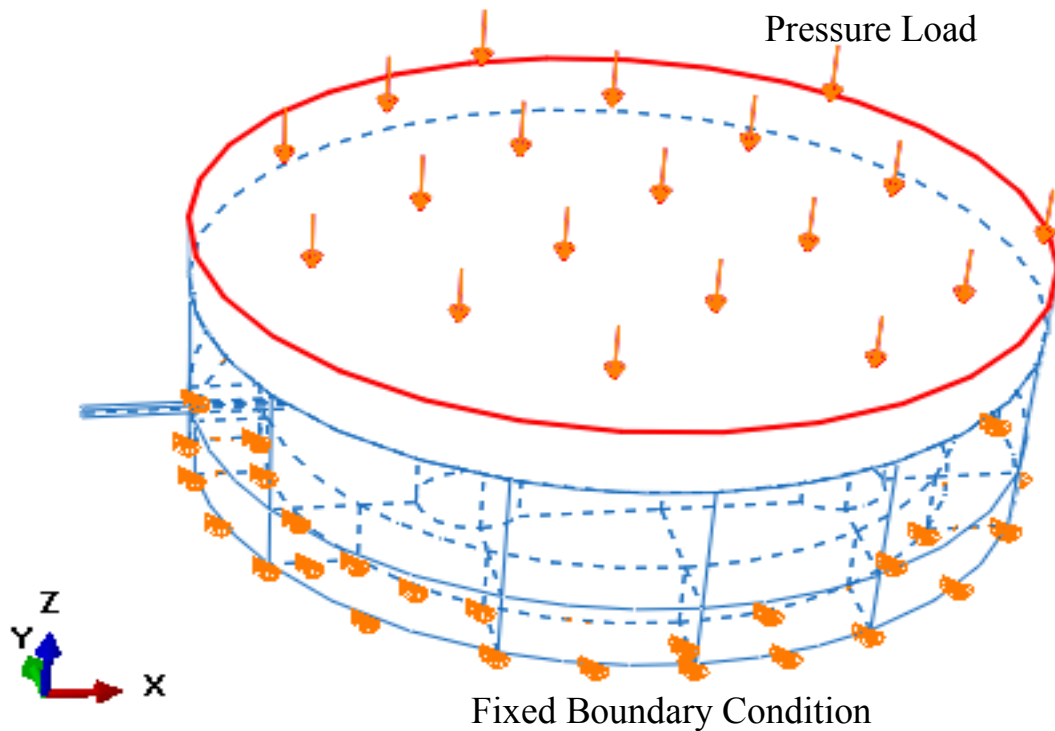
Figure 3.3: Wireframe schematic of impact transducer modelled using ABAQUS Explicit. A compressive pressure load is applied to the face of the button to produce a resultant compressive load acting through the center of the transducer. The magnitude of the pressure load modelled a static analysis with a load range of 100 N – 1200 N with 100 N incremental steps. A fixed boundary condition is applied to the bottom of the transducer to fix the transducer in space to eliminate movement and rotation in the x, y, and z planes.

A fixed boundary condition was applied to the bottom of the transducer (Figure 3.3) to fix the transducer in space. The boundary condition eliminates the motion of the transducer

in the x, y, and z axes, as well as eliminates rotation in the three planes. All other components of the transducer were able to move freely in all directions.

The contact between the FBG and aluminum superstructure was modeled as a tie constraint (see Figure 3.4). A tie constraint eliminates the degrees of freedom on adjacent nodes on the aluminum and optical fibre and couples the motion of the fibre nodes to the motion of the aluminum. The tie constraint models the permanent fixation point where the FBG is integrated onto the aluminum superstructure.
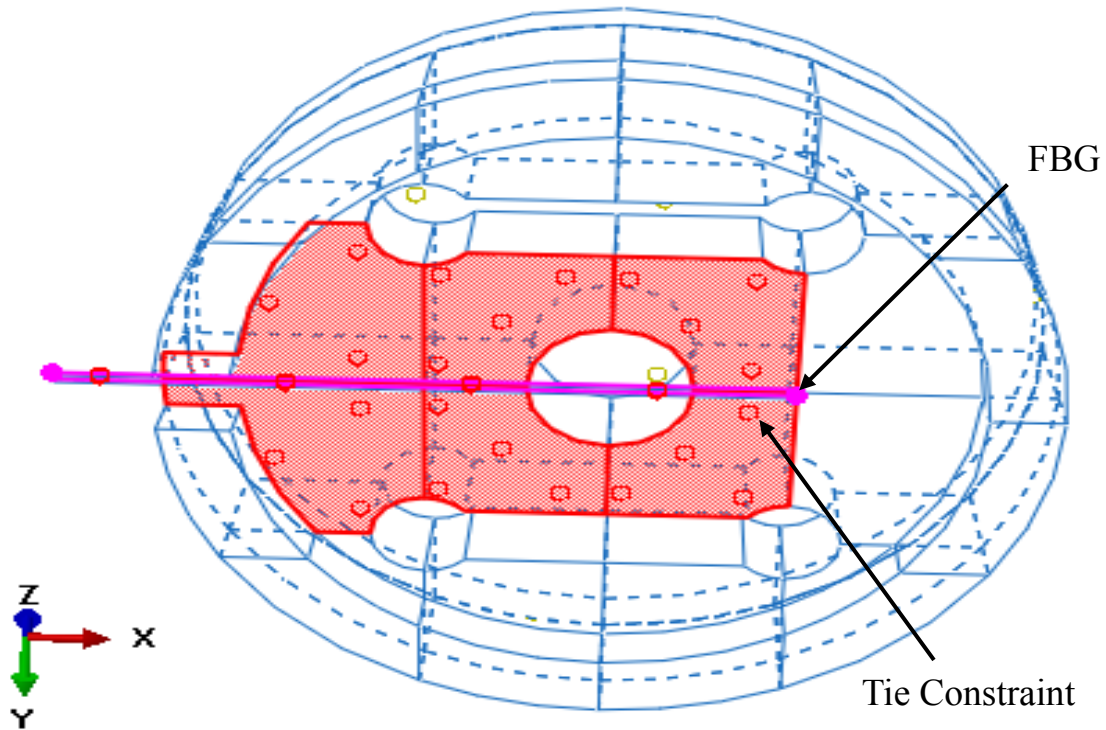
Figure 3.4: Wireframe schematic of the transducer modelled using ABAQUS Explicit. An underside view of the transducer shows a tie constraint between the FBG and aluminum superstructure. A tie constraint couples the motion of adjacent nodes on the FBG to the motion of the aluminum superstructure.

After the load and boundary conditions were applied to the model, the transducer was meshed in order to calculate the force sensitivity of the transducer. Before the final mesh was

chosen, a convergence test was performed. The convergence test was used to determine the number and type of elements for the model, as well as confirm that the model converges. Initially, linear HEX (8-node linear brick) elements comprised the model and were used to assess convergence. The criterion for convergence was that, for increasing number of elements and for an applied force of 1200 N, peak principal strain magnitude of the FBG changed less than 10% of the previous peak strain magnitude. The seed length was varied to increase the number of elements in the model and the peak principal strain magnitude was determined for each seed length. The range of seed length was 0.7 to 0.08 mm at increments of 0.05 mm. The density of elements set by the seed length in the transducer model ranged from 838 to 303,982 elements. The results of the convergence test are shown in Figure 3.5, detailed subsequently. Once the mesh density was determined, the type of elements was changed from HEX elements to tetrahedral (4-node linear tetrahedron) elements with a seed length of 0.15 mm to determine the difference in peak principal strain magnitude between element types. The results of the convergence test for the tetrahedral elements in shown in Figure 3.5.

With the final structural model of the transducer composed, to ascertain force sensitivity, the static analysis with a load range of 0 N to 1200 N was run and the strain along the axis of the fibre was solved at each load increment. The predicted peak strain of the FBG was then input to Equation 3.8 to determine the predicted shift in Bragg wavelength. A plot of predicted wavelength shift versus applied load data was constructed and a simple linear regression was performed to compute the ABAQUS model predicted force sensitivity in units of Newton per nm of wavelength shift (N/nm). The results of the predicted force sensitivity are shown in Figure 3.7 of Section 3.6.

3.4   Finite element modeling – modal analysis

Mechanical resonance is the tendency of a mechanical system to oscillate at greater amplitude when the oscillations match the systems resonance frequency (or natural frequency). Mechanical resonance can produce vibrations within the system strong enough to cause damage within the system or cause measurement error by producing large oscillations that can hinder the measurement. Standardized test headforms cannot have resonances below 2 kHz [58]. Therefore, transducers that are integrated onto test headforms cannot resonate below 2 kHz to ensure that integration of the transducer onto the head does not create resonance below 2 kHz on the aggregate head-transducer assembly.

To ascertain mechanical resonances of the transducer, a modal analysis was performed. The purpose of the analysis was to confirm that the first (lowest) resonance exceeded the requirements on mechanical resonance of helmet and crash test headforms [58]. The modal analysis is performed using ABAQUS Explicit. The properties and geometry of the model was the same as described above. The step input for the modal analysis was set to a frequency step input with 10 eigenvalues reported. The first mode (resonance) was compared to the industry standard resonance of 2 kHz, and the first three modes are reported. The results of the modal analysis of the transducer are shown in Section 3.7.

3.5   Results – convergence

The results of the convergence test for the ABAQUS structural model is shown in Figure 3.5. The outcome of the initial convergence test comprised of 8-node linear brick HEX

elements, resulted in a final structural model with a seed length of 0.15 mm and a mesh density of 57,053 elements. After the change in element topography, the outcome resulted in the final structural model comprised of 57,053 HEX (linear 8-node) elements.
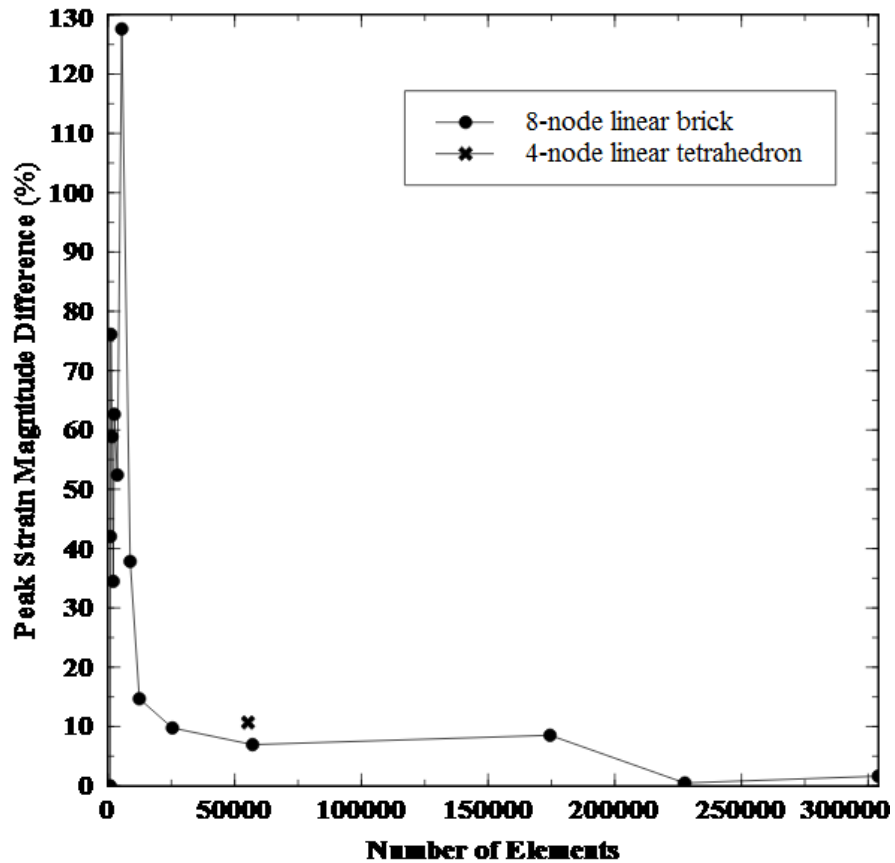
Figure 3.5: ABAQUS convergence test. Convergence test was initially done with 8-node linear brick HEX elements. The convergence criterion was that peak principal strain magnitude less than 10% of the previous peak strain magnitude. Element topography was changed to a 4-node linear tetrahedron element to determine if the peak principal strains were invariant.

3.6   Results – force sensitivity

Figure 3.6 shows the deformation of the ABAQUS structural model of the transducer under applied loads.
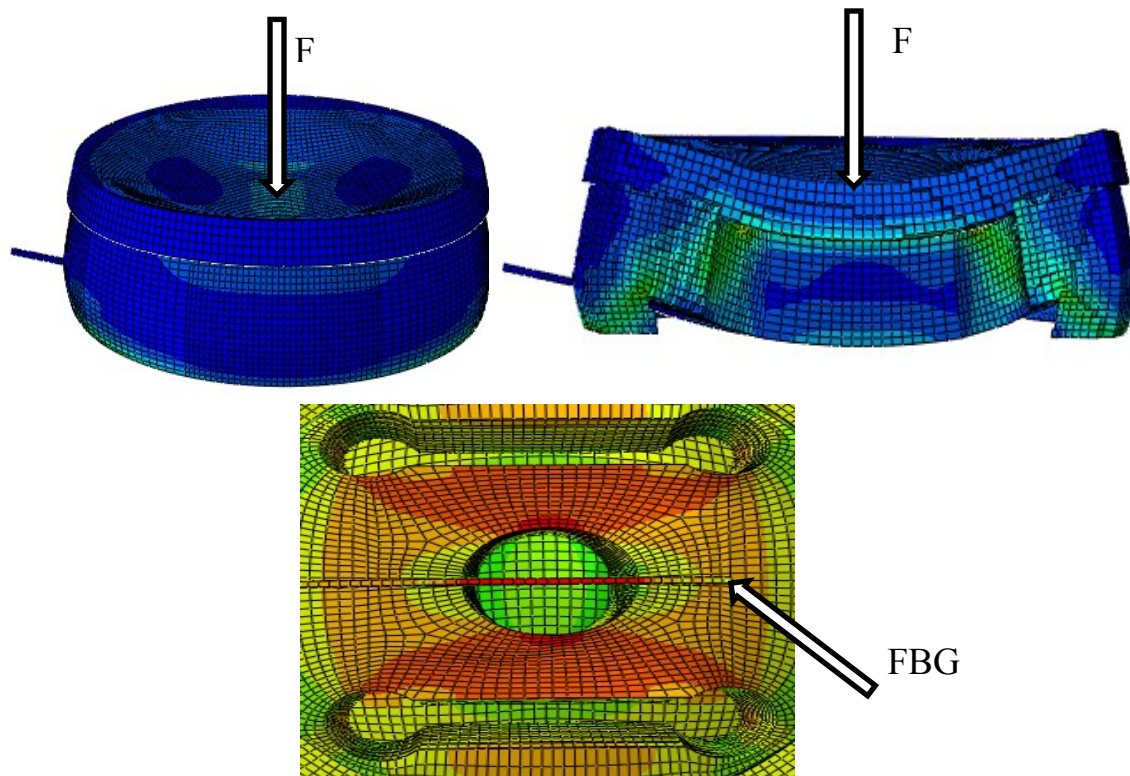
Figure 3.6: Deformation of ABAQUS structural model under applied loads. Applied loads ranged from 0 N to 1200 N and the peak principal strain magnitude of the FBG was solved for. Top left: Deformation of transducer under applied loads. Top right: Section view of fixed-fixed end beam deforming under applied loads. Bottom: Underside view of the beam showing the resulting strains along the FBG.

The ABAQUS structural model predicts a direct linear relationship between impact force and axial strain of the FBG (Figure 3.7). The model predicted a sensitivity to force of 1.06 N/micro-strain and a least-squares fit of the model data indicated a coefficient of determination of 1.0 (Figure 3.7).
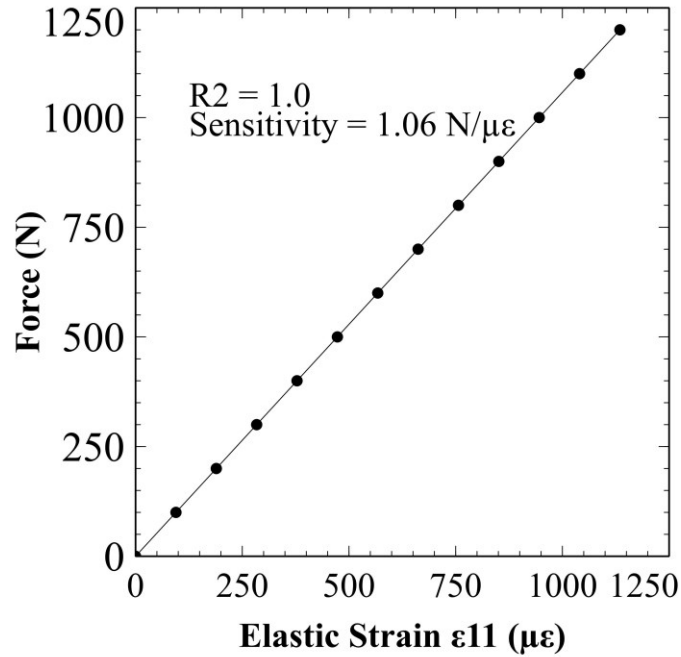
Figure 3.7: ABAQUS structural model predicted linear relationship between impact force and strain along the FBG.

The ABAQUS structural model predicts a direct linear relationship between impact force and Bragg wavelength shift (Figure 3.8). The model predicted a sensitivity to force of 873.9 N/nm and a least-squares fit of the model data indicated a coefficient of determination of 1.0 (Figure 3.8).
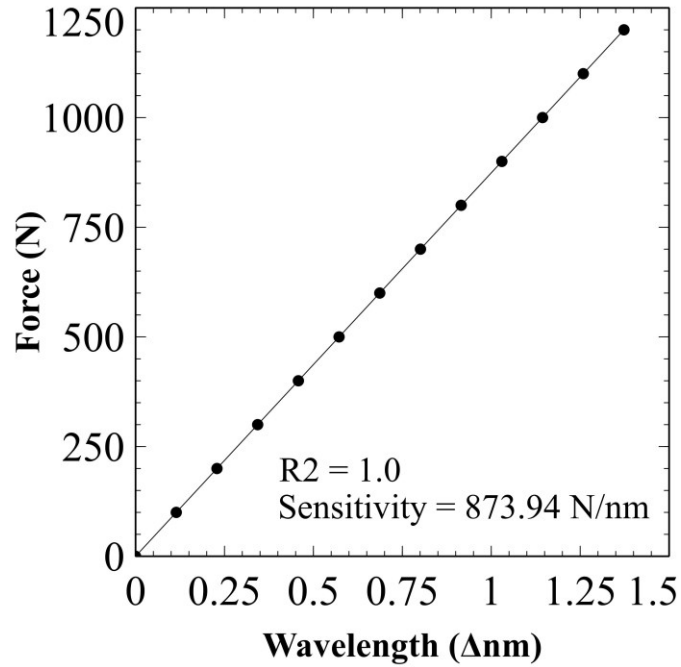
Figure 3.8: ABAQUS structural model predicted linear relationship between impact force and Bragg wavelength shift [64].

3.7   Results – structural resonance

The results from the modal analysis are shown in Figure 3.9. The ABAQUS simulations predicted the first mechanical resonance at 71.8 kHz. The first mechanical resonance is much greater than the required 2 kHz. The deformation associated with the first mode resonance is shown in Figure 3.10 and can be qualitatively described as that of the first mode of a fixed-fixed end beam.
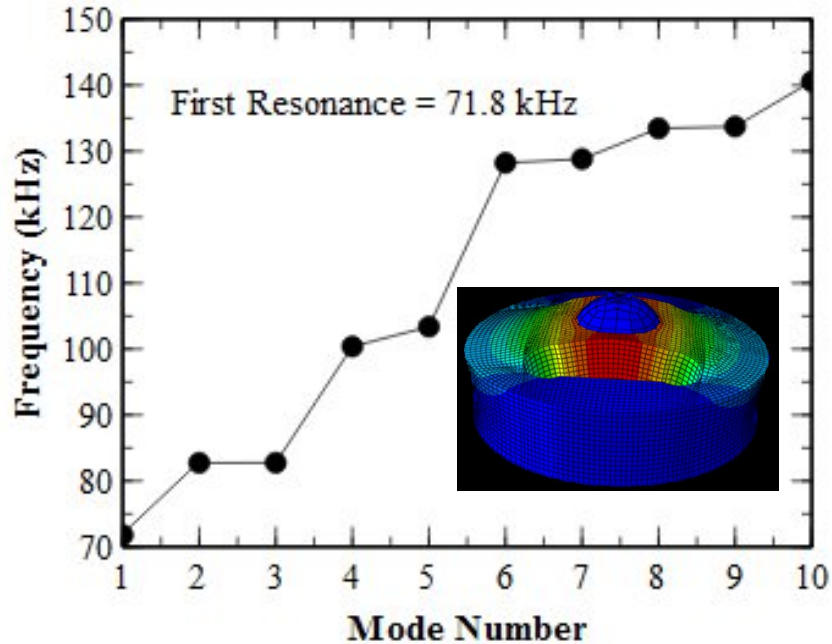
Figure 3.9: ABAQUS predicted resonances for increasing mode number. Predicted first resonance is 71.8 kHz. Inset: Deformation of the transducer associated with the first mode resonance [64].

3.8   Discussion

The design of the impact force transducer comprises an FBG that is integrated into an aluminum superstructure. Basic solid mechanics and finite element modeling was used to establish the overall geometry (major diameter = 12 mm, overall thickness = 3 mm, beam length = 5 mm, beam width = 5 mm) and transducer performance when subjected to contact forces. The results of the finite element model provided a linear relationship between impact forces and predicted induced wavelength shifts of the transducer. The predicted sensitivity to force for the finite element model was 873.9 N/nm. The first predicted resonance of the impact force transducer was 71.8 kHz, which far exceeds industry standards on mechanical resonance.

The impact force transducer provides adequate force sensitivity, survives peak loads of typical impacts, and has appropriate mechanical resonance. The fabrication and calibration of the impact force transducer is described in Chapter 4.

4 FABRICATION AND CALIBRATION OF IMPACT FORCE TRANSDUCER

This chapter discusses the fabrication and calibration of the impact force transducer. An overview of the fabrication process is described first, followed by a complete description of the calibration procedure and the calculated sensitivities to force for each transducer applied in this thesis.

4.1 Fabrication of impact force transducer

Four impact transducer (transducers 1-4) superstructures (Figure 4.1) were fabricated using aluminum (6061 T6) with a major diameter of 12 mm and an overall thickness of 3 mm. As mentioned previously, the centrally located fixed-fixed end beam has a length and width of 5 mm with a beam thickness of 2 mm. One FBG (Figure 4.1) with a Bragg wavelength centered at 1550 nm was permanently fixed to the underside of the fixed-fixed beam using a high-strength epoxy (Epoxy 907, Miller Stephenson Chemical Company Inc., Danbury CT).

Four additional impact force transducers (transducers 5-8) were fabricated using the same materials and procedure. Transducers 5-8 were used in a continuation study that will be discussed in Chapter 6. The additional force transducers have the same major and beam dimensions as the initial transducers. A single FBG with a Bragg wavelength centered at 1556 nm was permanently fixed to the underside of the beam using the same Miller Stephenson epoxy.
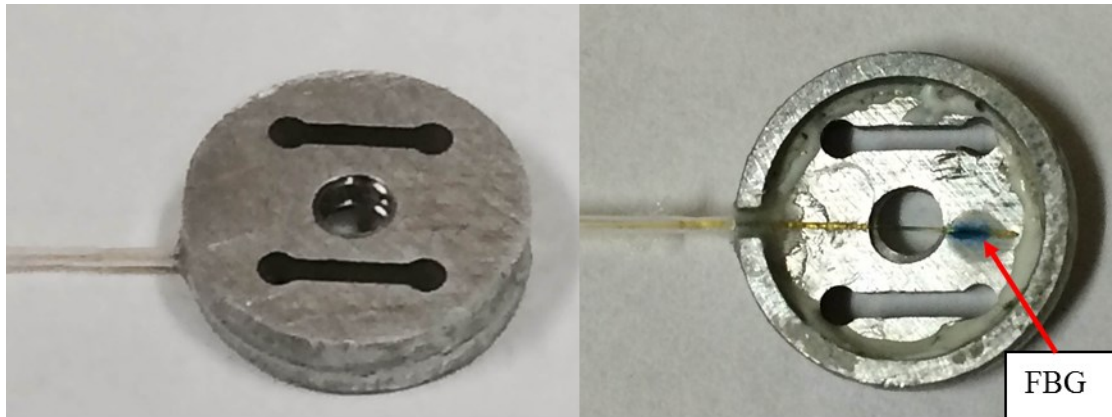
Figure 4.1: a) Topside of prototype impact force transducer. b) Underside of prototype impact force transducer.

4.2   Calibration of impact force transducer

The eight total impact force transducers (transducers 1-4 initially, transducers 5-8 subsequently) were calibrated as shown in Figure 4.2. The transducers were calibrated using a calibration apparatus (Figure 4.2) that has been extensively pre-calibrated and validated in our ongoing research. Prior to testing, calibration drops are conducted and measured impact velocity and peak acceleration are compared to calibration standards for our impactor and anvil.
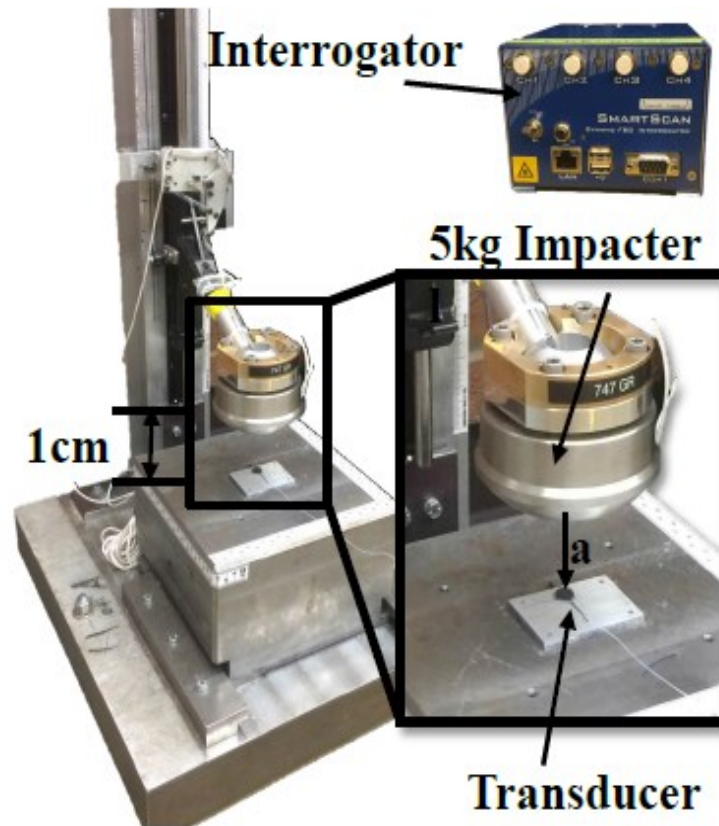
Figure 4.2: Calibration apparatus. (Inset) Impactor set 1 cm above the impact transducer. The Bragg grating interrogator is also shown [64].

The apparatus used in calibrating the impact force transducers included a falling spherical impactor (Figure 4.2). The total mass of the falling impactor was 5 kg. A piezo-electric accelerometer (Niell-Tech, Xiamen Niell Electronics Co., China, 2,000g range) was located at the mass-center of the spherical impactor. The frequency response of the piezo-electric accelerometer is typical of industry standards for crash and helmet testing [65]. The impact force transducer was fixed to a metal anvil (Figure 4.2) (AISI 4130 Steel, 161 kg mass) using a custom calibration plate to hold the transducer in place below the impactor. A compliant neoprene rubber (durometer of 70A, thickness of 1.6 mm) layer was placed on the impact

sensing surface of the transducer (Figure 4.2). The neoprene rubber was chosen to serve a dual purpose of limiting impactor acceleration to that typical of helmeted impact (range 10 g-forces or "g" to 200 g) and creating an appropriate time-duration of impact force that matched that typical of helmeted impacts (range 5 msec to 20 msec [31]). The drop distance between the impactor and force transducer was set to 1 cm (Figure 4.2) to create peak impact force magnitude of 2 kN, which brackets a realistic range of impact forces that could be experienced by a helmeted head that does not suffer skull fracture [2]. The impact force was applied by dropping the impactor onto the transducer. Applied impact force was calculated as the product of falling impactor mass (5kg) and the measured impactor acceleration. During applied impact forces, the Bragg wavelength reflected by the transducer was modulated in direct proportion to the applied impact forces.

4.3   Low-pass filtering of calibration data

Analog voltages from the pre-calibrated accelerometer were interrogated at 100 kHz and passed through an anti-aliasing filter. Analog voltages were measured using National Instruments hardware (PXI 6251, National Instruments, Austin, TX) and software (LabVIEW, version 8.5, National Instruments, Austin, TX). Wavelength shifts from the impact force transducer were acquired at 10 kHz using a commercially available interrogator (SmartScan, Smart Fibres Ltd., UK, 25 kHz bandwidth, 4 channels). 10 kHz is the de-facto minimum acquisition rate that allows compliance with the prevailing industry standard for crash or impact telemetry [65]. The acceleration data was subsequently filtered again using a low-pass filter code implemented in Matlab (version R2013a, The Mathworks, Inc., Natick, MA) at a cutoff frequency of 1,650 Hz in accordance with industry standards for impact

telemetry [65]. Like the acceleration data, impact induced wavelength shifts were low-pass filtered using Matlab (version R2013a, The Mathworks, Inc., Natick, MA) with the same industry standard cutoff frequency of 1,650 Hz.

4.4   Calculation of impact transducer sensitivity to force

Following calibration experiments, all accelerations and wavelength data were synchronized in time using a Matlab code (version R2013a, The Mathworks, Inc., Natick, MA). To synchronize the acceleration and wavelength data, the timescale that corresponds to the peaks of the acceleration and wavelength data was set to a value of zero (Figure 4.3). Once the timescales at peak values for both the acceleration and wavelength data were zeroed, the two pulses were plotted together on the same axis (Figure 4.3). Acceleration data was then down sampled from 100 kHz to 10 kHz using computing software (Matlab, version R2013a, The Mathworks, Inc., Natick, MA) to match the acquisition rate of the impact induced wavelength data. Down sampling of acceleration data to 10 kHz does not affect the fidelity of acceleration measures (10 kHz is the minimum acceptable acquisition rate for collecting acceleration telemetry [65]).
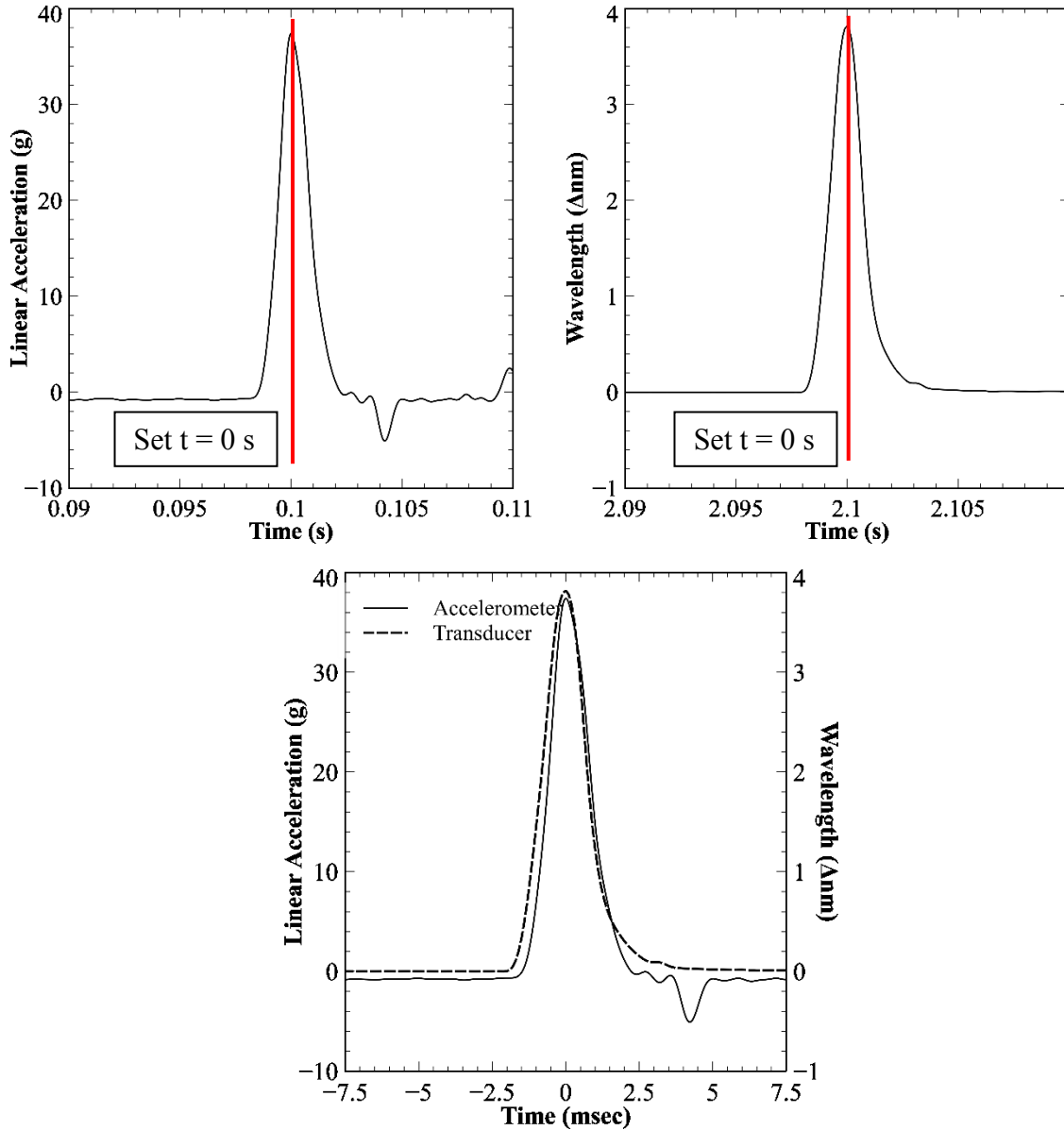
Figure 4.3: Time synchronization of acceleration and wavelength data from calibration drops. The timescale corresponding to peak acceleration and wavelength shift were set to 0 s. The acceleration and wavelength data were then plotted on the same synchronized time axis. Data is from Transducer 2.

In order to calculate the force sensitivity of the impact transducer, the acceleration of the impactor was converted to impact force by multiplying the measured acceleration by the total falling mass of the impactor. The synchronized impact force and impact wavelength data

were then plotted on a separate graph (Figure 4.4). The increasing portion of the force and wavelength pulses was used as the calibration data to calculate the force sensitivity for each force transducer (Figure 4.4). The corresponding wavelength data was set as the abscissa axis and the impact force data was set as the ordinate axis. The resulting configuration produced a calibration plot for each impact force transducer (Figure 4.4). Simple linear regression was performed to compute impact transducer sensitivity to force in units of Newtons of force per nanometer of wavelength shift (N/nm) and the coefficient of determination of the linear fit. The calibration results will be shown in Section 4.6.
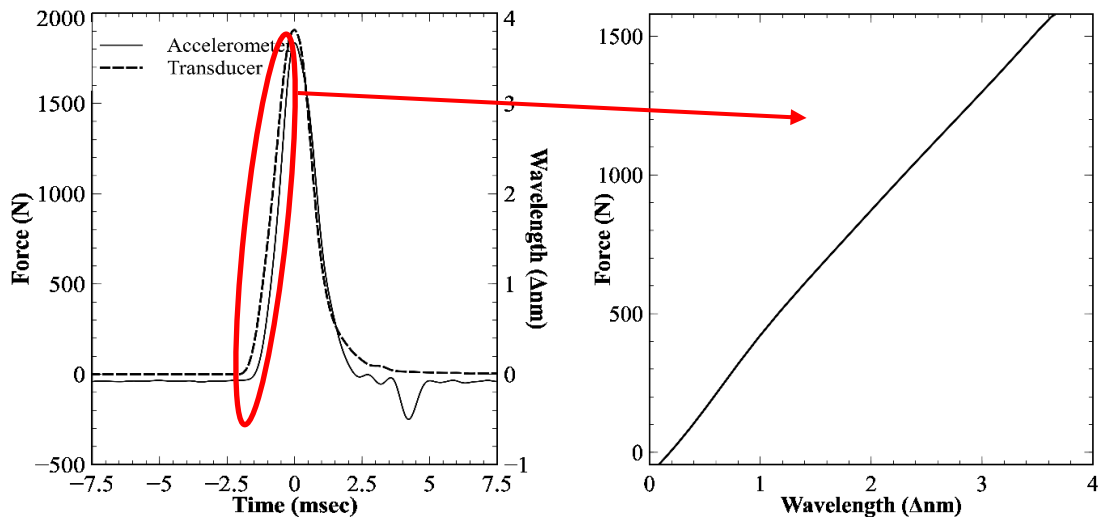
Figure 4.4: The acceleration data was converted to impact force by multiplying the acceleration data by the total falling mass of the impactor (5 kN). The corresponding wavelength data was set as the abscissa axis and the impact force data was set as the ordinate axis. The resulting configuration produced a calibration plot for each impact force transducer and simple linear regression was performed to compute impact transducer sensitivity to force in units of Newtons of force per nanometer of wavelength shift (N/nm) and the coefficient of determination of the linear fit.

4.5   Calibration results

Figure 4.5 shows the typical characteristic force (calculated from accelerometer) versus time as well as impact-induced Bragg wavelength shift from the impact transducer, versus time. Table 4.1 shows the mean time duration (Δt) of the measured pulse for the accelerometer and all transducers. The time duration of the pulse is defined as the time between first increase from pre-impact and time at which measured pulse returns to pre-impact magnitude (Figure 4.5). The mean differences between the accelerometer Δt and those of the impact transducers are 9%, 8%, 11% and 9% for transducer 1, transducer 2, transducer 3 and transducer 4, respectively. The mean differences between the accelerometer Δt and the four additional transducers are 11%, 11%, 6% and 16% for transducer 5, transducer 6, transducer 7 and transducer 8, respectively.
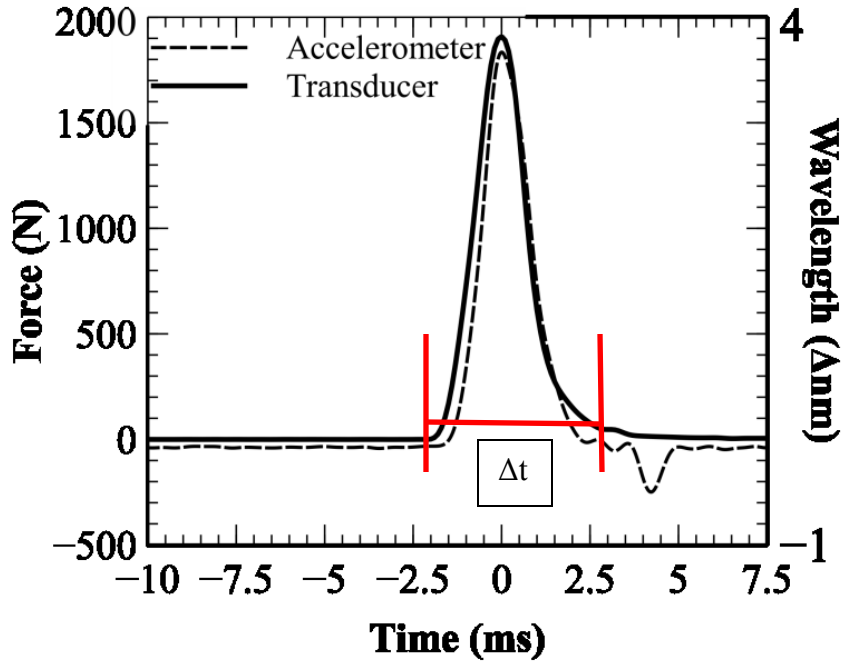
Figure 4.5: Typical impact force applied to the impact transducer (solid line, calculated from accelerometer signal) and impact-induced wavelength shift (dashed line). Solid line is a locus through data collected at 100 kHz. Dashed line is the locus through wavelength data collected at 10 kHz. Presented data is low-pass filtered at 1650 Hz corner frequency. Data is for Transducer 2.

Table 4.1: The mean time duration of the measured pulse for the accelerometer and all transducers. Each value is measured in units of milliseconds (msec).

	Δt (msec)
Accelerometer	4.6
Transducer	
1	5.1
2	5.0
3	5.2
4	5.1
5	5.2
6	5.2
7	4.9
8	5.5

Figure 4.6 shows typical impact force versus impact-induced wavelength shift characteristics for the eight transducers and summary data is in Table 4.4. Sensitivities to force were calculated using the mean sensitivity for each transducer over three calibration trials. As shown, data for all transducers exhibits linearity over the range of impact forces. The mean calculated sensitivity to force for transducer 1, transducer 2, transducer 3, transducer 4, transducer 5, transducer 6, transducer 7 and transducer 8 are 1498.4 N/nm, 549.6 N/nm, 509.8 N/nm, 832.7 N/nm, 310.8 N/nm, 303.9 N/nm, 430.3 N/nm and 335.3 N/nm, respectively. The mean coefficients of determination (R^2) are greater than 0.95 for all transducers (Table 4.2). Approximately 50 data points was used to determine the transducers sensitivity to force and the coefficient of determination.
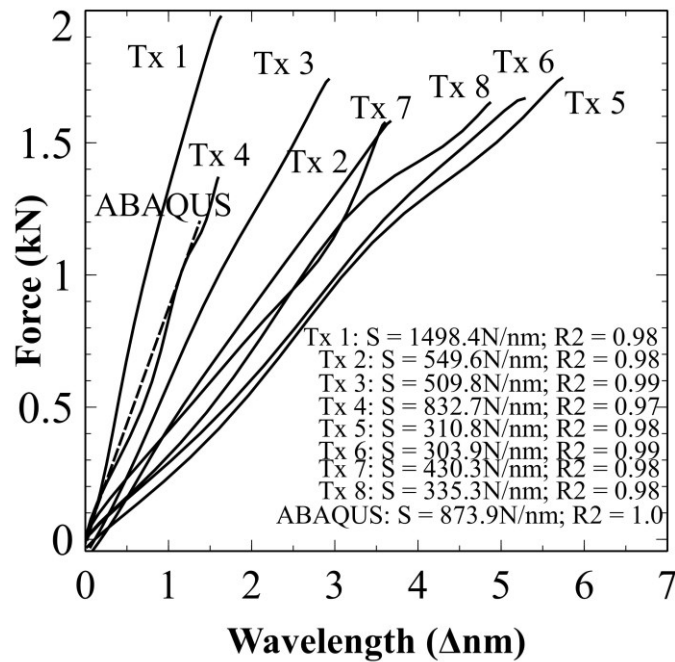
Figure 4.6: Typical calibration characteristics for eight prototypes constructed. Data presented is low-pass filtered.

Table 4.2: The sensitivity of each impact transducer and the corresponding coefficient of determination. Each transducer was calibrated three times and the mean sensitivity to force for each transducer can be found in Figure 4.5.

	Sensitivity (N/nm)	R^2		Sensitivity (N/nm)	R^2
Transducer 1	1465.4	0.96	Transducer 5	306.1	0.99
	1490.9	0.99		326.3	0.98
	1538.9	0.99		300.1	0.98
Transducer 2	549.6	0.99	Transducer 6	279.2	0.97
	535.5	0.99		309.1	0.99
	563.8	0.96		323.5	0.99
Transducer 3	467.5	0.99	Transducer 7	408.4	0.99
	515.9	0.99		457.2	0.98
	546.1	0.99		425.3	0.97
Transducer 4	868.3	0.98	Transducer 8	326.3	0.98
	832.8	0.96		327.2	0.98
	797.1	0.97		352.5	0.99

The mean sensitivity to force for all eight transducers is 596.4 N/nm, which is 32% lower than the predicted sensitivity from the ABAQUS structural and strain-optic model (873.9 N/nm). The large difference between the force sensitivities between the predicted ABAQUS model and the impact force transducers is due to the difference in Bragg grating location for all transducers. Bragg grating location on the superstructure varies slightly between transducers and, as a result, the strain transferred to the grating for a given force will also vary. Because the amount of strain coupled into the grating varies based on minor differences in grating location (each transducer will have slightly different Bragg grating location) transducer sensitivity varies.

4.6   Discussion

Calibration results exhibit repeatability and linearity over the force range of interest. Calibration results (Table 4.2) indicate that a linear fit to calibration data is appropriate ($R^2 \geq$ 0.98) and that the variance in calibration results (slope) is 10% or less for all transducers calibrated. More specifically, the standard deviation of the calculated calibration sensitivity ranges from 2% to 6% for all transducers. Overall, these calibration results are in agreement with ABAQUS strain-optic predictions of sensitivity. We acknowledge that there is variation in inter-transducer sensitivity (Table 4.2), but these differences owe mainly to minor differences in transducer fabrication. It is worth noting, however, that on average the experimental sensitivity of the collection of transducers is 32% lower that the model predicted. In Chapter 5, validation of the impact transducers in helmeted impacts is presented and the reader will note that variation in the inter-transducer sensitivity did not affect the overall validation of the transducers described in this thesis.

5   VALIDATION OF IMPACT FORCE TRANSDUCER

This chapter discusses the validation of the calibrated impact force transducers. Validation was comprised of two main activities: assessment of measurement repeatability and agreement with measures based on head acceleration; and subsequently comparison of force transducer measurements to limited data found in the literature. The impact transducers were integrated first with a magnesium test headform and then integrated with a HybridIII test headform. A complete description of the validation process is described first, followed by the results of the validation experiments. For the validation experiments only transducers 1-4 were used to assess transducer repeatability.

5.1 Experimental methods

The most commonly used headform in helmet standards is the ISO headform specified in EN 960 test headform standard (2006) [61]. The standards typically specify that headforms should be made of K1A magnesium. Magnesium K1A is selected by the standards organization because it is a low resonance alloy that will not amplify or absorb the energy of an impact and therefore does not skew the results during acquisition tests. The magnesium headform is used in many standards in North America such as the ASTM [16] and CSA [33] hockey helmet standards. Individual performance standards specify the mass of the headform, instrumentation, and support assembly used to attach the headform to the drop tower. ASTM and CSA standards use the magnesium headform to certify commercially available helmets. An in-depth look at the certification process of commercially available helmets can be found in the ASTM [16] and CSA [33] standards.

The magnesium headform was used to validate the impact force transducers first because there is limited data in the literature where force measurements have been made over the magnesium headform, and therefore comparison between the work in this thesis and that of previous researchers was possible. To validate the impact transducers, the transducers will be tested for repeatability of force measurements, and we will also establish that the time duration of the forces measured by the transducer match the time duration of head accelerations registered by an industry standard accelerometer.

Three incremental drop heights of 0.5 m, 1.0 m and 1.5 m were used to test the transducer performance. To test for transducer repeatability, five impacts were conducted at each drop height. The forces measured using the impact transducers were compared to measurements found in literature (Ouckama 2012) [63]. For the initial validation of the force transducers, three transducers (Transducer 1-3) were used.

In novel work from Ouckama *et al.* (2012) [63] peak helmet-head contact forces were measured using a variant of TekScan© as the forcing system. Twenty-five flexible force sensors arranged in a 5 x 5 array positioned on a 575 mm EN960 headform (same test headform used in our validation experiment). Three impact sites (front, side, rear) were used in the work presented by Ouckama *et al.* Five different commercially available hockey helmets were tested at an impact velocity of 4.5 m/s (corresponds to a drop height of 1 m). The results from the work presented by Ouckama *et al.* were compared to the force measurements presented in the work to assess the performance of the impact force transducers. The results of this comparison will be described in subsequent sections.

The impact force transducers were integrated one at a time with a magnesium helmet test headform (size medium, mass = 2,511.7 g, circumference = 575 mm, CADEX Inc., St-Jean-sur-Richelieu, QC, Canada). To hold the transducers in place on the headform, a custom skin was made to integrate with the transducers and fit onto the magnesium headform (Figure 5.1). A custom made impact resistant acrylic cover (3.5 mm thickness) was retrofitted to the magnesium headform and a retainer hole was created in the acrylic cover at the headform apex (Figure 5.1) to retain the impact force transducers. A trough was cut along the underside of the acrylic cover to allow a safe pathway for the transducers patch cords. The impact transducer was set into the acrylic, with a neoprene rubber cover, such that the top surface of the neoprene was less than 1 mm above the acrylic. The decision to retain the transducers using the cover was made primarily to avoid making permanent changes to the magnesium headform which would invalidate the headform certification, making it unusable for helmet certification. The purpose of the acrylic cover is to ensure that the force sensing surface and the rest of the head are continuous, but the presence of the acrylic cover is not a requirement for application of the impact transducer. The magnesium headform was then installed onto the linear drop rail and the Bauer hockey helmet (model HH1000S, size 520 - 570 mm) was fitted onto the headform.

The experimental apparatus used in this experiment is similar to the calibration apparatus discussed in Chapter 4 and the experimental set-up proposed in Ouckama (2012) [63]. The magnesium headform was installed onto a linear drop tower (Figure 5.1) with specifications meeting helmet certification standards in both North America and Europe. The total falling mass of the rigid neck and magnesium headform was 4.7 kg. The helmet used in this experiment was a commercially available Bauer hockey helmet (model HH1000S, size 520 -

570 mm). The Bauer hockey helmet has a vinyl-nitrile impact liner and the helmet was impacted onto a steel anvil covered with an elastomer pad of thickness of 1 inch and a shore A hardness of 60 ± 2 (CADEX Inc., St-Jean-sur-Richelieu, QC, Canada) in accordance with industry test standards.
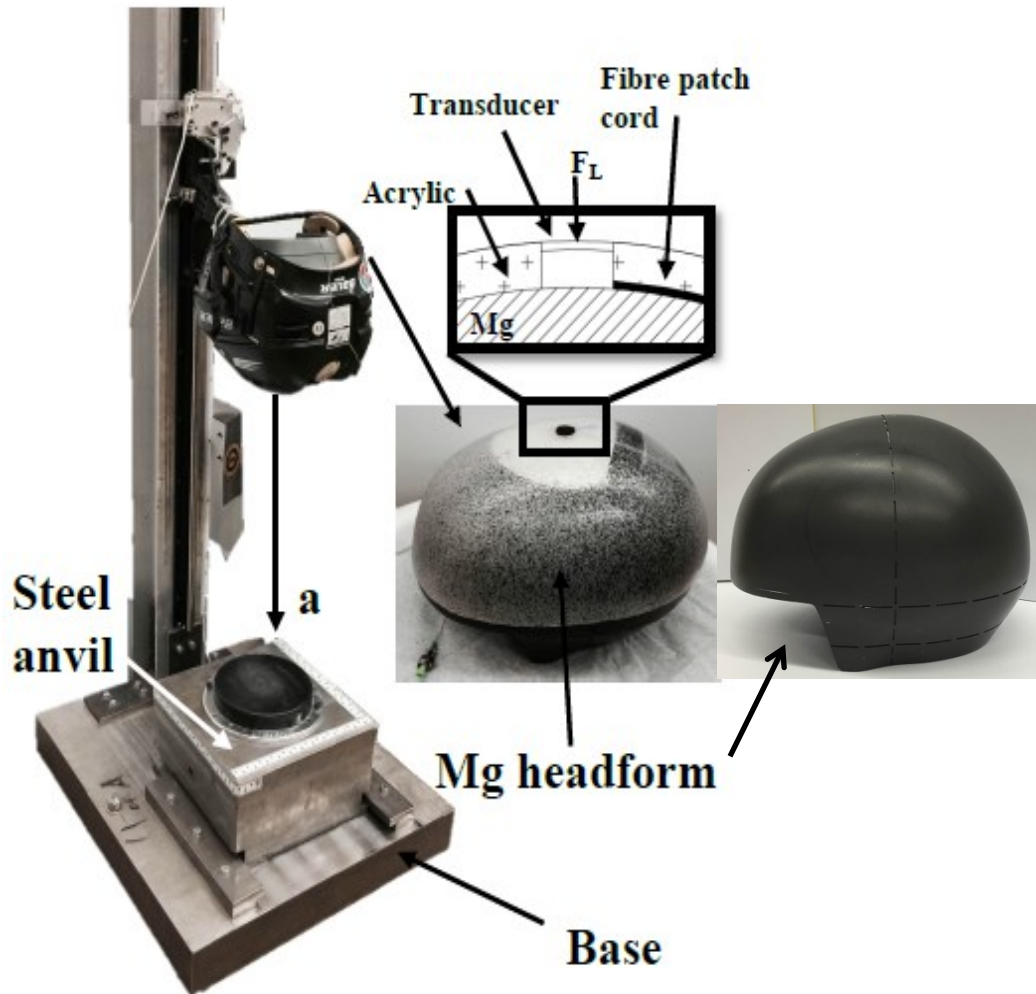
Figure 5.1: Experimental configuration used to assess repeatability of impact force transducers in helmeted impact. As shown (inset) an impact resistant acrylic skin (3.5 mm nominal thickness) with a conformal fit to the magnesium headform retains the transducer near the apex of the headform. The headform is installed on a linear drop experiment, and a hockey helmet is placed over the headform [64].

The helmeted headform was subjected to linear impacts at heights of 0.5 m, 1.0 m and 1.5 m and the configuration of the impact experiment was in conformance with the certification standard of contemporary hockey helmet (ASTM) [16]. The incremental drop heights were determined to produce a range of impact energies that simulate low energy impacts (0.5 m) up to high energy impacts (1.5 m), and also bracket the range used for certification testing. Five drop tests were conducted at each drop height to assess transducer repeatability. Headform accelerations and impact transducer wavelength shifts were measured using the same technique as those described in Chapter 4. Acceleration and wavelength data were acquired and filtered using the same spectral frequency characteristics as described in Chapter 4.

Once acceleration and wavelength data were filtered, post-processing of the data included the conversion of acceleration and wavelength data into force measurements. Wavelength shift measured using the impact force transducer were converted to forces by applying the transducers sensitivity to force which was determined in Chapter 4. The transient change in wavelength shift measured for each transducer was multiplied by the transducer sensitivity to force to determine the measured local transient force for each impact. The local impact force was compared to the net head force of the magnesium headform. The net head force was calculated using the acceleration data from the test headform. The filtered acceleration data was multiplied by the total falling mass of the headform, transducer, acrylic cover, and helmet of 5 kg. The result produced a transient net head force that was compared to the local force measurements using the impact force transducers. This comparison will be described in the next section.

Lastly, a discrete Fourier transform was performed on both the acceleration and wavelength data. The DFT allows comparison of spectral characteristics to confirm that the impact force transducer records all frequencies that the industry standard accelerometer records and therefore that no important frequency harmonics are missed.

5.2   Results – Transducer integration with magnesium headform

Figure 5.2 shows the typical net head force (calculated from the accelerometer and using the total falling mass of 5.0 kg, left axis) versus time as well as local impact force from the impact transducer (measured with transducer 2, right axis), versus time. The local impact force was measured on the test headform and the net head force was calculated by multiplying the headforms acceleration by the mass of the headform. The typical net head force and local impact force were obtained at incremental drop heights of 0.5 m, 1.0 m and 1.5 m. Each trace has been artificially shifted to allow efficient presentation of all results in a single figure. The measured net head force is 3352.7 N for a 0.5 m drop height, 7005.3 N for a drop height of 1.0 m and 11054.0 N for a 1.5 m drop height. The local impact force is 78.0 N for a 0.5 m drop height, 163.0 N for a 1.0 m drop height and 260.0 N for a 1.5 m drop height (Figure 5.2).
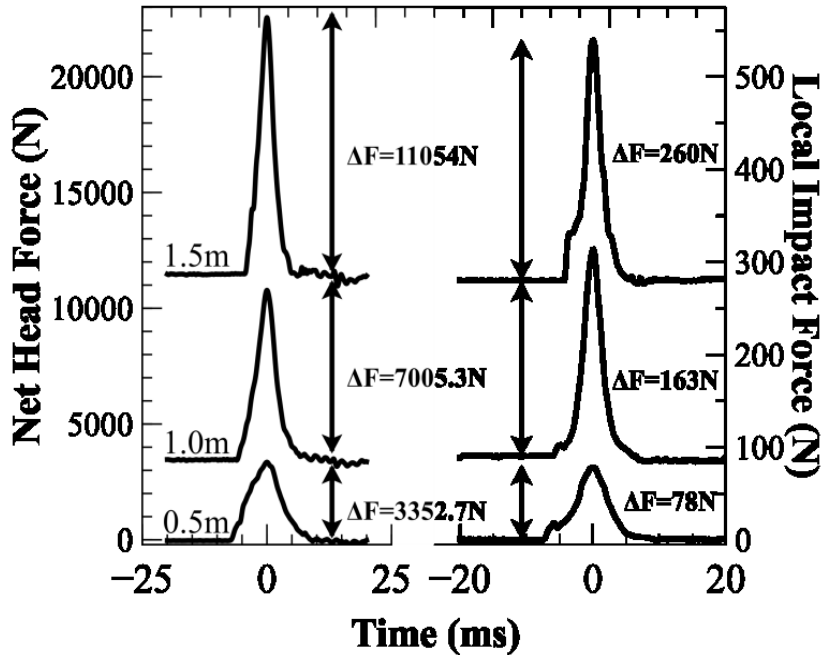
Figure 5.2: Typical net head force (left) and local impact force (right) from three headform drop heights (0.5 m, 1.0 m and 1.5 m). Local impact force is measured with transducer 2 [64].

Figure 5.3 is a bar chart showing typical variance (standard deviation) of local force measurements relative to the mean force magnitudes measured. The mean ± standard deviation of local impact force for transducer 1 is 73.2 ± 0.8 N for a 0.5 m drop height, 165.9 ± 9.5 N for a 1.0 m drop height and 211.6 ± 13.1 N for a 1.5 m drop height. The mean local impact force for transducer 2 is 71.6 ± 8.8 N for a 0.5 m drop height, 170.0 ± 29.5 N for a 1.0 m drop height and 256.3 ± 6.3 N for a 1.5 m drop height. The mean local impact force for transducer 3 is 55.4 ± 3.1 N for a 0.5 m drop height, 150.5 ± 26.3 N for a 1.0 m drop height and 262.5 ± 16.1 N for a 1.5 m drop height.
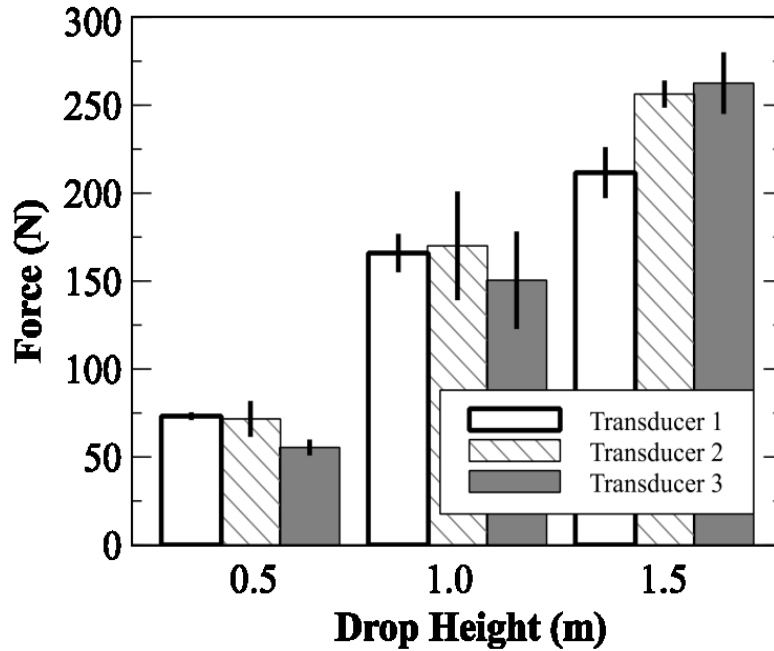
Figure 5.3: Mean and standard deviation of impact force measurements for the three prototypes constructed based on 5 drop tests [64].

Table 5.1 augments Figure 5.3 by showing the comprehensive force measurement results for transducers 1 through 3: the net head force (F_N) and local impact force (F_L) for each validation drop. The mean percentage ± standard deviation of the net head force captured by transducer 1, transduce 2 and transducer 3 is 2.24 ± 0.2%, 2.30 ± 0.3% and 2.17 ± 0.4%, respectively.

Table 5.1: The net head force (F$_N$) and local force (F$_L$) at incremental drop heights of 0.5 m, 1.0 m and 1.5 m. Five trials were performed at each drop height and the mean force measurements are shown in Figure 5.3. All forces reported in units of Newtons (N). The mean value (Top value), standard deviation (middle value), and range of values (bottom value) are presented in the table [64].

Transducer	0.5 m		1.0 m		1.5 m	
	F$_N$*	F$_L$*	F$_N$*	F$_L$*	F$_N$*	F$_L$*
1						
Mean	3032.8	73.2	7094.4	165.9	10707.9	211.6
Std. Dev	26.8	0.8	173.4	9.5	412.1	13.1
Range	3004.1 to 30673.4	71.8 to 74.3	6914.6 to 7305.9	157.3 to 182.9	9979.3 to 11164	191 to 232.4
2						
Mean	3296.0	71.6	7022.8	170.0	11051.4	256.3
Std. Dev	45.9	8.8	133.5	29.5	222.7	6.3
Range	3213.2 to 3352.7	54.4 to 78.7	6901.4 to 7276.0	161.2 to 224.0	10665 to 11321	247.9 to 265.7
3						
Mean	3270.4	55.4	6647.1	150.5	10279.9	262.5
Std. Dev	72.7	3.1	200.4	26.3	384.1	16.1
Range	3195.6 to 3392.3	51.8 to 60.7	6358.3 to 6869.9	117.2 to 182.7	9654.7 to 10812	260.0 to 289.0

* units (N)

Table 5.2 shows the time duration of impact pulse (defined as time between first increase from pre-impact force and time at which measured force returns to pre-impact magnitude) measured using the accelerometer (Δt_a) and impact transducer (Δt_t) for the helmeted impacts.

Table 5.2: The time duration of helmeted impact for both the accelerometer (Δt_a) and each transducer (Δt_t) at incremental drop heights of 0.5 m, 1.0 m and 1.5 m. Five trials were performed at each drop height. All time durations reported in units of milliseconds (msec). The mean value (top value), standard deviation (middle value) and range of values (bottom value) are presented in the table [64].

	0.5 m		1.0 m		1.5 m	
Transducer	Δt_a*	Δt_t*	Δt_a*	Δt_t*	Δt_a*	Δt_t*
1						
Mean	17.1	15.7	15.0	14.4	10.4	10.0
Std. Dev	0.3	0.4	1.3	0.9	0.4	0.5
Range	16.7 to 17.5	15.1 to 16.2	13.4 to 16.8	12.8 to 15.6	9.8 to 11.0	9.4 to 10.8
2						
Mean	16.2	15.3	15.3	14.5	9.9	9.7
Std. Dev	0.8	0.6	1.4	0.9	0.5	0.6
Range	14.6 to 17.0	14.4 to 16.2	13.2 to 16.8	13.7 to 15.8	9.0 to 10.5	8.8 to 10.4
3						
Mean	17.1	16.7	14.0	13.5	10.5	10.6
Std. Dev	0.3	1.2	1.1	0.9	0.2	0.1
Range	16.5 to 17.4	15.2 to 18.8	13.2 to 16.1	12.9 to 15.3	10.3 to 11.0	10.5 to 10.8

* units (msec)

The mean difference in time duration between the accelerometer and transducer 1, transducer 2 and transducer 3 is 0.93 msec, 0.69 msec and 0.57 msec, respectively.

Figure 5.4 shows typical spectral results from discrete Fourier transform of force measurements from both the accelerometer and datasets from the initial three transducers (Transducers 1-3). As shown, the trend of the spectral results is a general decay of amplitude with no significant harmonics registered past 250 Hz (harmonics are shown by large 'spikes' in data) for both the accelerometers and force transducers and the general characteristic shape of the Fourier amplitude versus frequency characteristics is the same between accelerometer and force transducers. This is an important characteristic of the transducers because the frequency characteristics comply with the frequency characteristics of industry standard accelerometers. Also of note, the force transducers do not exhibit resonance at 2 kHz or below. This indicates that the transducers do not resonate when subjected to impact forces at timescales typical of helmet impact (as indicated by nominally zero amplitude beyond 250 Hz) and comply with industry standard codes [61]. This is an important characteristic of the force transducers because it confirms that the mechanical resonance of the transducers will not induce resonance of the headform and therefore produce measurement error.
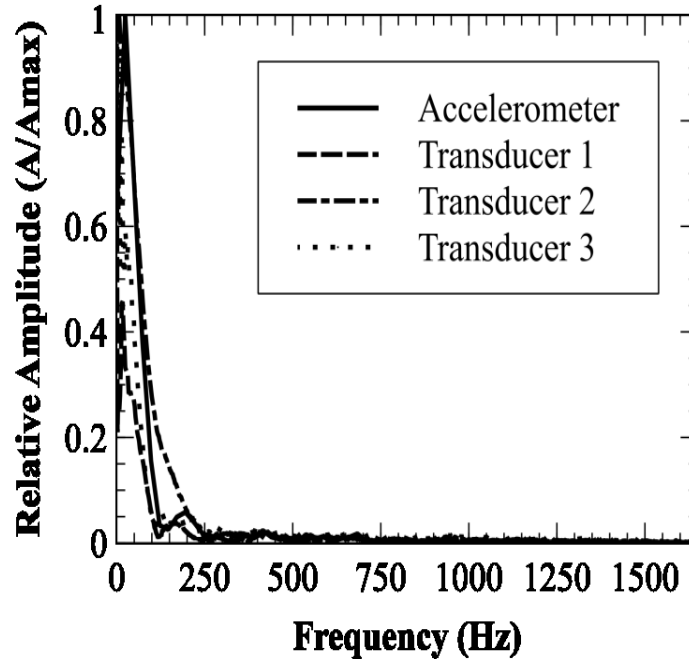
Figure 5.4: Spectral results from discrete Fourier transform of force measurements of a helmeted impact at a drop height of 0.5 m from both the accelerometer and three impact force transducers. Cutoff frequency is 1650 Hz [64].

5.3   Discussion – Transducer integration with Magnesium Headform

In measurements of local force during helmeted impact, the impact force transducers exhibit repeatability in both the force and time domain. Transducer integration with magnesium headform conveys that each transducer repeatedly captured 2% of the net head force and the standard deviation of the net head force captured by the transducers was negligible (0.2%, 0.3% and 0.4% for transducers 1, transducer 2 and transducer 3, respectively). Furthermore, the measured timescale of the force transients was in excellent agreement with acceleration measures (Table 5.2). The average difference in Δt between the accelerometer and force transducers was 0.6 msec (4% of mean Δt measured by the industry standard accelerometer).

The force magnitudes measure using the impact force transducers presented in this work are comparable to previously published data for helmeted impacts using ASTM certified hockey helmets. For similar helmets with vinyl-nitrile impact liner dropped from 1 m, the mean force magnitudes measured using the impact transducers presented in this work is 162.2 N, which is 12.3% higher than the force magnitude presented by Ouckama *et al.* (2012) [63] of 144.4 N (rear helmet impacts). Care must be taken in comparing these results because the location of the transducers (head apex) is different than the location to the results presented in the work done by Ouckama *et al.* (2012) (rear). Nevertheless, the results from the presented transducers are comparable, and further comparisons for frontal helmet impacts, Ouckama *et al.* report peak force of 136.6 N (15.8% lower than 162.2 N). Impacts to the helmet rear and helmet front zones could be seen as similar to impacts to the apex because the amount of impact liner compressed in these impacts would be similar. Despite the difference in impact locations between the presented work and the work done by Ouckama *et al.*, the forces measured using the impact transducers produced comparable force magnitudes at the desired drop height and also repeatable measurements.

The results from the impact transducer, in terms of inter-test variance in peak measured force, compare well that that presented for previous attempts in literature. In Ouckama's novel work, the maximum standard deviation (two standard deviations as indicated by error bars) in peak local force measurements is approximately 200 N (approximately 33% of local force measured), while for our results the maximum standard deviation was 59 N (17% of local force measured) (Figure 5.3, Transducer 2, 1 m drop height). The maximum standard deviation of the work presented here is 48% lower than the standard deviation presented in

the work by Ouckama *et al.* Based on these results, the variation in peak local force measured is approximately halved when using our impact force transducer.

The results from the spectral analysis of accelerometer and force transducer data (Figure 5.4) indicate that the transducer registers harmonics at 250 Hz or less, in complete agreement with results reported from the industry-standard accelerometers used for crash and helmet testing. Spectral considerations are lacking in the results which have been reported using TekScan© films and therefore it is unclear whether these films measure all important harmonics during an impact.

The validation of the impact force transducers demonstrates the transducers repeatability in both the force-time and frequency domain for helmeted impacts. The results from integrating the transducers with the magnesium test headform is promising, allowing arrays of impact transducers to be deployed on helmet test and anthropomorphic test headforms to study helmet performance and head injury. In the next section, the impact force transducers are integrated and tested using the de-facto standard ATD headform for automotive and sport head injury research: the HybridIII headform.

5.4   Transducer integration with HybridIII headform

After integrating the impact transducers with the magnesium headform, the impact transducers (Transducers 1-4) were integrated with a second industry standard test headform (HybridIII). The objective of this study was to access transducers repeatability using the HybridIII headform. An introduction to the HybridIII headform and the experimental set-up using the HybridIII headform is now outlined.

The HybridIII 50th percentile male anthropomorphic test headform is a standard impact test headform that is used in head injury analysis[11], [66], [67]. The HybridIII was a human-like male crash test dummy developed by General Motors Corporation in the 1970s to use in place of human cadavers for impact testing in their cars. The HybridIII dummy was designed to be biomechanically similar to a human cadaver and provide injury prediction measurements in automotive crash testing. The HybridIII 50th percentile male dummy is used world wild in accordance with the Society of Automotive Engineers' (SAE) and the National Highway Transport and Safety Administration (NHTSA). Originally developed and applied in automotive crash testing, the HybridIII head-neck is now used in many helmet performance studies and sport injury (to the head) prevention experiments, and is becoming a popular tool to study the biomechanics of the head and neck during simulated impacts. In the work presented in this thesis, the HybridIII head-neck was used to study the characteristics of the impact force transducers using an anthropomorphic test device (HybridIII) that can be used to study helmet-head interactions as well as possibly studying bare-head impacts.

The impact force transducers were integrated with a HybridIII 50th percentile head-neck. The experimental apparatus consisted of the same standardized drop tower as mentioned previously, except that the magnesium test headform and rigid drop pistol was replaced with an adjustable drop gimbal and a HybridIII headform (total mass of gimbal and head-neck of 16 kg, Figure 5.5). The gimbal allows full rotation of the HybridIII head to allow for multiple impact sites on the head to be tested. The HybridIII headform was instrumented with a uniaxial accelerometer (Measurement Specialties Inc. Hampton VA, model 64C-2000-360) array, allowing both linear and angular head accelerations at the head center of mass to be

determined. This validation study was conducted before the wiring of the accelerometer array was completed; therefore, the accelerations of the HybridIII head were not measured.

Unlike the transducer integration with the magnesium headform, all four impact transducers (transducer 1-4) were integrated with the HybridIII head simultaneously. A 4 transducer array was constructed (Figure 5.6) with an active sensing region of 38 mm diameter. The transducer array was placed between the aluminum skull and vinyl skin of the HybridIII headform at a location to simulate a frontal impact (Figure 5.7), a common region of impact in helmeted sports [68]. The vinyl skin was placed back onto the HybridIII head overtop the transducer array and was fitted with a commercially available hockey helmet and installed onto the linear drop tower.
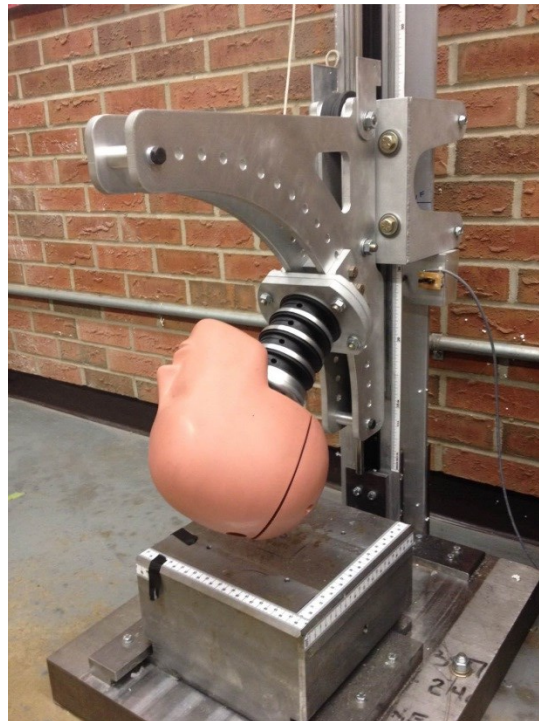
Figure 5.5: Photo of HybridIII headform and adjustable gimbal. The total falling mass of the HybridIII and gimbal is 16 kg. The HybridIII headform was used to further validate the performance of the impact force transducers.
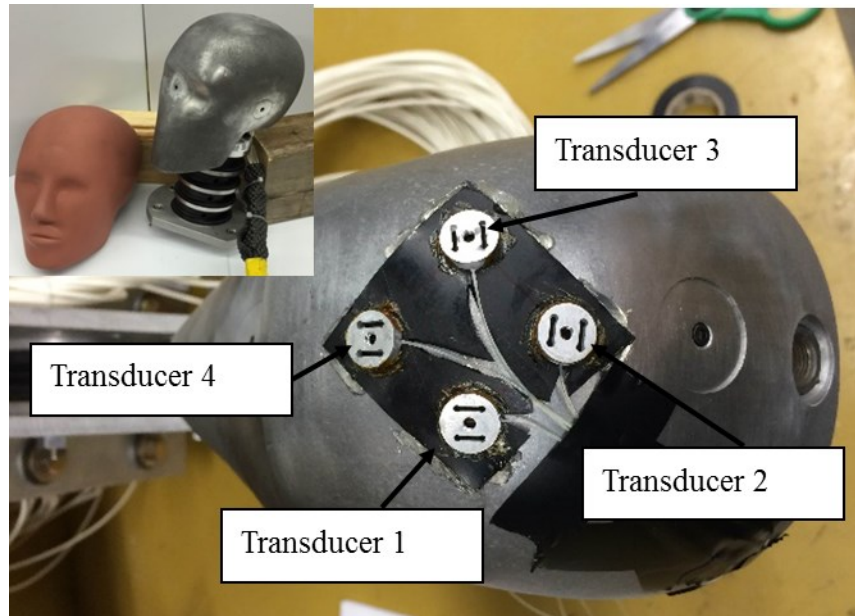
Figure 5.6: Photo of 4 transducer array integrated with the HybridIII headform. The array was placed under the vinyl skin onto the aluminum skull (Inset). The location of the transducer array is to simulate frontal head impacts.

The helmeted HybridIII headform was subjected to linear impacts at heights of 0.1 m, 0.2 m and 0.3 m. Low drop heights were chosen to protect the impact force transducers and to distinguish if the presence of the impact transducers under the vinyl skin will cause damage to the HybridIII headform. Five drop tests were conducted at each drop height to assess transducer repeatability. Under these test conditions, no damage was caused to the HybridIII head-neck and later applications of the impact transducers proved to provide no damage to the structure of the HybridIII head.
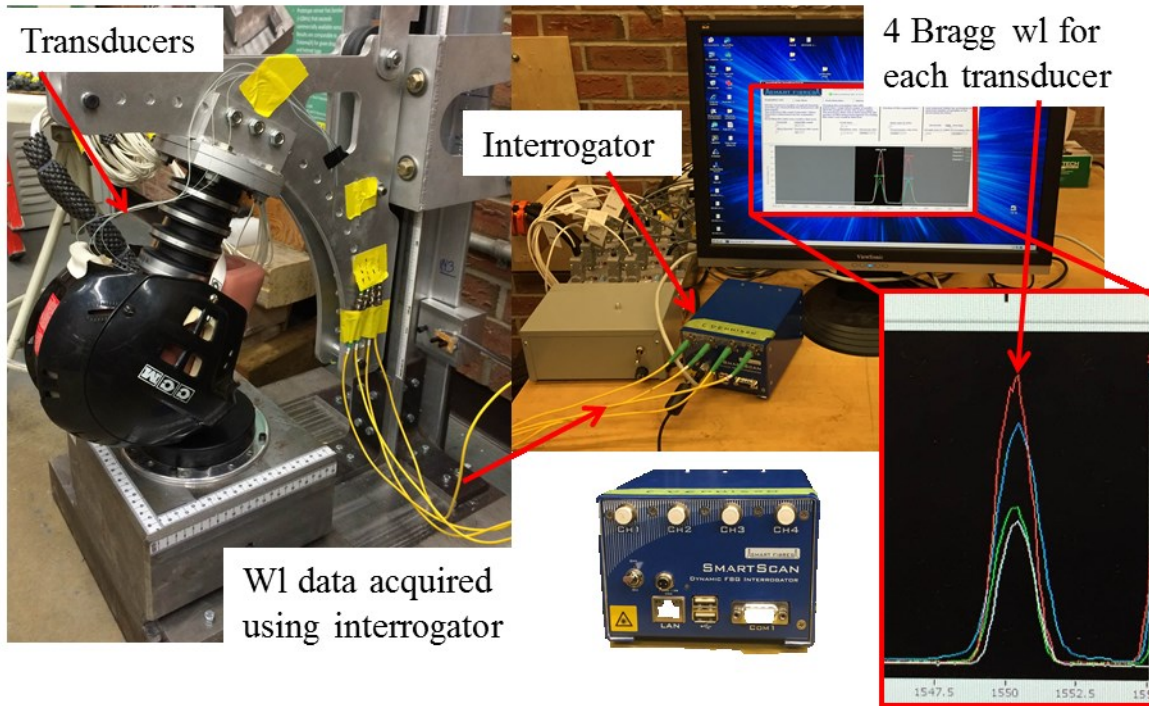
Figure 5.7: Photo of helmeted HybridIII head-neck (transducers integrated onto the aluminum skull) and gimbal installed onto the linear drop tower. Total falling mass of HybridIII and gimbal is 16 kg. Impact location is to the front of the head. Wavelength data was acquired on 4 channels using our Bragg interrogator.

Wavelength data was acquired on 4 channels using our Bragg grating interrogator (SmartScan, Smart Fibres Ltd., UK, 25 kHz bandwidth, 4 channels).

Once wavelength data was filtered, the same post-processing procedure was used to convert the wavelength data to transient force measurements. The change in wavelength shift was multiplied by the transducer sensitivity to force. This conversion results in a local transient force measurement. Once the transient force measurements were computed for each drop test, the results were compared and assessment of transducer repeatability was concluded. The results from this validation experiment using the HybridIII head-neck will be outlined in the next section.

5.5   Results – Transducer integration with HybridIII headform

The typical local impact force were obtained at incremental drop heights of 0.1 m, 0.2 m and 0.3 m. Figure 5.8 shows the typical local impact force versus time for transducer 1 (data taken from drop test 1). Each trace has been artificially shifted to allow efficient presentation of all results in a single frame. The local impact force for transducer 1 is 13.4 N for a 0.1 m drop height, 21.4 N for a 0.2 m drop height and 41.2 N for a 0.3 m drop height (Figure 5.8).
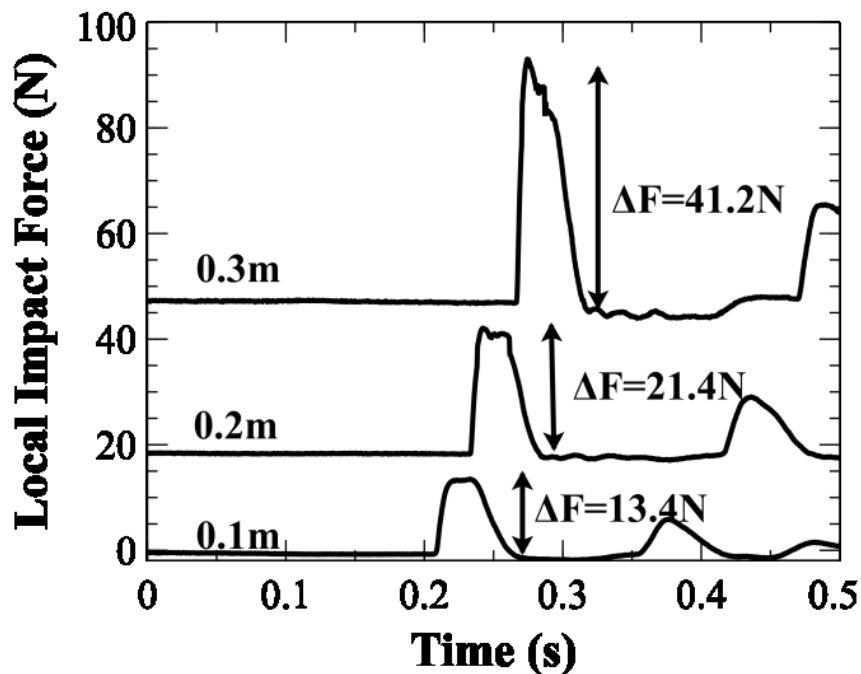
Figure 5.8: Typical net head force (left) and local impact force (right) from three headform drop heights (0.1 m, 0.2 m and 0.3 m). Local impact force is measured with transducer 1 (drop test 1).

Figure 5.9 shows the mean and first standard deviation of local impact force measurements for each impact force transducer. The mean local impact force for transducer 1 is 13.2 ± 0.8 N for a 0.1 m drop height, 22.8 ± 2.3 N for a 0.2 m drop height and 35.7 ± 3.7 N

for a 0.3 m drop height. The mean local impact force for transducer 2 is 15.4 ± 1.1 N for a

0.1 m drop height, 29.4 ± 3.6 N for a 0.2 m drop height and 36.1 ± 6.1 N for a 0.3 m drop

height. The mean local impact force for transducer 3 is 13.2 ± 0.9 N for a 0.1 m drop height,

24.1 ± 2.3 N for a 0.2 m drop height and 36.3 ± 4.1 N for a 0.3 m drop height. The mean

local impact force for transducer 4 is 12.8 ± 1.5 N for a 0.1 m drop height, 23.1 ± 2.7 N for a

0.2 m drop height and 32.9 ± 3.9 N for a 0.3 m drop height.
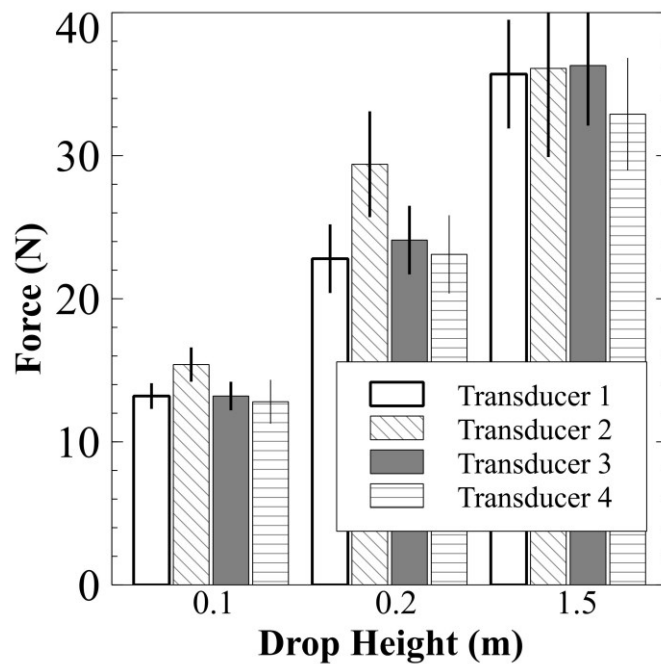
Figure 5.9: Mean and first standard deviation of impact force measurements for the transducers integrated with the HybridIII headform.

Table 5.3 shows the local impact force (F_L) and time duration of impact force (Δt) for

each validation drop. The time duration of the impact pulse is defined previously as the time

between the first increase from pre-impact force and time at which measured force returns to

pre-impact magnitude. The mean time duration ± standard deviation force for transducer 1 is

Table 5.3: The local force (F_L) and time duration (Δt) at incremental drop heights of 0.1 m, 0.2 m and 0.3 m. Five trials were performed at each drop height and the mean force measurements are shown in Figure 5.9. All forces reported in units of Newtons (N) and time durations in units of milliseconds (msec). The mean value (Top value), standard deviation (middle value), and range of values (bottom value) are presented in the table.

Transducer	0.1 m		0.2 m		0.3 m	
	Δt^+	F_L*	Δt^+	F_L*	Δt^+	F_L*
1						
Mean	13.2	13.2	12.8	22.8	13.4	35.7
Std. Dev	0.3	0.8	0.5	2.3	0.9	3.7
Range	13.1 to 14.3	71.8 to 74.3	12.2 to 13.7	19.2 to 25.7	12.4 to 14.4	27.2 to 38.1
2						
Mean	13.8	15.4	14.1	29.4	13.4	36.1
Std. Dev	0.4	1.1	0.7	3.6	1.1	6.1
Range	12.9 to 14.1	13.6 to 16.4	13.7 to 14.6	26.4 to 32.9	11.9 to 14.7	29.5 to 41.7
3						
Mean	13.1	13.2	13.7	24.1	13.9	36.3
Std. Dev	0.8	0.9	0.7	2.3	1.0	4.1
Range	12.7 to 13.4	12.8 to 14.8	13.1 to 14.2	21.4 to 29.4	12.7 to 14.8	32.2 to 40.7
4						
Mean	12.9	12.8	13.1	23.1	13.4	32.9
Std. Dev	1.1	1.5	0.4	2.7	0.9	3.9
Range	12.4 to 14.2	10.8 to 14.4	12.4 to 13.9	21.0 to 25.7	12.1 to 13.9	28.1 to 37.4

* units (N)
+ units (msec)

13.2 ± 0.3 msec for a 0.1 m drop height, 12.8 ± 0.5 msec for a 0.2 m drop height and 13.4 ± 0.9 msec for a 0.3 m drop height. The mean time duration for transducer 2 is 13.8 ± 0.4 msec for a 0.1 m drop height, 14.1 ± 0.7 msec for a 0.2 m drop height and 13.4 ± 1.1 msec for a 0.3 m drop height. The mean time duration for transducer 3 is 13.1 ± 0.8 msec for a 0.1 m drop height, 14.1 ± 0.7 msec for a 0.2 m drop height and 13.4 ± 1.1 msec for a 0.3 m drop height. The mean local impact force for transducer 4 is 12.9 ± 1.1 msec for a 0.1 m drop height, 13.1 ± 0.4 msec for a 0.2 m drop height and 13.4 ± 0.9 msec for a 0.3 m drop height.

5.6   Discussion – Transducer integration with HybridIII headform

The results from integrating the impact force transducers with the HybridIII headform provided the same characteristics as previously mentioned using the magnesium headform. In measurements of local force during helmeted impact, the impact force transducers exhibit repeatability in both the force and time domain. The mean standard deviation was 10.5 % of the local force measured. The mean standard deviation of the local force measurement is a mere 5% higher than the variability of head acceleration measurements (<5% variability, HybridIII head acceleration, see Chapter 6). Based on these results the force measurements from the impact transducers are as repeatable as acceleration measurements which are the current standard measure. Furthermore, the measured timescale of the force transients also exhibited repeatability (Table 5.3) and was in excellent agreement with the entire body of hockey helmet impact literature that shows timescales of impact ranging from 10msec to 15msec [28], [63], [69]. The average difference in Δt within an experimental impact was <10% for all 4 transducers.

The force magnitudes measured using the impact transducers with the HybridIII headform was not compared to previous literature because there is no literature to compare to. The purpose of this experimental study was to confirm transducer repeatability and to assess transducer performance with anthropometric test headforms like the HybridIII. The validation of the impact force transducers demonstrated the transducers repeatability in both the force and time domain for helmeted impacts.

The novel impact force transducers will be used to study the effects of external helmet accessories on measures of head injury risk in the next chapter.

6 EFFECTS OF EXTERNAL HELMET ACCESSORIES ON BIOMECHANICAL MEASURES OF HEAD INJURY RISK

In previous chapters, fabrication, calibration, and validation of novel impact force transducers have been presented. This chapter will focus on the application of the impact force transducers to answer a research question – does the presence of an external helmet accessory increase the risk of skull fracture and severe concussion? Background information on the importance of this study will be described first, followed by a detailed outline of the experimental set-up, and lastly, key results and conclusions.

6.1 Background

US statistics show bicycle-related injury as the second most common related to sport and recreation [70] with 44,000 cyclists injured (726 fatally) in the US in 2012 [71]. Among cycling injuries, head injuries account for the majority of hospital admissions and fatalities despite widespread helmet use [72].

In recent years, aftermarket helmet accessories (accelerometers, cameras) comprising hard and impact resistant polymers have become popular. These accessories, like external bosses and retaining clips, could focus impact forces and cause injuries. In the popular media, there is speculation that helmet mounted accessories have contributed to serious injury in high profile athletes [40]. Worldwide, the helmet standards communities have yet to adopt specific language for their integration and application with consumer helmets, possibly because the effect these accessories have on head injury risk is unclear. In the case of bicycle helmets, the CPSC Bicycle Helmet Standard states that external projections be 7 mm or less

[17], meaning that a majority of helmet-mounted accessories are larger than the CPSC guideline. If external accessories do in fact localize and magnify impact forces, wearing these external accessories, such as cameras, can be dangerous and will increase the risk of head/brain injury to cyclists. To our knowledge, there is no biomechanical data on transient head forces or the common kinematic measures used to assess head injury risk (peak linear/angular acceleration, time weighted functional (SI, HIC)) during helmeted impact with helmet-mounted accessories.

The objective of this chapter is to apply the impact force transducers to quantify changes in head-helmet interaction forces and head kinematics, both with and without helmet mounted camera hardware. A transducer array will be integrated with a HybridIII test headform and transient forces measured at the skull will be measured with/without helmet mounted camera. Statistics will be done on the results to determine significance. Head kinematics (linear and angular accelerations) of the HybridIII headform will also be measured with and without a helmet mounted camera and the results will be compared.

6.2   Experimental methods

Impacts were simulated using the same linear drop tower as mentioned in previous chapters. The impact drop tower comprised of a different adjustable drop gimbal, a HybridIII 50th percentile head and neck (combined mass of gimbal and head-neck is 10 kg), and a stationary steel impact anvil (Figure 6.1). The HybridIII headform was instrumented with the same uniaxial accelerometer array as mentioned in the previous chapter. For the purposes of this study, both linear and angular head accelerations at the head center of mass were

determined. Attached to the drop tower is a custom-made velocity gate that captures impact speed at a height of 30 mm before the impact.
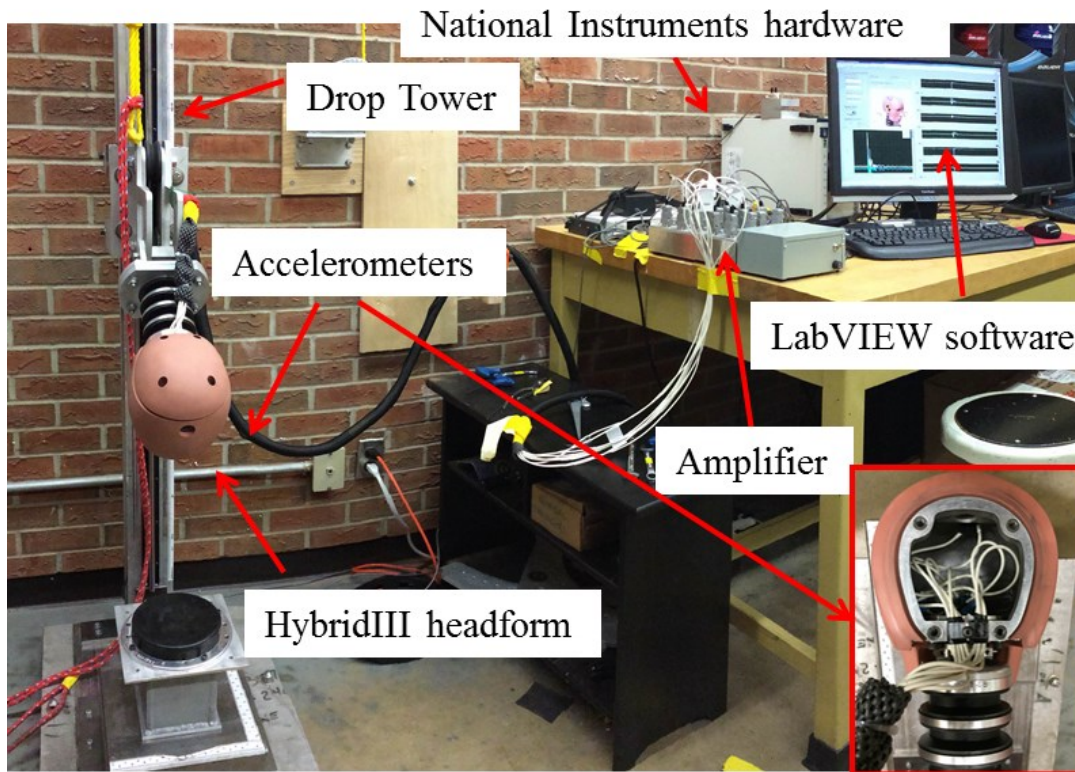
Figure 6.1: Photo of entire experimental set up. The HybridIII headform was installed onto the linear drop tower (total falling mass of HybridIII head-neck is 10 kg. Analog voltages from the accelerometer were measured using National Instruments hardware and software. Wavelength data from the force transducers were acquired using a commercially available interrogator. Inset. Photo of 9 uniaxial accelerometers positioned inside the HybridIII headform.

In total, 24 CPSC certified helmets (CCM Nexus size medium, mass: 283 ± 3 grams) were impacted. 12 of the bicycle helmets were left unmodified, and 12 helmets were equipped with an external camera accessory (GoPro vented helmet strap camera mount, GoPro Inc., San Mateo CA, mass: 46 ± 1 gram). A surrogate camera model of impact

resistant polyvinyl chloride, matching the mass (150 grams) and dimensions (70 mm x 60 mm x 30 mm) of contemporary cameras were used (Figure 6.2 and Figure 6.3).

Figure 6.2: Photo of CCM Nexus size medium helmet (mass: 283 ± 3 grams). 12 bicycle helmets were left unmodified and 12 were equipped with a GoPro vented helmet strap camera mount. A surrogate camera model made of impact resistant polyvinyl chloride (mass: 150 grams, dimensions: 70 mm x 60 mm x 30 mm).
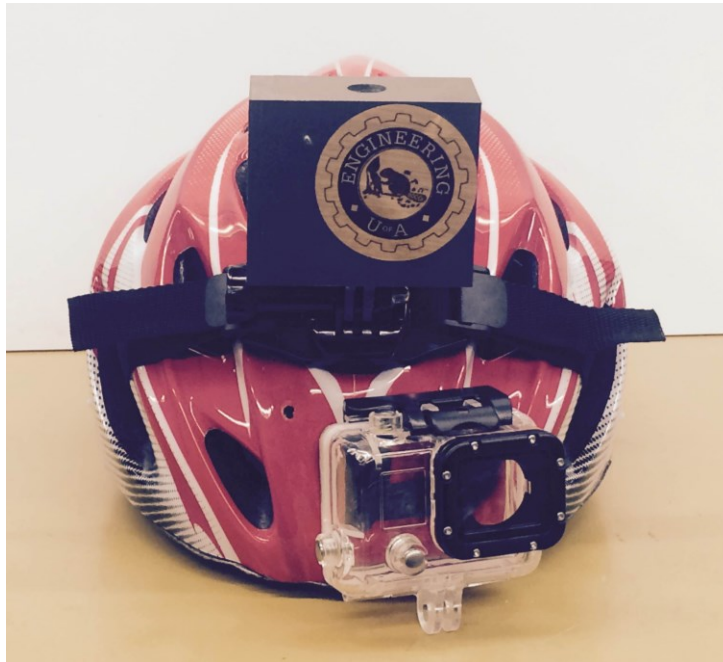
Figure 6.3: Photo of surrogate camera mounted onto the CCM bicycle helmet compared to actual GoPro camera. The surrogate camera has mass and dimensions that match that of a GoPro camera.

Four additional impact force transducers (Transducer 5-8) were fabricated and calibrated using the same protocol as previously mentioned, and used in this study. Combining with the four initial transducers, an 8 transducer array was built to measure impact forces in this study (Figure 6.4). The transducer array was integrated onto the aluminum skull below the vinyl HybridIII skin (Figure 6.4). Four transducers (Transducer 1-4) were clustered together directly below the camera mounts to measure a localized impact forces with an active sensing region of 36 mm diameter. Another four transducers (Transducer 5-8) were arranged remote from the camera mount. The 4 transducers directly beneath the camera mount captured transient force magnitudes on the region of the head beneath the accessory, while the 4 remote transducers capture forces distant (nominally 40 mm) from the accessory. The complete set-up consisting of the drop tower, adjustable gimbal, HybridIII head-neck and the external helmet accessories are shown in Figure 6.5.
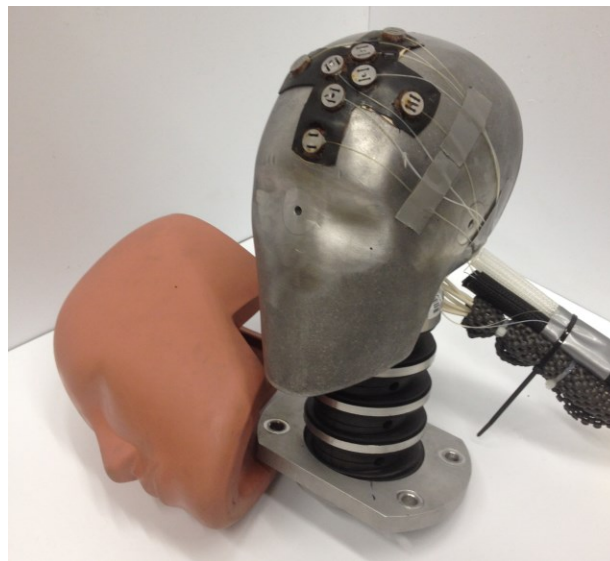
Figure 6.4: Photo of 8 transducer array integrated onto the HybridIII skull.
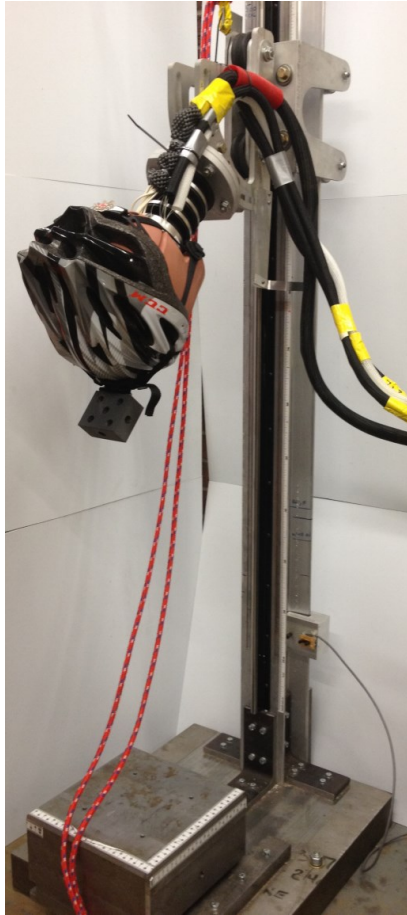
Figure 6.5: A) Photo of impact experiment showing helmeted HybridIII head-neck attached to adjustable gimbal, and steel impact surface.

The impact location for all impacts was the frontal region of the head. Impacts to the front of the head were chosen because the majority of bicycle injuries occur to the front of the head [68]. The camera mount was positioned on the front of the helmet (Figure 6.5) to simulate a direct blow to the camera (simulating the worst case scenario). Two realistic impact speeds for bicycling [27] of 4.5 m/s and 6 m/s were simulated. The two different impact speeds were used to study the interaction of the helmet accessory during high (6 m/s) and low (4.5 m/s) energy impacts. Twelve impacts were simulated at each drop speed, where six drops included an external helmet camera mount and six without.

Similarly, with the calibration and validation studies, National instruments hardware and software were used to collect impact telemetry. Acceleration data of the HybridIII head-neck were acquired at 100 kHz on all 9 channels, and impact forces measured from the transducers were acquired at 10 kHz on 8 channels. Analog voltages were anti-alias filtered using hardware, and subsequently low-pass filtered as described in previous chapters.

Linear acceleration and angular acceleration data were processed to obtain peak resultant linear and peak resultant angular acceleration as well as resultant angular velocity. Resultant linear acceleration data was post-processed to calculate the Head Injury Criterion (HIC) over the customary 15 msec window in time. HIC-15 will allow estimates of increased/decreased risk of skull fracture and serious life-threatening brain injury (as opposed to mild brain injury including concussion). Angular velocity data is used, based on the methods of Takhounts and colleagues [8], to estimate the risk of concussion (clinical description of loss of concussions > 6hrs, coded as a serious brain injury in the abbreviated injury scale). Non-parametric Wilcoxon-Rank sum tests (two tailed, significance at p<0.05) were used to test for significant differences in all measures that were compared.

6.3   Results

Summary data for all experiments is reported in Table 6.1. Figure 6.6 presents typical transient force versus time for both low velocity (6.6a) and high (6.6b). Impact forces measured using the four transducers located remote from the camera accessory did not register significant forces or alterations associated with the camera accessory.

Table 6.1: Summary data for impact kinetics and kinematics. Greyed cells indicate statistical significance (p<0.05).

	Low velocity (4.5 m/s nom.)			High velocity (6 m/s nom.)		
	No accessory	Accessory	p-value	No accessory	Accessory	p-value
Head impact velocity (m/s)	4.0 ± 0.2	4.0 ± 0.4	0.85	6.3 ± 0.4	6.2 ± 0.5	0.75
Average of peak forces (N)	59.0 ± 3.6	53.8 ± 7.3	0.23	87.0 ± 16.9	58.1 ± 5.8	0.005
Sum of peak forces (N)	176.9 ± 10.9	198.3 ± 27.0	0.17	335.0 ± 79.1	221.9 ± 24.7	0.02
Time duration of forces (msec)	10.3 ± 0.2	17.4 ± 0.7	0.005	12.1 ± 0.8	21.9 ± 1.0	0.005
Peak resultant linear acceleration (g)	72.4 ± 3.1	35.6 ± 7.4	0.003	118.4 ± 4.5	46.3 ± 3.1	0.005
Time duration of resultant acceleration (msec)	10.4 ± 0.03	14.1 ± 1.5	0.005	9.9 ± 0.09	21.1 ± 2.3	0.005
Peak resultant angular acceleration (krad/s^2)	13.4 ± 3.3	7.1 ± 2.0	0.008	12.4 ± 2.2	13.0 ± 2.9	0.58
Maximum resultant angular velocity (rad/s)	44.7 ± 4.0	31.7 ± 4.5	0.005	31.6 ± 3.5	50.1 ± 12.4	0.06
Time duration of resultant angular acceleration (msec)	12.5 ± 0.2	17.7 ± 1.8	0.005	15.3 ± 1.6	21.6 ± 5.5	0.17
HIC-15 (sec)	186.6 ± 7.0	50.8 ± 13.1	0.005	530.6 ± 34.8	115.8 ± 54.0	0.005

nb. Results are Average ± Standard Deviation (n=6)
nb. p-values calculated using two-tailed Rank-Sum test
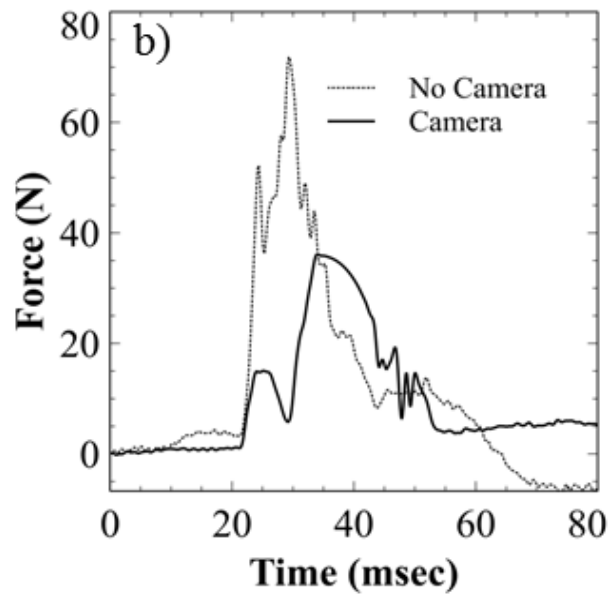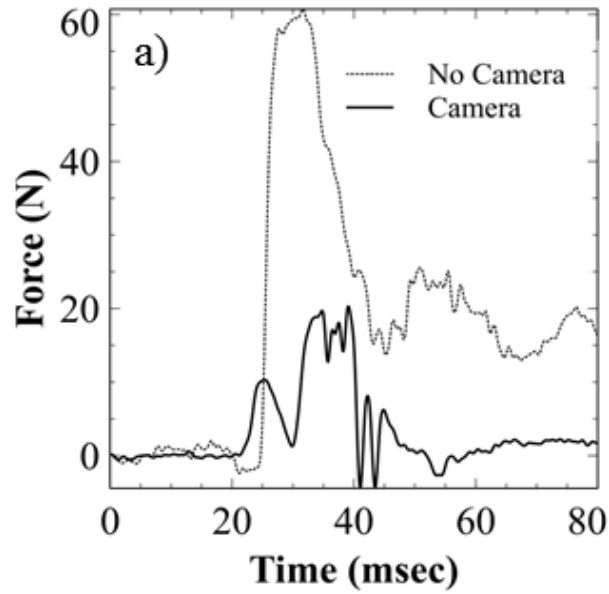
Figure 6.6: Typical impact force versus time for one of the force transducers directly beneath the camera accessory for (a) low velocity impact, both with and without camera accessory, and (b) high velocity impact.

Table 6.2 shows the average of peak forces and total force measured for each drop test for each drop scenario. Figure 6.7 – 6.10 shows the inter-test variance and distribution of data for each drop test for each drop scenario.

Table 6.2: The average of peak forces and total local force measured by transducers 1 through 4 positioned below the camera accessory mount.

	Low velocity - No camera		Low Velocity - Camera	
	Average of peak forces (N)	Sum of peak forces (N)	Average of peak forces (N)	Sum of peak forces (N)
Drop test 1	57.2 ± 7.2	171.7	57.9 ± 13.7	231.4
Drop test 2	51.6 ± 9.7	154.7	43.2 ± 5.1	172.9
Drop test 3	61.0 ± 4.9	183.0	58.4 ± 3.5	233.6
Drop test 4	61.5 ± 11.2	184.5	66.2 ± 13.2	198.5
Drop test 5	61.1 ± 5.8	183.4	53.8 ± 20.1	161.5
Drop test 6	61.5 ± 14.2	184.4	48.0 ± 10.2	191.9

	High velocity - No camera		High velocity - Camera	
	Average of peak forces (N)	Sum of peak forces (N)	Average of peak forces (N)	Sum of peak forces (N)
Drop test 1	71.5 ± 20.5	285.8	46.3 ± 23.5	185.3
Drop test 2	110.8 ± 25.3	443.2	62.5 ± 15.1	250.1
Drop test 3	66.5 ± 9.3	265.8	56.0 ± 11.2	224.0
Drop test 4	107.2 ± 19.3	428.9	59.7 ± 15.1	238.9
Drop test 5	87.3 ± 19.3	349.2	64.0 ± 11.8	192.1
Drop test 6	79.0 ± 13.2	236.9	60.2 ± 15.3	240.8
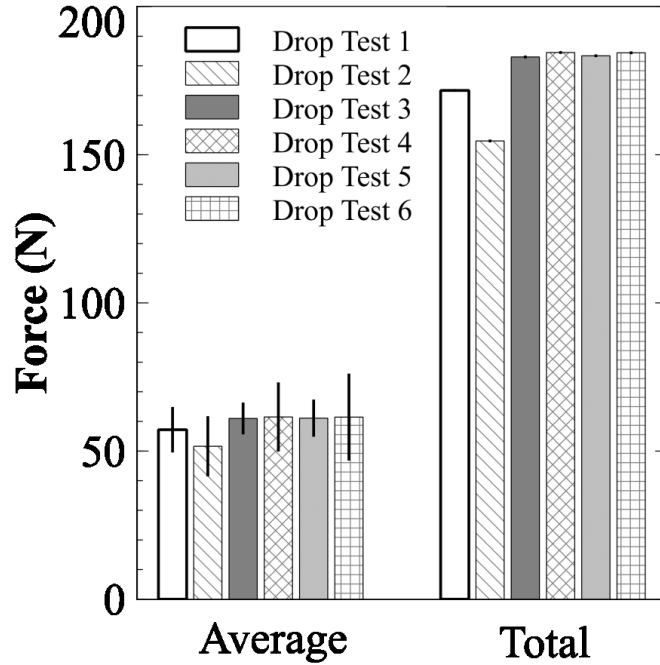
Figure 6.7: Detailed data for each impact experiment (Drop Test no.). Average of peak forces and total forces for transducers 1-4 is presented for a low velocity impact without a helmet accessory. Error bars indicate the variability of force measurements between each transducer at the given drop test no. There are no error bars on the total force measurements because the peak forces for each transducer were summed.
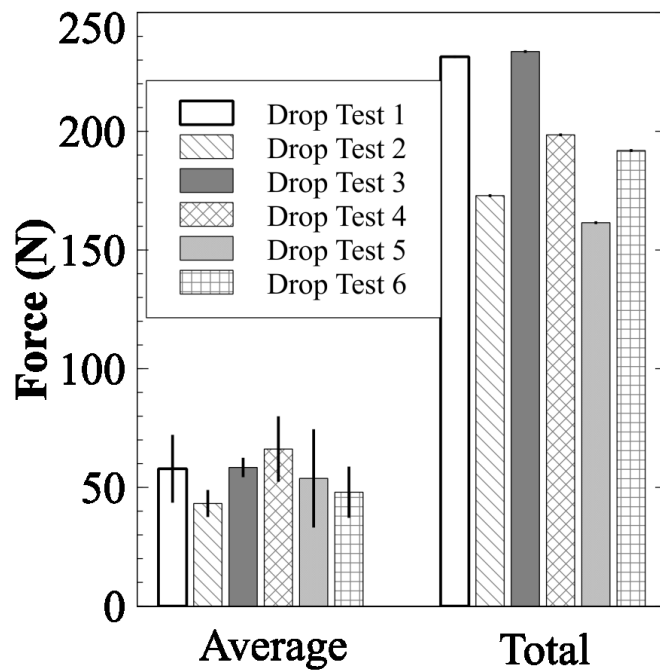
Figure 6.8: Detailed data for each impact experiment (Drop Test no.). Average of peak forces and total forces for transducers 1-4, located directly below the camera mount, and is presented for a low velocity impact with a helmet accessory. Error bars indicate the variability of force measurements between each transducer at the given drop test no. There are no error bars on the total force measurements because the peak forces for each transducer were summed.
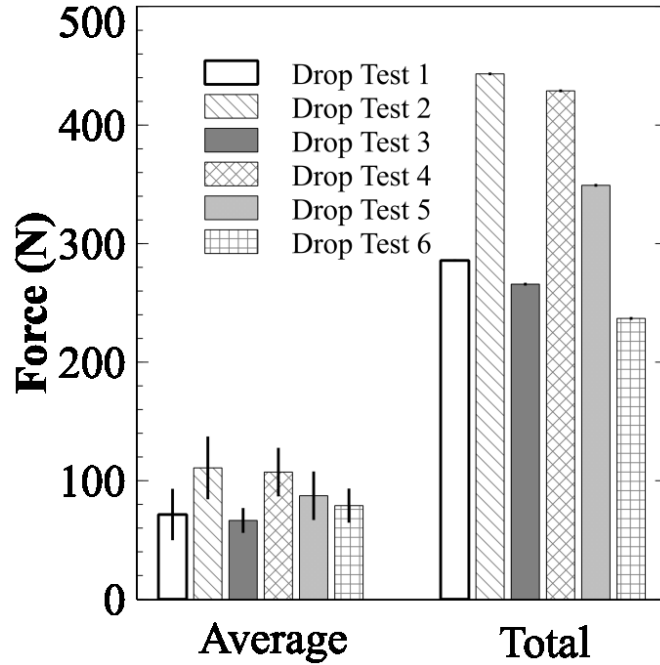
Figure 6.9: Detailed data for each impact experiment (Drop Test no.). Average of peak forces and total forces for transducers 1-4 is presented for a high velocity impact without a helmet accessory. Error bars indicate the variability of force measurements between each transducer at the given drop test no. There are no error bars on the total force measurements because the peak forces for each transducer were summed.
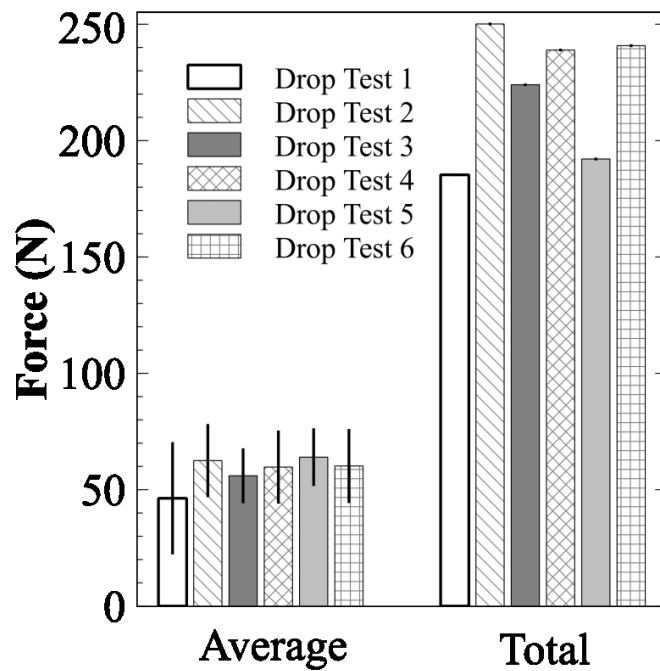
Figure 6.10: Detailed data for each impact experiment (Drop Test no.). Average of peak forces and total forces for transducers 1-4, located directly below the camera mount, and is presented for a high velocity impact with a helmet accessory. Error bars indicate the variability of force measurements between each transducer at the given drop test no. There are no error bars on the total force measurements because the peak forces for each transducer were summed.

The average of the peak forces measured by the 4 transducers directly beneath the camera mount was not significantly affected in low velocity impacts, but transient forces were of significantly longer duration (10.3 ± 0.2 msec – no camera, 17.4 ± 0.7 msec – camera, Table 6.1). In high velocity impacts, these forces were significantly lower magnitude and, again, of longer duration (12.1 ± 0.8 msec – no camera, 21.9 ± 1.0 msec – camera, Table 6.1). There was little variation between the force magnitudes measured by each transducer below the camera accessory (mean difference = 20%). Therefore, to simplify presentation of results we report average force across the four transducers beneath the camera, and subsequently the total force from the same four transducers. The average of the peak forces (Table 6.1) measured by the 4 transducers directly beneath the camera mount was not significantly affected in low velocity impacts. In high velocity impacts, these forces were significantly lower magnitude (33%). When considering the local force underneath the camera mount, we summed the peak force magnitudes across all four transducers to determine the local force underneath the camera mount. The local force increased in low velocity impact (effect not significant), but were significantly decreased in high velocity impacts (Table 6.1). High velocity impact without the camera accessory yielded the highest local force on the HybridIII skull: 443.2 N (highest force measured of all impacts presented in this work). The mean percentage of total force on the head (the head mass multiplied by head resultant linear acceleration) captured by our transducers for all drop scenarios was 4.1 ± 1.4%. Impact forces measured using the four transducers located remote from the camera accessory did not register significant forces or alterations associated with the camera accessory.

Table 6.3 shows the peak linear acceleration of the head and HIC-15 for each drop test for each drop scenario. Figure 6.11 shows the typical linear acceleration versus time for both low velocity (6.11a) and high (6.11b). Figure 6.12 and Figure 6.13 shows the linear acceleration measured for each drop test for a low and high velocity impact with and without a helmet camera accessory. Figure 6.14 and Figure 6.15 shows the HIC-15 measured for each drop test for a low and high velocity impact with and without a helmet camera accessory.

Table 6.3: The peak linear acceleration of the head and HIC-15 for each drop test.

	Low velocity - No camera		Low Velocity - Camera	
	Peak linear acceleration (g)	HIC-15 (s)	Peak linear acceleration (g)	HIC-15 (s)
Drop test 1	72.2	185.8	33.5	36.8
Drop test 2	74.6	186.2	49.2	71.9
Drop test 3	76.1	193.0	31.2	62.3
Drop test 4	70.1	180.9	29.6	43.2
Drop test 5	66.9	176.2	41.4	53.6
Drop test 6	74.5	197.2	28.3	36.9

	High velocity - No camera		High velocity - Camera	
	Peak linear acceleration (g)	HIC-15 (s)	Peak linear acceleration (g)	HIC-15 (s)
Drop test 1	111.2	482.6	49.9	97.8
Drop test 2	123.6	576.0	46.3	86.5
Drop test 3	116.2	522.7	44.2	88.9
Drop test 4	121.0	548.0	42.6	89.2
Drop test 5	122.8	562.5	43.8	96.4
Drop test 6	115.3	491.9	51.0	236.2

Figure 6.11: Linear acceleration versus time for (a) low velocity impact, both with and without camera accessory, and (b) high velocity impact.

Figure 6.12: Detailed data for each impact experiment (Drop Test no.) for linear acceleration for a low velocity impact with and without camera accessory.

Figure 6.13: Detailed data for each impact experiment (Drop Test no.) for linear acceleration for a high velocity impact with and without camera accessory.

Figure 6.14: Detailed data for each impact experiment (Drop Test no.) for HIC-15 for a low velocity impact with and without camera accessory.

Figure 6.15: Detailed data for each impact experiment (Drop Test no.) for HIC-15 for a high velocity impact with and without camera accessory.

Overall, the presence of the camera accessory reduced peak acceleration (51% - low velocity, 61% high) and increased the time duration of the linear accelerations (36% - low, 113% - high) associated with the impact, with both effects being significant (Table 6.1). Significantly lower HIC-15 (73% - low velocity, 78% - high) was associated with impacts where the helmet was fit with a camera accessory.

Table 6.4 shows the peak angular acceleration and angular velocity of the head for each drop test for each drop scenario. Figure 6.16 shows the typical angular acceleration versus time for both low velocity (6.16a) and high (6.16b). Figure 6.17 and Figure 6.18 shows the angular acceleration measured for each drop test for a low and high velocity impact with and without a helmet camera accessory. Figure 6.19 and Figure 6.20 shows the angular velocity measured for each drop test for a low and high velocity impact with and without a helmet camera accessory.

Table 6.4: The peak angular acceleration and angular velocity of the head for each drop test.

	Low velocity - No camera		Low Velocity - Camera	
	Peak angular acceleration (krad/s^2)	Peak angular velocity (rad/s)	Peak angular acceleration (krad/s^2)	Peak angular velocity (rad/s)
Drop test 1	18.4	53.0	4.2	38.3
Drop test 2	10.8	49.3	6.1	31.0
Drop test 3	9.5	48.3	5.8	38.3
Drop test 4	17.3	46.1	10.3	39.3
Drop test 5	11.9	41.5	8.6	48.3
Drop test 6	12.1	42.3	7.5	45.6

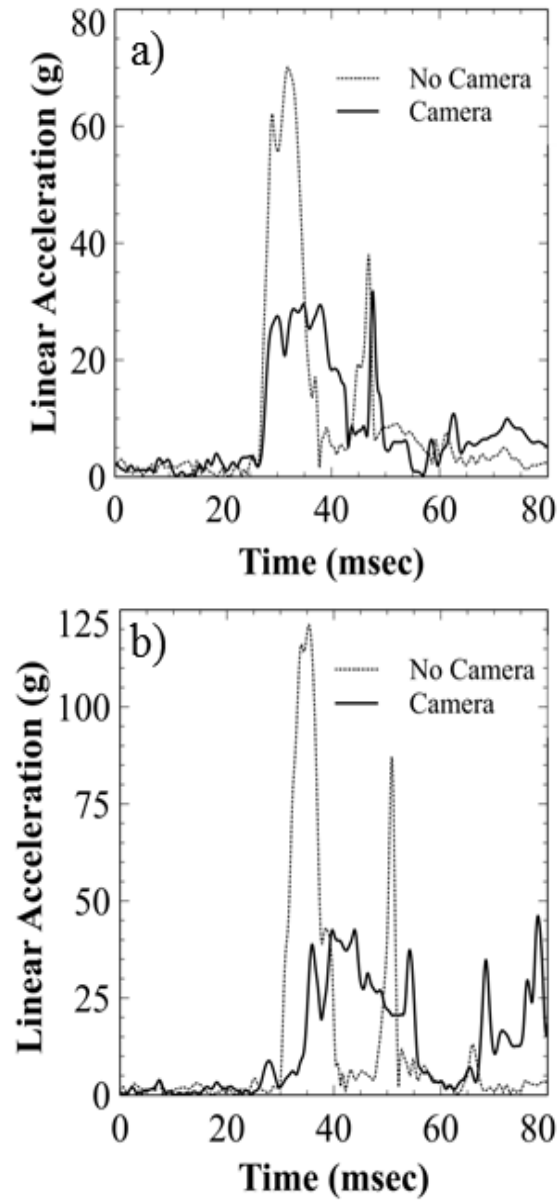|	High velocity - No camera		High velocity - Camera	
	Peak angular acceleration (krad/s^2)	Peak angular velocity (rad/s)	Peak angular acceleration (krad/s^2)	Peak angular velocity (rad/s)
Drop test 1	12.1	30.9	14.2	67.7
Drop test 2	13.8	23.7	14.1	61.2
Drop test 3	13.6	38.3	16.7	64.3
Drop test 4	14.8	29.4	12.4	44.0
Drop test 5	11.9	34.3	13.5	67.6
Drop test 6	8.1	30.4	7.2	25.9
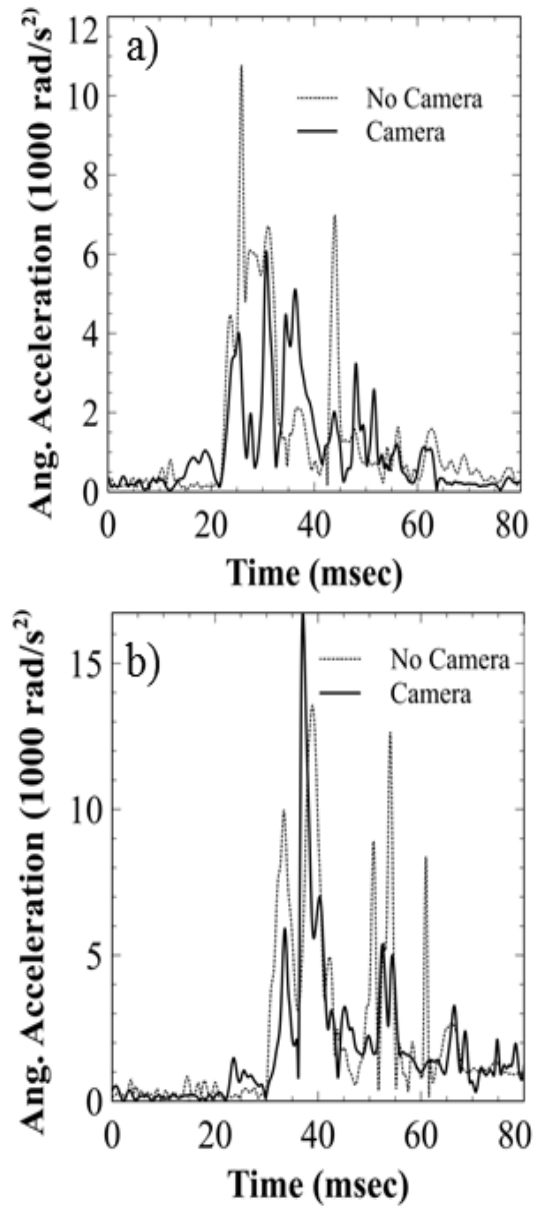
Figure 6.16: Angular acceleration versus time for (a) low velocity impact, both with and without camera accessory, and (b) high velocity impact.
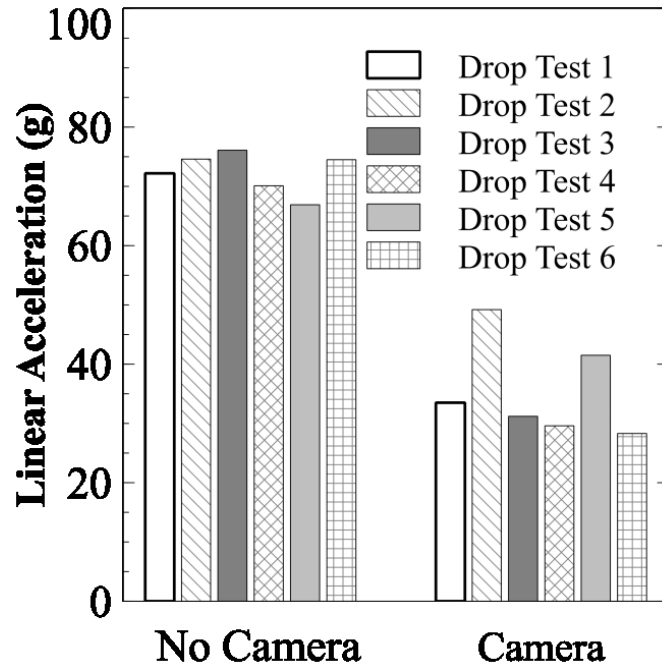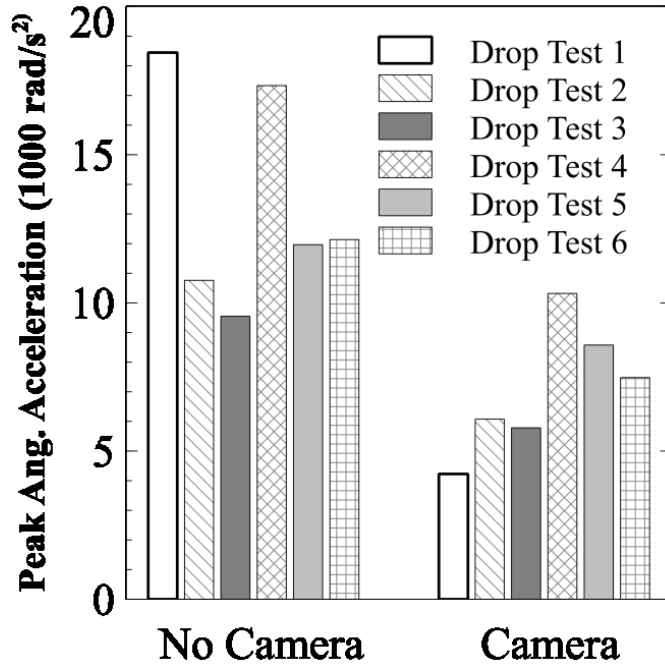
Figure 6.17: Detailed data for each impact experiment (Drop Test no.) for angular acceleration for a low velocity impact with and without camera accessory.
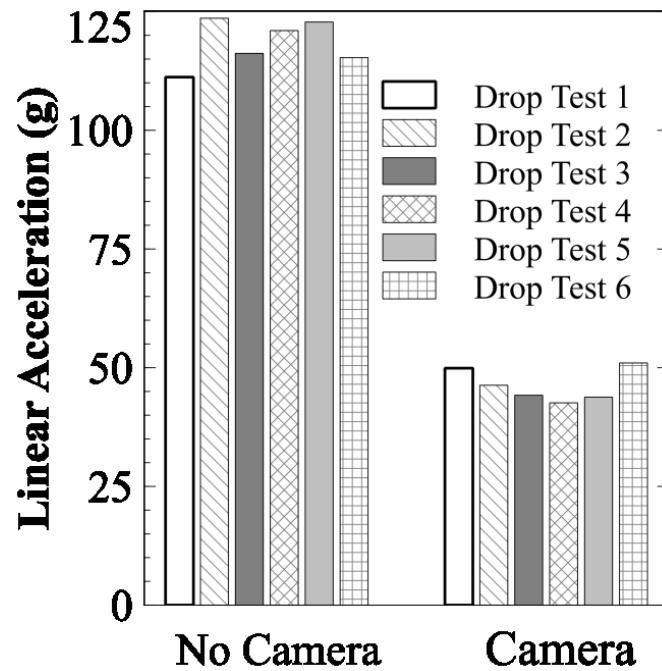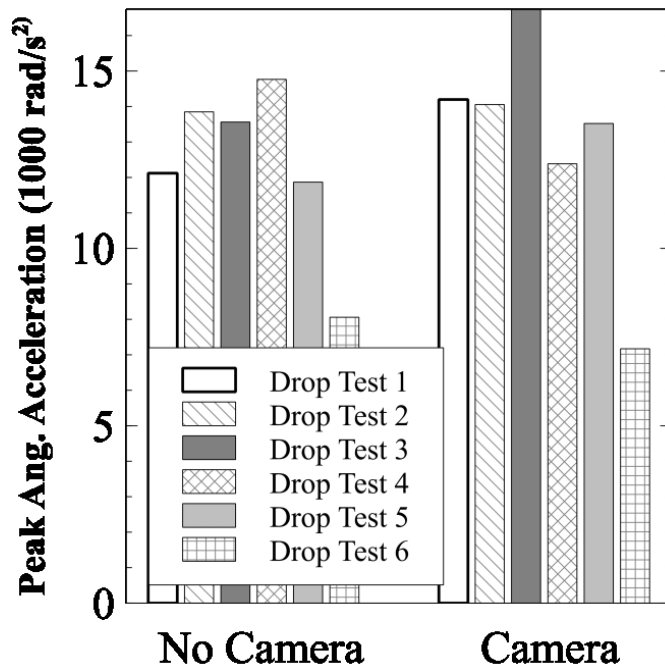

Figure 6.18: Detailed data for each impact experiment (Drop Test no.) for angular acceleration for a high velocity impact with and without camera accessory.
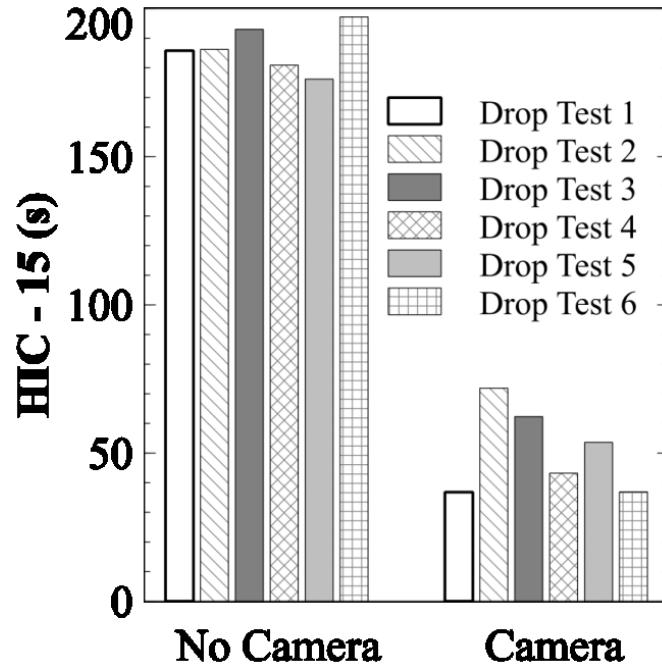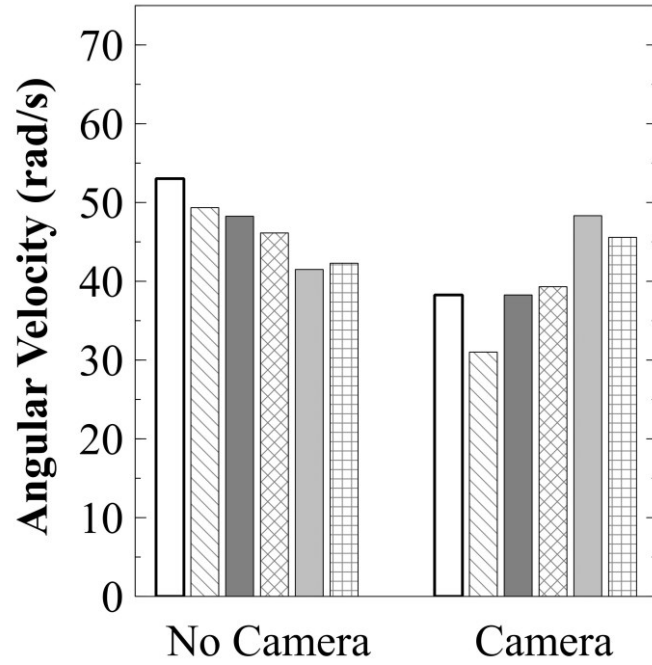
Figure 6.19: Detailed data for each impact experiment (Drop Test no.) for angular velocity for a low velocity impact with and without camera accessory.
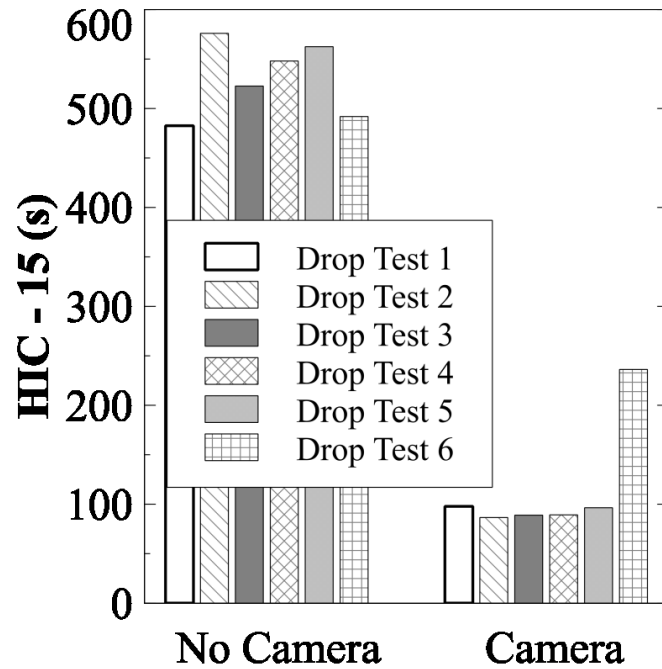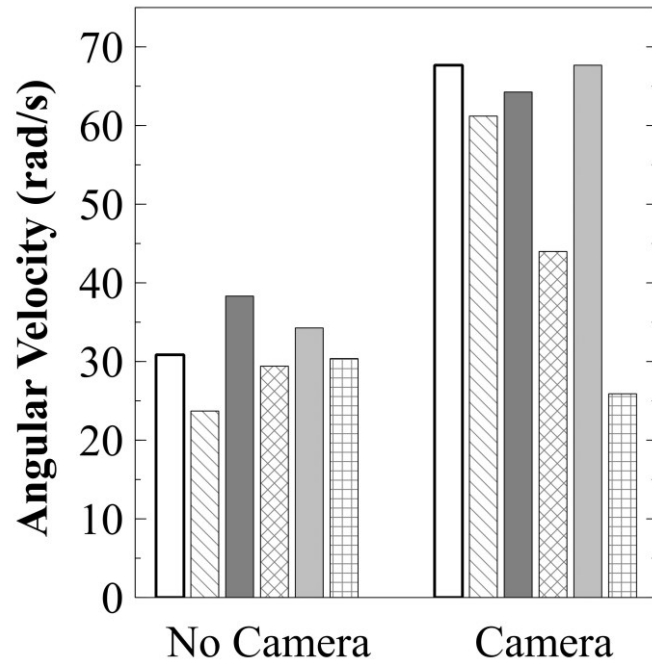

Figure 6.20: Detailed data for each impact experiment (Drop Test no.) for angular velocity for a high velocity impact with and without camera accessory.

For low velocity impacts, peak angular accelerations were significantly lower (47%) when the helmet was fit with the camera accessory. For high velocity, angular accelerations were on average higher (5%). The effect was not significant (Table 6.1). Peak angular velocities were lower (14%) in low velocity impacts with the camera accessory (result not significant). In high velocity impacts to the camera accessory, peak angular velocity was 77% higher, on average, and the effect was significant (Table 6.1).

Table 6.5 shows the characteristic helmet damage observed post impact. The table outlines the number of helmets damaged and a summary of damage to helmet mounted accessories.

Table 6.5: Characteristic helmet damage observed post impact, corresponding number of helmets with noted damage, and summary of damage to helmet mounted accessories.

Damage score	Picture of damaged helmet	Damage score description	Number of damaged helmets	Broken accessory components
0		No damage	n = 0	-
1		Shell damaged, no visible fracture of liner	n = 1	-
2		Shell damaged, obvious fracture of liner	n = 6 (low, no accessory) n = 1 (high, no accessory)	-
3		Shell damaged, obvious liner fracture, significant reduction in liner thickness due to impact related compression	n = 4 (high, no accessory)	-
4		Shell damaged, obvious liner fractures, significant reduction in liner thickness, camera mount penetrated external shell and was embedded in liner	n = 6 (low, accessory) n = 6 (high, accessory)	Components intact (n = 3), Accessory mount (n = 4), Accessory buckle (n = 5)

6.4   Discussion

Based on the results from this study, the presence of the external camera accessory altered the impact forces and the kinematics of the head by interacting with the flat anvil prior to the helmet. The average of the peak forces measured by the 4 transducers directly beneath the camera mount was not significantly affected in low velocity impacts, but transient forces were of significantly longer duration. In high velocity impacts, these forces were significantly lower in magnitude and, again of longer duration. When considering the total force measured, total force increased in low velocity impact (effect not significant), but were significantly decreased in high velocity impacts. High velocity impact without the camera accessory yielded the highest total force on the HybridIII skull (443.2 N).

The impact force measures (Table 6.1) suggest that addition of camera accessories does not increase risk of skull fracture. Work from Yoganandan and colleagues [2] suggests that for impacts at 3.4 m/s to 8.0 m/s, fracture of the frontal bone was associated with peak forces ranging from 6 kN to 14 kN. In this study, the maximum recorded impact forces under the camera accessory approached 300 N (450 N for the impacts without the camera), at least an order of magnitude smaller than what the biomechanical literature for direct (un-helmeted) impact would suggest as sufficient for skull fracture. Based on the transient forces measure using our novel impact force transducers, the presence of an external helmet accessory did not increase the risk of skull fracture. In fact, the forces measured in this study suggest the risk of skull fracture goes down significantly with the presence of an external helmet accessory.

When considering injury risk based on peak linear acceleration and HIC-15, our results suggest that the presence of the camera accessory decreased risk of severe or life threatening head and brain injury. Mertz and colleagues [73] propose that 5% risk of skull fracture in the adult male population can be associated with approximately 180 g peak linear acceleration (and HIC-15 of approximately 690 sec.), and for severe brain injury (e.g. AIS4+: large contusions and subdural, subarachnoid, and intracerebral hematomas with diffuse axon indications) with HIC-15 of 700 sec. The highest accelerations in our work approached 125 g (6m/s, no camera) which corresponds to less than 0.5% risk of skull fracture, and the highest HIC-15 approached 563 sec. (6m/s, no camera), corresponding to roughly 2% risk of skull fracture, and <2% risk of AIS4+ brain injury. Peak acceleration and HIC-15 associated with the 6 m/s impacts to the camera accessory were less, suggesting relatively less risk of injury in direct impacts to the camera. It is important to acknowledge that the risk curves of Mertz and colleagues were developed for automotive injury to the un-helmeted head. The injury biomechanics of the helmeted head depend on the specific impact and head-helmet interactions which may not be representative of automotive impacts. Therefore, the increases and decreases of injury risk based on our linear kinematics should be viewed as estimates of injury risk.

In low velocity tests, impacts to the camera accessory resulted in decreased angular acceleration. Based on work done by Takhounts *et al.* (2013) [9] reduced angular acceleration would suggest decreased risk of severe concussion. Conversely, in high velocity impacts, angular accelerations increased. The increase in angular acceleration was not significant (p=0.58), however, on average, angular acceleration increased with a camera

accessory. The increase in angular acceleration could suggest an increased risk of concussion and this warrants further investigations on how these accessories could contribute to injury.

In low velocity impacts, impacts to the camera accessory resulted in decreased angular velocity (Table 6.1). However, in high velocity impacts, the angular velocity increased with the presence of an external camera mount. According to recent work by Takhounts *et al.* (2013) relating cumulative strain damage measure (CSDM) to animal brain injuries assumed to have etiology based on rotational mechanics [9], reduced CSDM would suggest decreased risk of severe concussion (severe concussion with loss of consciousness > 6 hrs), coded AIS4+ [74]. Using the risk curves from Takhounts *et al.*, CSDM can be computed based on maximum resultant angular velocity. Relating the resultant angular velocity to CSDM, and using the risk curves produced by Takhounts *et al.*, the average risk of severe concussion decreased from 15% to 4% when impacting the camera accessory for a low velocity impact. Conversely, in high velocity impacts, average severe concussion risk increased from 3% to 24% when impacting the camera accessory. The risk curves from Takhounts *et al.*, is based on data using a wide variety of test headforms and injury models, so the preceding injury risks should be considered indicative only of trends. Because we noted significant trends in both risk and angular velocity (known to be a contributor to diffuse brain injury), our results suggest further investigations on how these accessories contribute to injury are warranted.

Overall, the linear kinematic measures and force measurements beneath the camera accessory indicated a tendency toward reduced risk of skull fracture and severe life threatening brain injury in direct impacts to the camera accessory. In low velocity impacts (4 m/s nom.), kinematics (linear and angular acceleration) indicated relatively lower risk of

severe concussion when the camera accessory was present. In high velocity impacts (6 m/s nom.) the presence of the camera accessory (on average) increased risk of severe concussion.

Helmets with camera accessories experienced more impact liner damage than those without (Table 6.2), which suggests that when the helmets used in this study are fit with a camera, the liner could fail and expose the head at relatively lower energies than would be required to expose the head in impacts without a camera accessory. In the high velocity impacts, accessory contact with the headform was not observed. The maximum depth to which the camera accessories penetrated the liner was approximately 50% of the pre-impact liner thickness.

Like any study relying on ATDs and brain models, this study has limitations. Unlike human heads, the HybridIII does not fracture and it cannot be used to represent the wide variation in head mass and shape that could realistically fit within a medium helmet. Heads of variable mass/shape could experience varying kinematics that his study cannot capture. Another limitation to this work is the use of one impact site. In real-world scenarios, athletes can hit multiple locations on the helmet and also wear a helmet fitted camera accessory in different locations. Different impact sites on the helmet could also experience varying kinematics that was not studied. Impacts to the side or back of the head could provide altered kinematics because of the varying amount of liner exposed and protecting the head. The use of a repeatable head-neck model was appropriate because it eliminated the potentially confounding effects of variable head mass/shape.

Our overall objective was to quantify alterations in forces, and our model achieved this objective with repeatability commensurate with our other measures (Table 6.1). Our

measurements of force suggested low risk of skull fracture, and to our knowledge this is the first measurements of force through time of impact to the HybridIII head.

We have documented significant alterations in kinematics and forces experienced by the head in impacts to contemporary cycling helmets, between the cases of impact with and without a helmet camera accessory. These alterations suggest further study is warranted on the potential role that helmet accessories could play in altering the kinematics of the helmeted head and ultimately risk of injury.

7   CONCLUSION

7.1   Contributions

The first main objective of this thesis was to develop FBG-based impact force transducers that can integrate with existing ATD headforms like the HybridIII, and measure transient impact forces during impact, in parallel with the common kinematic measures (linear acceleration, angular acceleration) measured by the HybridIII. The second main objective is to apply the impact transducers, installed in a HybridIII headform, to answer a research question on head injury: do external helmet accessories (cameras), interfere with helmet ability to protect the head by studying risk of skull fracture (through force measurements using the force transducers) and brain injury (as evidenced by the typical kinematic measures) in impacts to camera accessories?

Experimental work included calibration to determine transducer sensitivity, and validation impacts to demonstrate repeatability of the impact transducers in both the force and time domain. Calibration and validation of the impact force transducers demonstrated repeatability in both the force and time domain for helmeted impacts. An experimental study was also developed to apply the impact transducers to quantify changes in head-helmet interaction forces during helmeted impacts both with and without an external helmet mounted camera.

The contributions of this thesis are summarized below:

1. Design and development of novel FBG-based impact force transducer:

The first contribution of this study is the design and calibration of the impact force transducers. The design of the impact transducer is small in size and is easily calibrated once fabricated. The calibration results of the impact transducers exhibit repeatability in the transducers sensitivity to force, as well as the time duration of each impact pulse. The spectral results from discrete Fourier transform of force measurements from the transducers indicated the same frequency characteristic for both the transducers and industry standard accelerometers. The results of the calibration experiment ultimately led to the second contribution: Transducer integration with anthropomorphic test headforms.

2. Transducer integration with anthropomorphic test headforms:

The second contribution of this work is the transducer repeatability in force measurements on different anthropomorphic test headforms. The impact force transducers produced repeatable force measurements and time durations while integrated with the magnesium and HybridIII test headforms. The transducers did not alter the kinematics (peak acceleration) of these test headforms. The repeatable results, while integrated with multiple headforms, led to the third contribution: Application of impact transducer to investigate head-helmet interaction forces during helmeted impacts.

3. Application of impact force transducer to give novel data on head-helmet interaction forces in impacts to an external helmet accessory with emphasis on skull fracture and concussion risk:

The contribution of this study was the use of the impact force transducers to study risk of head injury in helmeted impacts. The impact transducers were integrated with a HybridIII

headform and used to study the effects of an external helmet accessory on the risk of skull fractures during impact. Local forces were measured on the HybridIII headform both with and without an external helmet mounted camera. Based on the results of this study, there is no increased risk of skull fractures based on the local forces measured by the impact transducers (and kinematic measures). This is a novel study, the first examining the role of helmet accessories on injury risk, and the first measurements of force through time of impact to the HybridIII head.

In the context of understanding head injury, the transducers presented in this work could be used to answer inquiries that cannot be answered through measurements with stress sensitive films. For example, because the impact transducers can be integrated directly with a HybridIII headform, the impact transducers could be used to investigate head-helmet interactions under a wide range of applications. As mentioned previously, the impact transducers can also be used to study bare-head impacts, an application not applicable with stress sensitive films. The results from this work have established the feasibility of performing repeatable measurements that will be necessary to study helmet performance and head injury.

7.2   Future work

The impact force transducers presented in this work will continue to be used in ongoing research to study head-helmet interactions. Results from the force measurements can be used as inputs to finite-element models of the brain to investigate the effect of force measurements and brain injury.

Modifications to the design of the impact force transducer can allow the transducers to measure impact forces in the x, y, and z direction. The addition of two more FBG fibres orientated at different locations can produce force measurements in the normal and two shear directions. The ability to measure shear forces can give a better insight on the mechanics behind mild injuries to the brain, such as concussions. No existing sensors for applications in head trauma have the ability to measure normal and shear forces.

8   REFERENCES

[1]   K.-U. Schmitt, P. Niederer, M. Muser, and F. Walz, "Trauma Biomechanics: Accidental injury in traffic and sports." Springer New York Heidelber Dordrecht London, 2010.

[2]   N. Yoganandan and F. A. Pintar, "Biomechanics of temporo-parietal skull fracture," *Clin. Biomech. Bristol Avon*, vol. 19, no. 3, pp. 225–239, Mar. 2004.

[3]   Vanputte, Regan, and Russo, "Anatomy and Physiology," 10th ed., McGraw-Hill Professional, pp. 194–212.

[4]   Vanputte, Regan, and Russo, "Anatomy and Physiology," 10th ed., McGraw-Hill Professional, pp. 430–447.

[5]   M. Villarreal, "Human skull side simplified (bones)." [Online]. Available: https://commons.wikimedia.org/wiki/File:Human_skull_side_bones.svg#/media/File:Human_skull_side_simplified_%28bones%29.svg.

[6]   "CDC - TBI in the US Report - Traumatic Brain Injury - Injury Center." [Online]. Available: http://www.cdc.gov/TraumaticBrainInjury/tbi_ed.html. [Accessed: 09-Mar-2014].

[7]   L. Zhang, K. H. Yang, and A. I. King, "Comparison of brain responses between frontal and lateral impacts by finite element modeling," *J. Neurotrauma*, vol. 18, no. 1, pp. 21–30, Jan. 2001.

[8]   R. M. Greenwald and J. J. Crisco, "Head im[act severity measures for evaluating mild traumatic brain injury risk exposure," *Neurosurgery*, vol. 62, pp. 789–798, 2008.

[9]   E. G. Takhounts, M. J. Craig, K. Moorhouse, J. McFadden, and V. Hasija, "Development of Brain Injury Criteria (BrIC)," *Stapp Car Crash J.*, vol. 57, pp. 243–266, 2013.

[10]   J. A. Newman, "Biomechanics of Head Trauma: Head Protection," in *Accidental Injury: Biomechanics and Prevention*, New York, USA: Springer Verlag, 2002, pp. 303–323.

[11]   J. G. Beckwith, R. M. Greenwald, and J. J. Chu, "Measuring Head Kinematics in Football: Correlation Between the Head Impact Telemetry System and Hybrid III Headform," *Ann. Biomed. Eng.*, vol. 40, no. 1, pp. 237–248, 2012.

[12]   J. M. Hootman, R. Dick, and J. Agel, "Epidimiology of collegiate injuries for 15 sports: summary and recommendations for injury prevention initiatives," *J. Athl. Train.*, vol. 42, no. 2, pp. 311–319, 2007.

[13]   J. A. Newman, N. Shewchenko, and E. Welbourne, "A proposed New Biomechanical head injury assessment function - the maximum power index," *SAE*, 2000.

[14]   E. Gurdjian, V. Roberts, and L. Thomas, "Tolerance curves of acceleration and intracranial pressure and protective index in experimental head injury," *J. Trauma*, 1964.

[15]   "Crash Helmets for Motorcyclists, BS 1869-1952." .

[16]   "ASTM F1045-07: Standard Performance Specification for Ice Hockey Helmets." .

[17]   "Safety Standard for Bicycle Helmets; Final Rule." Consumer Product Safety Commission (CPSC), 10-Mar-1998.

[18]   V. Hodgson and L. Thomas, "Comparison of head acceleration injury indices in cadaver skull fracture," *SAE Tech. Pap. 710854*, p. 9 pp, 1971.

[19] C. W. Gadd, "Use of a Weighted-Impulse Criterion for Estimating Injury Hazard," SAE International, Warrendale, PA, 660793, Feb. 1966.

[20] J. Versace, "A Review of the Severity Index," SAE International, Warrendale, PA, 710881, Feb. 1971.

[21] "FMVSS Part 571 No.208 - Crashworthiness." .

[22] D. Marjoux, D. Baumgartner, C. Deck, and R. Willinger, "Head injury prediction capability of the HIC, HIP, SIMon and ULP criteria," *Accid. Anal. Prev.*, vol. 40, no. 3, pp. 1135–1148, Dec. 2007.

[23] H. Fenner, D. Thomas, T. Gennarelli, F. Pintar, E. Becker, J. Newman, and N. Yoganandan, "Final Report of Workshop on Criteria for Head Injury in Helmet Standards." Snell Memorial Foundation Inc, 06-May-2005.

[24] J. A. Newman, "On the Use of the Head Injury Criterion (HIC) in Protective Headgear Evaluation," SAE International, Warrendale, PA, SAE Technical Paper 751162, Feb. 1975.

[25] J. A. Newman, "A Generalized Model for Brain Injury Threshold (GAMBIT)," in *Proceedings of the 1986 International IRCOBI Conference on the Biomechanics of Impact*, Zurich, Switzerland, 1986.

[26] J. Newman, C. Barr, M. Beusenberg, E. Fournier, N. Shewchenko, E. Welbourne, and C. Withnall, "A New Biomechanical Assessment of mild traumatic brain injury. Part 2: Results and Conclusions," presented at the Proceedings of the 2000 International IRCOBI Conference on the biomechanics of impact, September 20-22, 2000, Montpellier, France, 2000.

[27] W. N. Hardy, M. J. Mason, C. D. Foster, C. S. Shah, J. M. Kopacz, K. H. Yang, A. I. King, J. Bishop, M. Bey, W. Anderst, and S. Tashman, "A Study of the Response of the Human Cadaver Head to Impact," *Stapp Car Crash J.*, vol. 51, p. 17, Jan. 2012.

[28] R. Ouckama and D. J. Pearsall, "Evaluation of a flexible force sensor for measurement of helmet foam impact performance," *J. Biomech.*, vol. 44, no. 5, pp. 904–909, Mar. 2011.

[29] F. O. Mueller and C. S. Blyth, "Fatalities from head and cervical spine injuries occurring in tackle football: 40 years' experience," *Clin. Sports Med.*, vol. 6, no. 1, pp. 185–196, Jan. 1987.

[30] J. A. Langlois, W. Rutland-Brown, and M. M. Wald, "The epidemiology and impact of traumatic brain injury: a brief overview," *J. Head Trauma Rehabil.*, vol. 21, no. 5, pp. 375–378, 2006.

[31] J. A. Newman, "Biomechanics of Head Trauma: Head Protection," in *Accidental Injury: Biomechanics and Prevention*, New York, USA: Springer Verlag, 2002, pp. 303–323.

[32] J. A. Newman, *Modern Sports Helmets: Their History, Science, and Art*. Schiffer Publishing, 2007.

[33] "CAN-CSA-D113.2-M89 (R2009)." Canadian Standards Association.

[34] "ISO, 10256:2003, Head and Face Protection for Use in Ice Hockey," *Int. Stand. Organ. Geneva Switz.*

[35] National Operating Committee on Standards for Athletic Equipment (NOCSAE), "NOCSAE DOC (ND) 081-04m04: Standard linear impactor test method and equipment used in evaluating the performance characteristics of protective headgear and face guards." Jan-2006.

[36] P. McCrory, W. Meeuwisse, K. Johnston, J. Dvorak, M. Aubry, M. Molloy, and R. Cantu, "Consensus statement on concussion in sport - the Third International Conference on Concussion in Sport held in Zurich, November 2008," *Phys. Sportsmed.*, vol. 37, no. 2, pp. 141–159, Jun. 2009.

[37] J. Z. Wu, W. Herzog, and M. Epstein, "Effects of inserting a pressensor film into articular joints on the actual contact mechanics," *J. Biomech. Eng.*, vol. 120, pp. 655–659, 1998.

[38] D. R. Wilson, M. V. Apreleva, M. J. Eichler, and F. R. Harrold, "Accuracy and repeatability of a pressure measurement system in the patellofemoral joint," *J. Biomech.*, vol. 36, pp. 1909–1915, 2003.

[39] P. J. Bishop and J. Arnold, "The effectiveness of hockey helmets in limiting localized loading on the head, in Safety in Ice Hockey," *Am. Soc. Test. Mater.*, pp. 175–182, 1993.

[40] A. Williams, "Michael Schumacher skiing crash: did helmet camera cause head injuries?," *The Telegraph (UK)*, 16-Feb-2014.

[41] R. M. Measures, *Structural Health Monitoring with Fiber Optic Technology*, vol. 1st. Academic Press, 2001.

[42] K. O. Hill, Y. Fujii, D. C. Johnson, and B. S. Kawasaki, "Photosensitivity in optical fiber waveguides: Application to reflection filter fabrication," *Appl. Phys. Lett.*, vol. 32, pp. 647–649, 1978.

[43] G. Meltz, W. W. Morey, and W. H. Glenn, "Formation of Bragg gratings in optical fibers by a transverse holographic method," *Opt. Lett.*, vol. 14, pp. 823–825, 1989.

[44] "Corning SMF-28 optical fibre: Product Information," *Corning Inc. Midl. MI Wwwcorningcomopticalfibre*, 2001.

[45] C. R. Dennison, "Development and application of in-fibre Bragg grating based biomedical pressure sensor," M.A.Sc. Thesis, University of Victoria, 2008.

[46] I. Abe, O. Frazao, M. W. Schiller, R. N. Noqueira, H. J. Kalinowski, and J. L. Pinto, "Bragg gratings in normal and reduced diameter high birefringence fibre optics," *Meas. Sci. Technol.*, vol. 17, pp. 1477–1484, 2006.

[47] H. Alemohammad, E. Toyserkani, and A. J. Pinkerton, "Femtosecond laser micromachining of fibre Bragg gratings for simultaneous measurement of temperature and concentration of liquids," *J. Phys. Appl. Phys.*, vol. 41, p. 185101, 2008.

[48] K. Smith, R. Selfridge, S. Schultz, D. Markos, and B. Ipson, "Analysis of replacing optical fiber core with polymer," *Opt. Express*, vol. 12, pp. 354–360, 2004.

[49] K. O. Hill and G. Meltz, "Fiber Bragg grating technology fundamentals and overview," *J. Light. Technol.*, vol. 15, pp. 1263–1276, 1997.

[50] Betz, "Advanced layout of a fiber Bragg grating strain gauge rosette."

[51] T. C. Buck, H. J. El-Khozondar, and A. W. Koch with M.S. Muller, "Shear Strain Influence on Fiber Bragg Grating Measurement Systems," *J. Light. Technol.*, vol. 27, no. 23, pp. 5223–5229, Dec. 2009.

[52] W. Qiu, X. Cheng, Y. Luo, Q. Zhang, and B. Zhu, "Simultaneous Measurement of Temperature and Strain Using a Single Bragg Grating in a Few-Mode Polymer Optical Fiber," *J. Light. Technol.*, vol. 31, no. 14, pp. 2419–2425, Jul. 2013.

[53] D. A. Singlehurst, C. R. Dennison, and P. M. Wild, "A Distributed Pressure Measurement System Comprising Multiplexed In-Fibre Bragg Gratings Within a Flexible Superstructure," *IEEE J. Light. Technol.*, vol. 30, pp. 123–129, 2012.

[54] C. R. Dennison, P. M. Wild, D. R. Wilson, and M. K. Gilbart, "An in-fiber Bragg grating sensor for contact force and stress measurements in articular joints," *Meas. Sci. Technol.*, vol. 21, p. 115803, 2010.

[55] S. Li-Yang, J. Qi, and A. Jacques, "Fiber optic pressure sensing with conforming elastomers," *Appl. Opt.*, vol. 49, pp. 6784–6788, 2010.

[56] S.-M. Lee, M.-Y. Jeong, and S. S. Saini, "Etched-Core Fiber Bragg Grating Sensors Integrated With Microfluidic Channels," *J. Light. Technol.*, vol. 30, no. 8, pp. 1025–1031, Apr. 2012.

[57] A. G. Mignani and F. Baldini, "Biomedical sensors using optical fibres," *Rep Prog Phys*, vol. 59, pp. 1–28, 1996.

[58] C. R. Dennison, P. M. Wild, P. W. G. Byrnes, A. Saari, E. Itshayek, D. C. Wilson, Q. A. Zhu, M. F. S. Dvorak, P. A. Cripton, and D. R. Wilson, "Ex vivo measurement of lumbar intervertebral disc pressure using fibre-Bragg gratings," *J. Biomech.*, vol. 41, no. 1, pp. 221–225, 2008.

[59] L. Mohanty, S. C. Tjin, D. T. T. Lie, S. E. C. Panganiban, and P. K. H. Chow, "Fiber grating sensor for pressure mapping during total knee arthroplasty," *Sens. Actuators A*, vol. 135, pp. 323–328, 2007.

[60] L. Carvalho, J. C. C. Silva, R. N. Nogueira, J. L. Pinto, H. L. Kalinowski, and J. A. Simoes, "Application of Bragg grating sensors in dental biomechanics," *J. Strain Anal.*, vol. 41, pp. 411–416, 2006.

[61] "EN 960:2006 Headforms for use in the testing of protective helmets." European Committee for Standardization (CEN).

[62] R. L. Norton, *Machine Design, An integrated approach*, 2nd ed. Prentice Hall, 2000.

[63] R. Ouckama and D. J. Pearsall, "Impact performance of ice hockey helmets: head acceleration versus force dispersion," *J. Sports Eng. Technol.*, vol. 226, no. 185, 2012.

[64] R. Butz and C. Dennison, "In-fibre Bragg grating impact force transducer for studying head-helmet mechanical interaction in head impact.," *J. Light. Technol.*, vol. 33, no. 13, p. 8, 2015.

[65] "SAE J211 Instrumentation for Impact Test - Part 1: Electronic Instrumentation." SAE International.

[66] A. Bartsch, E. Benzel, V. Miele, D. Morr, and V. Prakash, "Hybrid III anthropomorphic test device (ATD) response to head impacts and potential implications for athletic headgear testing," *Accid. Anal. Prev.*, vol. 48, pp. 285–291, Sep. 2012.

[67] P. A. Cripton, D. M. Dressler, C. A. Stuart, C. R. Dennison, and D. Richards, "Bicycle helmets are highly effective at preventing head injury during head impact: Head-form accelerations and injury criteria for helmeted and unhelmeted impacts," *Accid. Anal. Prev.*, 2014.

[68] B. Depreitere, C. V. Lierde, S. Maene, C. Plets, J. V. Sloten, R. V. Audekercke, G. V. der Perre, and J. Goffin, "Bicycle-related head injury: a study of 86 cases," *Accid. Anal. Prev.*, vol. 36, pp. 561–567, 2004.

[69] G. Gimbel and T. B. Hoshizaki, "A comparison between vinyl nitrile foam and new air chamber technology on attenuating impact energy for ice hockey helmets," *Int J Sports Sci Eng*, vol. 2, no. 3, pp. 154–161, 2008.

[70] "NEISS Data Highlights," 2012.

[71] "NHTSA Traffic Saefty Facts Data," 2014.

[72] F. Rivara and R. Thompson with Diane C. Thompson, "Helmets for preventing head and facial injuries in bicyclists."

[73] H. J. Mertz, A. L. Irwin, and P. Prasad, "Biomechanical and scaling bases for frontal and side impact injury assessment reference values.," *Stapp Car Crash J.*, vol. 47, p. 155, 2003.

[74] C. P. Carroll, J. A. Cochran, J. P. Price, C. E. Guse, and M. C. Wang, "The AIS-2005 Revision in Severe Traumatic Brain Injury: Mission Accomplished or Problems for Future Research?," *Ann. Adv. Automot. Med. Annu. Sci. Conf.*, vol. 54, pp. 233–238, Jan. 2010.